ISAS - INTERNATIONAL SCHOOL
FOR ADVANCED STUDIES

THE EVOLUTION OF MASSIVE STARS AND THE WEAK s–PROCESS

Thesis submitted for the degree of
"Magister Philosophiae"

Astrophysics Sector

Candidate:
Claudia Maria Raiteri

Supervisors:
Prof. Dennis Sciama
Prof. Roberto Gallino

Academic Year 1988/89

TRIESTE

SISSA - SCUOLA
INTERNAZIONALE
SUPERIORE
DI STUDI AVANZATI
TRIESTE
Strada Costiera 11

THE EVOLUTION OF MASSIVE STARS AND THE WEAK s–PROCESS

Thesis submitted for the degree of

"Magister Philosophiae"

Astrophysics Sector

Candidate:

Claudia Maria Raiteri

Supervisors:

Prof. Dennis Sciama

Prof. Roberto Gallino

October 1989

Contents

Chapter 1

INTRODUCTION

The evolution of a star depends on its mass, which governs the physical conditions inside it, and thus determines the ongoing of the subsequent thermonuclear stages.

After the initial contraction from the mother gas nebula, stars set on the Main Sequence, where the energy generation is provided by the conversion of hydrogen into helium at the centre. Low mass stars of $M \leq 1\ M_{\odot}$ stay on the so–called Lower Main Sequence. They have radiative cores and convective envelopes, and burn H via the p–p chain of nuclear reactions. On the Upper Main Sequence more massive stars convert H into He mainly through the CNO cycle, and have convective cores, but radiative envelopes. They may also experience some mass loss, which is supposed to be particularly important for the most massive of them.

When the central hydrogen is exausted, stars less massive than $\sim$ 7–9 $M_{\odot}$ (low and intermediate mass stars) leave the Main Sequence and run towards the Hayashy track, the coolest place of the HR diagram they can reach. During this phase the energy generation is supported by hydrogen burning in a shell which forms at the border of the H–depleted core.

The expansion of the stellar structure thus leads the stars to the Red Giants region, where they ignite helium at the centre, either quietly or with a succession of thermal flashes, depending if they are massive enough to avoid the degeneration of the helium core. The mass limit is strongly dependent on the physical parameters chosen in the evolutionary calculations: the classical value is $\sim 2.20\ M_{\odot}$, but if mass loss and overshooting are taken into account, it is lowered to $\sim 1.85\ M_{\odot}$.

After core helium burning, these stars are left with a strongly degenerate carbon–oxigen core, and during the double shell (H and He) burning they undergo the so–called thermal pulses, while ascending the Asymptotic Giant Branch (AGB) of the HR diagram. After that, the less massive ones ($M \leq 5\ M_{\odot}$) will suffer from a strong stellar wind, and a planetary nebula will be expelled, the star becoming a white dwarf. The higher mass ones, on the other side, will ignite carbon under degenerate conditions, and are supposed to give rise to the type I supernova phenomenon due to carbon deflagration, when the core has grown to the Chandrasekhar limit of 1.4 $M_{\odot}$.

Massive stars ($M \geq 10$–$12\ M_\odot$) can ignite carbon and then neon, oxygen and finally silicon burnings nondegenerately in their centers, until the iron–peak elements are synthetized. At that time, the star has an "onion–skin" structure, with layers of heavier and heavier elements going from the surface down to the centre. Now photodisintegration and electron– capture processes with the consequent release of neutrinos subtract energy from the star, that begins to contract. The contraction will go on until the core collapse occurs, followed by the core bounce, the shock wave formation and, if it is succesfull, by type II supernova explosion. Usually a neutron star is left, unless the star is very massive so that a black hole will form instead. Stars with masses in the range of 7–$9 \div 10$–$12\ M_\odot$ end their lives as electron–capture supernovae, that is they ignite oxygen under extremely degenerate conditions and suffer from intense electron captures on ^{20}Ne and ^{24}Mg, which make the core collapse before iron can be synthetized in the centre. The material ejected by a supernova explosion passes to the interstellar medium and partecipates to the chemical enrichment of the Galaxy.

In this thesis the evolution of a typical massive star of $25\ M_\odot$ was followed from the beginning of the hydrogen burning up to the end of core helium burning, testing the importance of variations in the thermonuclear reaction rates as well as in the initial metal content, and in one case the run was prolongued till the end of carbon burning.

The aim was to collect detailed physical information to follow the slow neutron–capture nucleosynthesis (the s–process) occurring during the final stages of central helium burning, which is believed to produce the heavy elements along the beta stability valley of the chart of nuclides in the atomic mass range $70 \div 90$.

On the other hand, according to the most updated investigations, the s–only isotopes with atomic mass greater than 90 are synthetized inside low mass stars ascending the AGB, during the repeated convective pulses that can provide an exponential distribution of neutron exposures. The results of the latest calculations indicate that it is possible to match the solar–system distribution of s–only nuclides in this atomic range, and a very good agreement with the results from the classical analysis of the s–process is now reached.

We would like to show that even for the light s–only isotopes it is possible to obtain a consistent picture for the explanation of the solar abundances, once a realistic galactic scenario is adopted, that is the contribution of a whole stellar generation of massive stars is considered.

Moreover, better determinations of the nuclear input data are now available which can play a fundamental role in the nucleosynthetic mechanism, and justify once more the reinvestigation of the s–process in massive stars.

Chapter 2

EVOLUTION OF MASSIVE STARS

When we speak about Massive Stars we refer to these objects which can avoid carbon burning under degenerate conditions after having experienced the hydrogen and the helium burnings. The lower limit for this to be true is about 7–9 $M_{\odot}$ depending on the physical inputs (metallicity, inclusion of overshooting and mass loss); over this limit stars ignite carbon quietly and direct themselves towards the core collapse and type II supernova explosion.

The hydrostatic stages of stellar evolution are easy to follow with the numerical codes that have been developed since the early calculations by Kippenhan et al. (1967), even if there are still some physical details whose treatment is under debate. The main sources of uncertainties at present are:

- *Mass Loss*
- *Semiconvection*
- *Overshooting*

The final stages of stellar evolution on the other side have to be studied by means of hydrodynamical codes, since the timescales of the nuclear processes involved become very short, and problems such as formation of shock waves must be faced.

2.1 MASS LOSS

Even if the physical nature of the mechanism is still obscure, observations show that stars do lose mass during their lives, the phenomenon being particulary significant for the most massive and coolest ones. The mass loss rate changes with the type of star and with luminosity, and is commonly given by empirical relations of the kind $\dot{M}$ = f (L, R, M,...) (see Chiosi and Maeder, 1986 for a detailed review). Brunish and Truran (1982a,b) studied the evolution of massive stars with and without mass loss. They stressed out that the inclusion of mass loss has several consequences on star evolution:

- the evolutionary track in the HR diagram moves at lower luminosity and effective temperature;
- since less energy must be radiated away now, the Main Sequence phase is prolongued, and also the helium burning lifetime is generally increased;
- stars move faster towards the red all along the He–burning;
- during the Main Sequence, semiconvective regions are narrower and of shorter duration;
- in the next phases, the amplitude of convective regions is reduced;
- the mass fraction $q_\alpha = M_\alpha/M_{tot}$ occupied by the helium core [1] is left unchanged when a moderate mass loss is included, because both M_α and M_{tot} are decreasing, while the maximum size the convective core reaches during He–burning is largely unaffected by mass loss (but see Maeder, 1981a, who found that in mass–losing models the growth of the convective core in this phase is greater than for constant mass evolution).

Moreover, when substantial mass loss rates are considered, they may allow nuclear processed matter to appear on the surface, where it can be detected spectroscopically and can give us information on the correctness of our assumptions on stellar evolution and nucleosynthesis.

Finally, the lost material which comes back to the Interstellar Medium can take part in the chemical enrichment of the Galaxy.

[1] M_α, the helium core, is defined as that part of the star's mass that is H–depleted due to the conversion of H into He during hydrogen burning; later on we shall also meet M_{CO}, that is the carbon–oxygen core that is left by the convective central helium burning.

2.2 SEMICONVECTION AND OVERSHOOTING

When we speak of *Semiconvective Regions* we mean those regions that suffer from vibrational instabilities caused by a gradient in the mean molecular weight μ, and by their being unstable according to the Schwarzschild criterion:

$$\nabla_{rad} \geq \nabla_{ad},$$

where ∇_{rad} is the radiative temperature gradient, and $\nabla_{ad} = (d\ln T/d\ln P)_{ad}$ the adiabatic one, unless full convection can be established. Situations where semiconvection may appear are found when the convective core shrinks during the Main Sequence evolution, or when the H–burning shell moves outwards during the core helium burning. In semiconvective regions the mixing timescale is slower than in convective zones, because the μ gradient fights against convection, but however a rearrangement of the chemical composition of the layers involved is obtained, until a neutrality condition is established, which is either the Schwarzschild's one, or the Ledoux one:

$$\nabla_{rad} = \nabla_{ad} + \frac{\beta}{4-3\beta}\nabla_{\mu} \equiv \nabla_{L},$$

where $\beta = P_g/P_{tot}$ is the ratio between the gas pressure and the total pressure, and $\nabla_{\mu} = d\ln\mu/d\ln P$ is the mean molecular weight gradient.

By using a diffusion approximation to semiconvection, Langer et al. (1985) and Langer (1986b) pointed out that while during the H–burning evolutionary phase the nuclear timescale is much greater that the semiconvective mixing timescale, so that the Schwarzschild's criterion for convection can be used, in the subsequent phases the Ledoux's criterion has to be considered and the inclusion of semiconvection implies that less mixing is allowed in comparison to the canonical treatment, which can greatly affect the evolutionary behaviour of the star. In particular Langer (1986b) found that the slowly mixed region on the top of the growing convective He–burning core, which developes because of the large μ–gradient at that point, has the effect of reducing the ^{12}C concentration at He–exhaustion and to lead to a nearly complete burning of the ^{22}Ne through the ^{22}Ne$(\alpha,\gamma)^{25}$Mg reaction in the final stages of helium burning. This is supposed to greatly increase the s–process nucleosynthesys efficiency that will be the subject of the following chapters.

In our calculations however semiconvection is obtained by adopting the Schwarzschild's criterion and a very fine zoning in the layers of varying molecular weight, as in the Lamb et al. (1976) work.

Another important problem which is related to the mixing processes in stars is the extension of convective cores that is usually investigated in terms of *Overshooting*. When we follow the canonical prescription to delimit a convective region (the Schwarzschild's condition), we assume the boundaries to be positioned where the acceleration of the convective bubbles goes to zero. But it seems reasonable that

the convective elements would continue their travel until their velocity goes to zero, penetrating (overshooting) into the adjacent regions that are in radiative equilibrium. In most of the stellar evolution calculations convection is analyzed through the Mixing Length Theory, but a correct treatment of this mechanism should be non local in order to take into account the inertial momentum of the convective elements (Maeder, 1975). When overshooting is considered, several consequences are found (Bressan et al., 1981; Bertelli et al., 1984, 1985, 1986; Maeder and Meynet, 1987):

- the convective cores during H and He burnings are enlarged, the effect being stronger for the smaller masses, and this implies that these models have larger helium and carbon–oxygen cores, which ultimately means that the central conditions (central temperature and density) match those of more massive stars. In particular, the C/O ratio at the end of core He–burning will be affected, being lowered if some overshooting is present;

- the evolutionary tracks in the HR diagram run at higher luminosities, and a wider Main Sequence band covering a larger range of effective temperatures is obtained;

- the total stellar lifetime is enhanced; as for the core H–burning episode, it is prolongued, while the He–burning one is shortened. This is explained by the fact that the higher luminosities of these models act in the direction of a faster evolution that during the Main Sequence phase is reversed by the availability of a greater amount of fuel (greater core mass);

- semiconvective instability does never occur in models with overshooting from the convective core.

Anyway, there are no theoretical prescriptions on the amount of overshooting which may be present in stellar interiors, and the mixing length parameter α defined as the ratio between the maximum distance travelled by the convective bubbles l to the pressure scale height H_p is considered as a free parameter, its calibration relying on a careful comparison with the observations (Bressan et al., 1981; Bertelli et al., 1985). Recently Maeder and Meynet (1987, 1989) have stressed that a moderate overshooting with $\alpha = 0.25$ best represents the observations of the main star clusters features such as:

- the main sequence width;

- the blue extension of the loops described in the HR diagram during the helium–burning phase;

- the number ratio of blue to red giants in the He–phase;

- the luminosity difference between the yellow giants and the Main Sequence turnoff (see below);
- the upper mass limit for degenerate helium burning.

In our computations overshooting will naturally arise from the opacity increase in the convective core starting from the beginning of helium burning, and the core growth will be obtained by a self–driving mechanism that has been described by Castellani et al. (1971a). As the evolution goes on, the behaviour of the radiative gradient at the core boundary will lead to the so–called "*Induced Semiconvection*" phenomenon (Castellani et al., 1971b, 1985) The details of the whole story will be discussed below, when we present the results of our models evolution.

Beside overshooting, other mixing mechanisms such as shear flow instabilities, meridional circulation or turbulent diffusion have been suggested to give larger convective cores.

2.3 THE EVOLUTIONARY CODE

A lot of evolutionary sequences have been calculated in the literature, with different numerical codes and different choices for the input physics. If we examine the position in the HR diagram of the canonical models (no mass loss and the Schwarzschild's criterion for convection), we have to conclude that the theoretical results are not able to fit the empirical data: the number of very bright Main Sequence stars seems to be lower than the expected one, and the computed He-burning evolution is not able to explain the abundances of red and blue supergiants. It seems that only the coupled effect of a moderate mass loss with a moderate core overshooting can bring the theoretical calculations in agreement with the observations. Anyway since our final aim is to collect data in order to study the neutron-capture nucleosynthesis during the late stages of the convective helium core burning, we simply ignored the mass loss and overshooting problems. Indeed, as was recently stressed by Langer et al. (1989), what is really important from the nucleosynthetic point of view is the carbon–oxygen core mass at the end of the helium burning phase, rather than the actual stellar mass during the He combustion. We shall leave the problem of finding the relation between this core mass and the Zero Age Main Sequence (ZAMS) mass in the hands of the stellar evolution experts.

So we used the FRANEC (Frascati Raphson–Newton Code) with the mass-loss routine call disabilited and the convective helium core growth inhibited when the helium mass fraction goes below 0.10 in order to avoid the "*Breathing Pulses*" mechanism to develop (see Castellani et al., 1985) [2] The integration of the stellar structure is performed by means of a Newton–Raphson scheme. The mass of the star is completely divided into sections: the outer 3% forms the subatmosphere, while the inner 97% is shared among almost 800 meshes of variable size. The mesh boundaries are computed at each time step by the requirement that the stellar physical variables R, L, P, T and M do not vary by more than some percent from one meshpoint to the next one.

The nuclear network includes 20 elements linked by 34 nuclear reactions and 12 $\beta-$ decays; the thermonuclear reaction rates are taken from Fowler et al. (1975; FCZ75) and subsequent updatings by Harris et al. (1983) and Caughlan et al. (1985; CFHZ85); a run with the most updated rates by Caughlan and Fowler (1988; CF88) was also performed.

[2]The Breathing Pulses are essentially due to thermal instabilities occurring at the end of core He-burning, when the growth of the convective core bringing new helium into a very hot and almost He-exhausted environment ($Y_c < 0.1$) makes the central structure of the star rejuvenate and the 3 α reaction burn the fresh fuel with an excess of nuclear energy release. This in turn enhances convective instability and induces further mixing, producing a considerable increase of the size of the mixed region and consequently of the He-burning lifetime. But the comparison of the models evolved with the breathing pulses allowed with the observations ruled out the real occurrence of this mechanism, that is now commonly recognized as being due to an unappropriate (local) numerical treatment of the mixing trough the convective core border (Chiosi et al., 1986).

Two different equations of state have been adopted: in regions where the temperature is greater than 10^6 K the matter is assumed completely ionized and the new set of tables of thermodynamical quantities computed by Straniero (1989) have been used. They take into account electron degeneracy and relativistic effects, electron–positron pair production and Coulomb interactions among ions and electrons. For temperatures lower than 10^6 K only partial ionization occurs and the thermodynamical behaviour of matter is derived by means of the Saha equation. The radiative opacity coefficient is calculated as a function of density and temperature by using the Los Alamos opacity library; the adopted chemical mixture is that of Ross and Aller (1976).

The surface convection is treated through the mixing length formalism with a ratio between the mixing length and the pressure scale height equal to $\alpha = l/H_p = 1.6$.

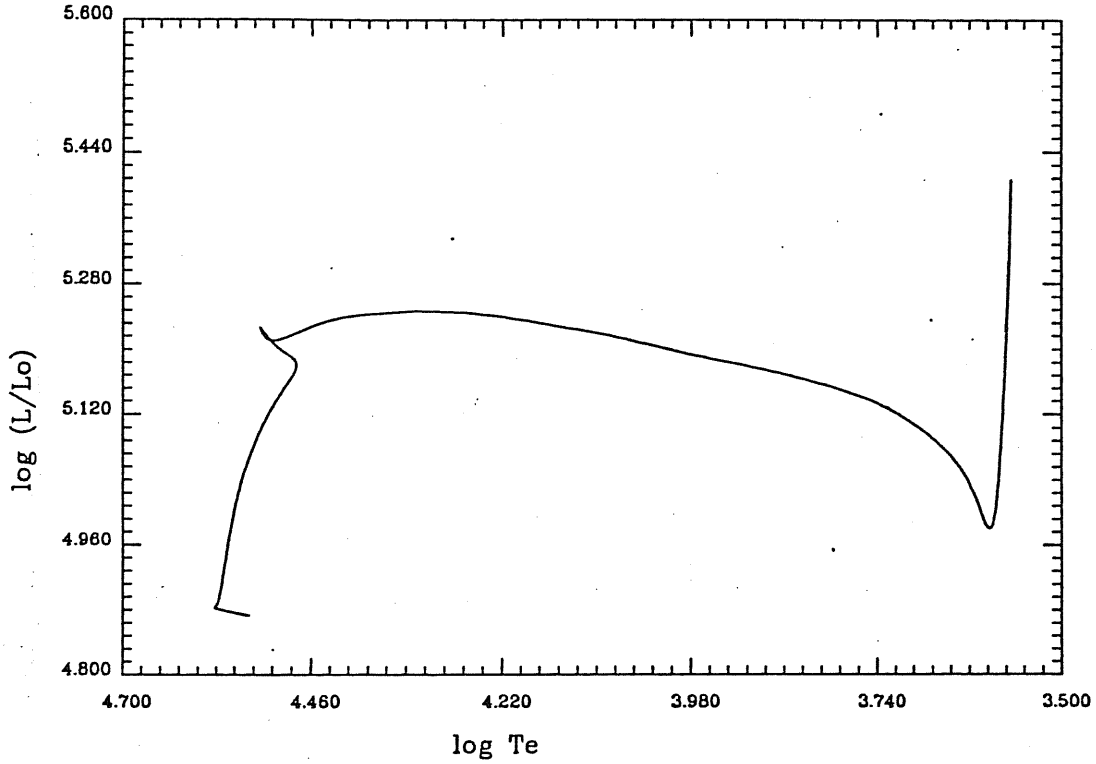

Figure 2.1: The HR diagram for the 25 $M_\odot$ pop.I star

2.4 EVOLUTION OF A M=25 $M_\odot$ POP.I STAR

We chose to follow the evolution of a 25 $M_\odot$ star with a helium content of $Y = 0.28$ and a nearly solar metallicity: $Z = 0.02$. The initial CNO content has to be consistent with the scale of the heavy element abundances the tables of opacities are based on. We then started with the following mass fractions:
$X_C = 0.2179Z$; $X_N = 0.0531Z$; $X_O = 0.4816Z$.
The behaviour of the star in the HR diagram is shown in figure 2.1, while figure 2.2 gives a picture of the evolution of the central conditions.

2.4.1 The Hydrogen Burning Phase

Our model sets up on the ZAMS with $\log(L/L_\odot) = 4.882$, and $\log T_e = 4.582$ K. It has got a 12.705 $M_\odot$ central convective core, and the central temperature and density are $\log T_c = 7.565$ K and $\log \rho_c = 0.584$ g/cm^3 respectively.

The transformation of H into He through the CNO cycle makes the opacity decrease and the convective core recede: when $X_c \simeq 0.50$, $M_{cc} = 10.738\ M_\odot$, and when $X_c \simeq 0.10$, $M_{cc} = 7.256\ M_\odot$.

Above the fully convective core, regions of semiconvection develop as a series of alternating, thin convective and radiative shells, leading to the construction of

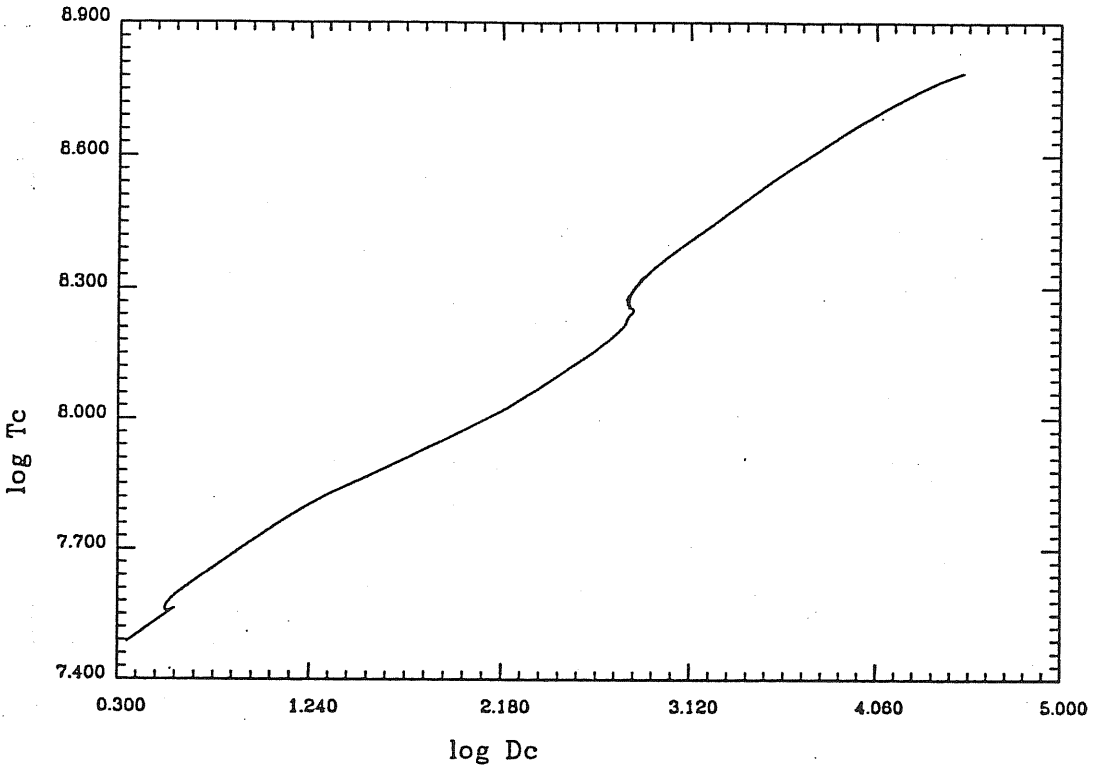

Figure 2.2: The evolution of the central conditions for the 25 $M_\odot$ pop.I star

a gradient in the mean molecular weight μ. The mass boundaries of these shells change with time, so that in the semiconvective regions we have variable steplike chemical profiles as shown in figure 2.3. In this figure, as in the following figures of this kind, L, R, P, T, D stand for luminosity, radius, pressure, temperature and density respectively; En is the nuclear energy generation; K the opacity; Rad and Ad are the radiative and adiabatic gradients. The physical parameters are normalized to the maximum value, which is shown on the right of the figure. The star goes up on the Main Sequence (MS) expanding in order to radiate away the energy produced by the nuclear reactions in the centre, until it reaches the Turnoff point (TO), at $\log T_e = 4.478$ K, $\log(L/L_\odot) \sim 5.18$. Here, the H central content is $X_c \simeq 0.03$.

Now the CNO cycle is loosing efficiency (see figure 2.4) and the point representing the star in the HR diagram starts moving on the left. It arrives at the MS Termination point (TE), i.e. the point when H is exhausted in the core, with $\log T_e = 4.523$ K and $\log (L/L_\odot) = 5.227$. Soon after the convective core disappears. If we choose this time as the time at which the hydrogen-burning phase ends, we get a H-burning time duration of 6.101004 Myr. Now the luminosity and effective temperature values are: $\log(L/L_\odot) = 5.211$ and $\log T_e = 4.501$, while the central temperature and density are: $\log T_c = 7.901$ K and $\log \rho_c = 1.675$ g/cm^3. The star is left with a He-core $M_\alpha = 6.772\ M_\odot$.

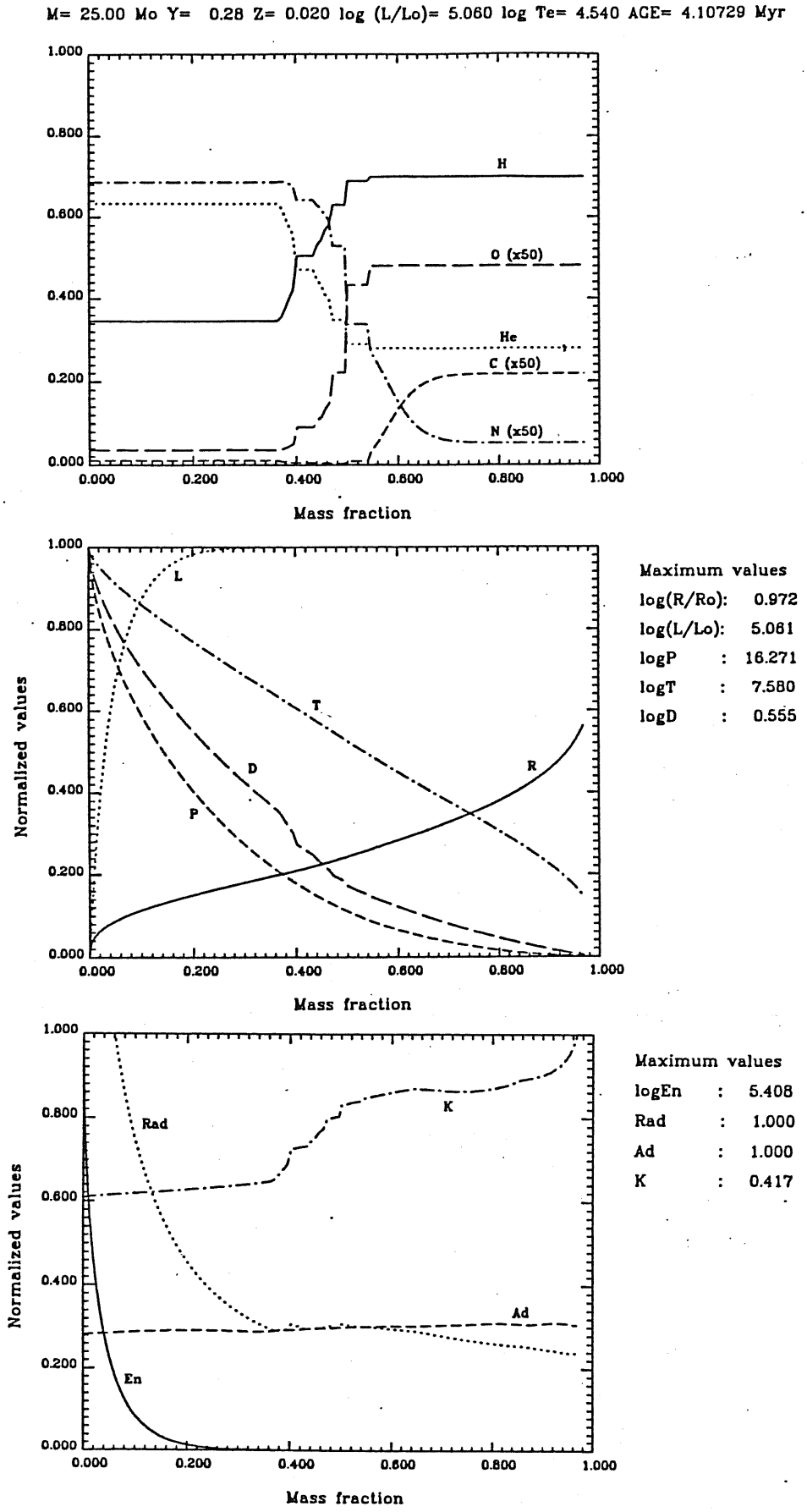

Figure 2.3: The chemical and physical stucture of the 25 $M_\odot$ pop.I star during hydrogen burning.

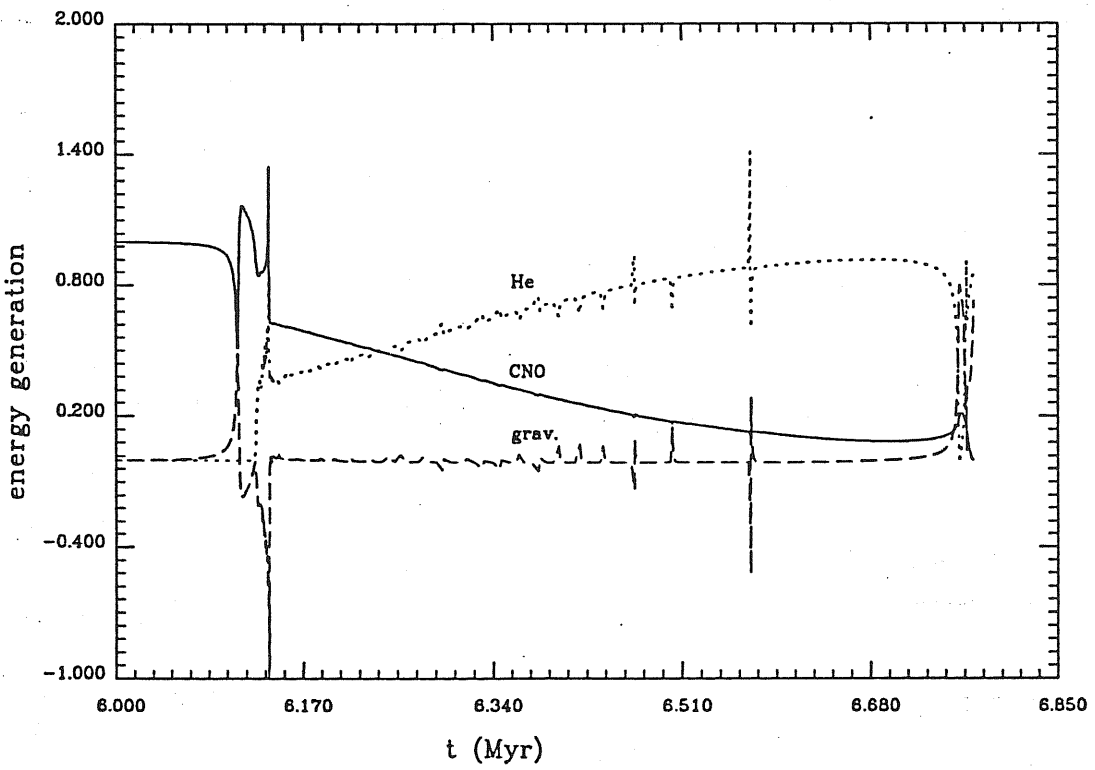

Figure 2.4: The energy generation for the 25 $M_\odot$ pop.I star from the end of H–burning to past the end of He–burning.

2.4.2 The Hydrogen Shell Burning Phase

The TE point is the point where the nuclear energy generation by the CNO cycle has a minimum. After that, it promptly rises again very rapidly because of the appearence of a H–burning shell just outside the convective core. Above it, semiconvective regions mantain the μ gradient.

At H–exhaustion, the shell is situated at M_r ~6.9 $M_\odot$ and has an extension of ~5.4 $M_\odot$. The temperature corresponding to the peak of the shell energy generation is ~4.07×10^7 K, high enough to produce the CNO equilibrium at once. This can be seen by looking at the N and C profiles in figure 2.5, that show sharp peaks at M_r/M_{tot} ~0.29. The star spends 1.1174×10^4yr in this H–shell energy–supported, radiative core phase.

2.4.3 The Helium Burning Phase

He–ignition takes place when $\log(L/L_\odot) = 5.246$, $\log T_e = 4.310$ K; the values of the central temperature and density are: $\log T_c = 8.164$ K and $\log\rho_c = 2.668$ g/cm^3, and the He–core involves 6.707 $M_\odot$. A convective core forms again which grows very rapidly to include ~ 16% of the star mass.

The hydrogen shell shrinks to ~2.24 $M_\odot$ and slowly moves outward, reducing its mass extension. Above the H–shell we still have regions of semiconvection.

By looking at figure 2.4 we see that during this first part of the He–burning, the star is supported mainly by the CNO energy generation in the shell and its point in the HR diagram moves towards the Hayashi line. In the meantime the energy output of the 3α reaction increases until the condition $\varepsilon_{CNO} = \varepsilon_{3\alpha}$ is reached after ~ 1.12×10^5yr from He–ignition; from now on, the star lives principally thanks to the He combustion in the convective core and climbs up the Hayashi track, rising the luminosity but keeping the effective temperature almost constant.The point of relative minimum luminosity at $\log T_e = 3.594$ marks the time when the outer envelope becomes convective due to the recombination of electrons with protons that increases the opacity. The external convection then starts to penetrate inward, down to regions that have previously experienced nuclear processing by H–burning. At the maximum extension this convective envelope has a mass of 15.71 $M_\odot$ and the matter dredged up makes the atmospheric chemical composition change: now we have $X_{sup} \simeq 0.66$, $Y_{sup} \simeq 0.32$.

The structure of the star at this point is very simple, as can be seen in figure 2.6: starting from the centre we have a convective core which is filling the inner 16% of the total mass; the remainder of the He–core is in radiative equilibrium. Outside it H is converted into He in a radiative shell; then there is a thin region with a steep H profile, and finally the convective envelope, which involves the outer ~63% of the total star mass.

Now we can examine the reasons that lead to the growth of the convective core with time, as is shown in figure 2.7. Since the beginning of the helium–burning, the

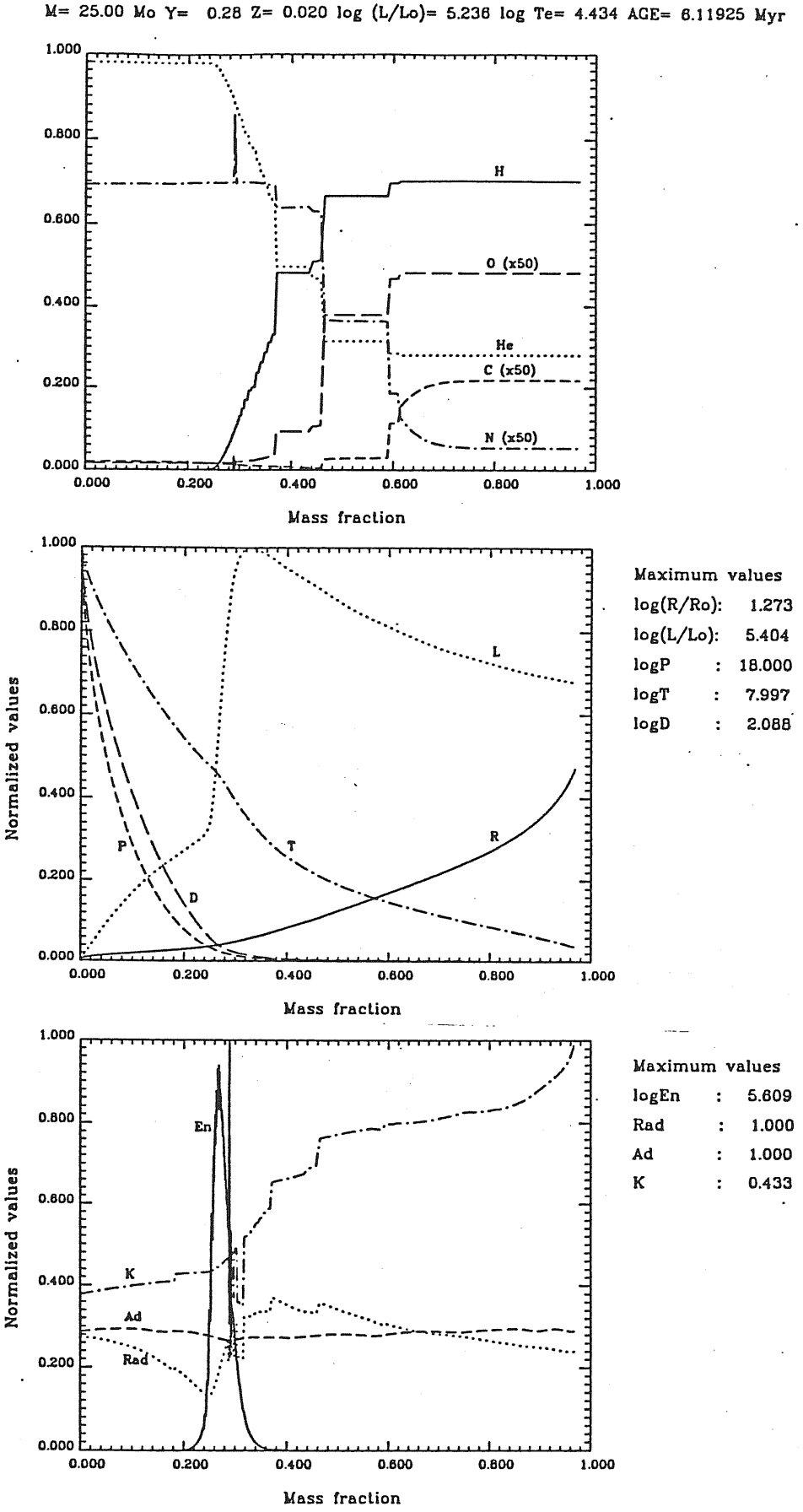

Figure 2.5: The chemical and physical stucture of the 25 $M_\odot$ pop.I star during the shell-hydrogen burning phase.

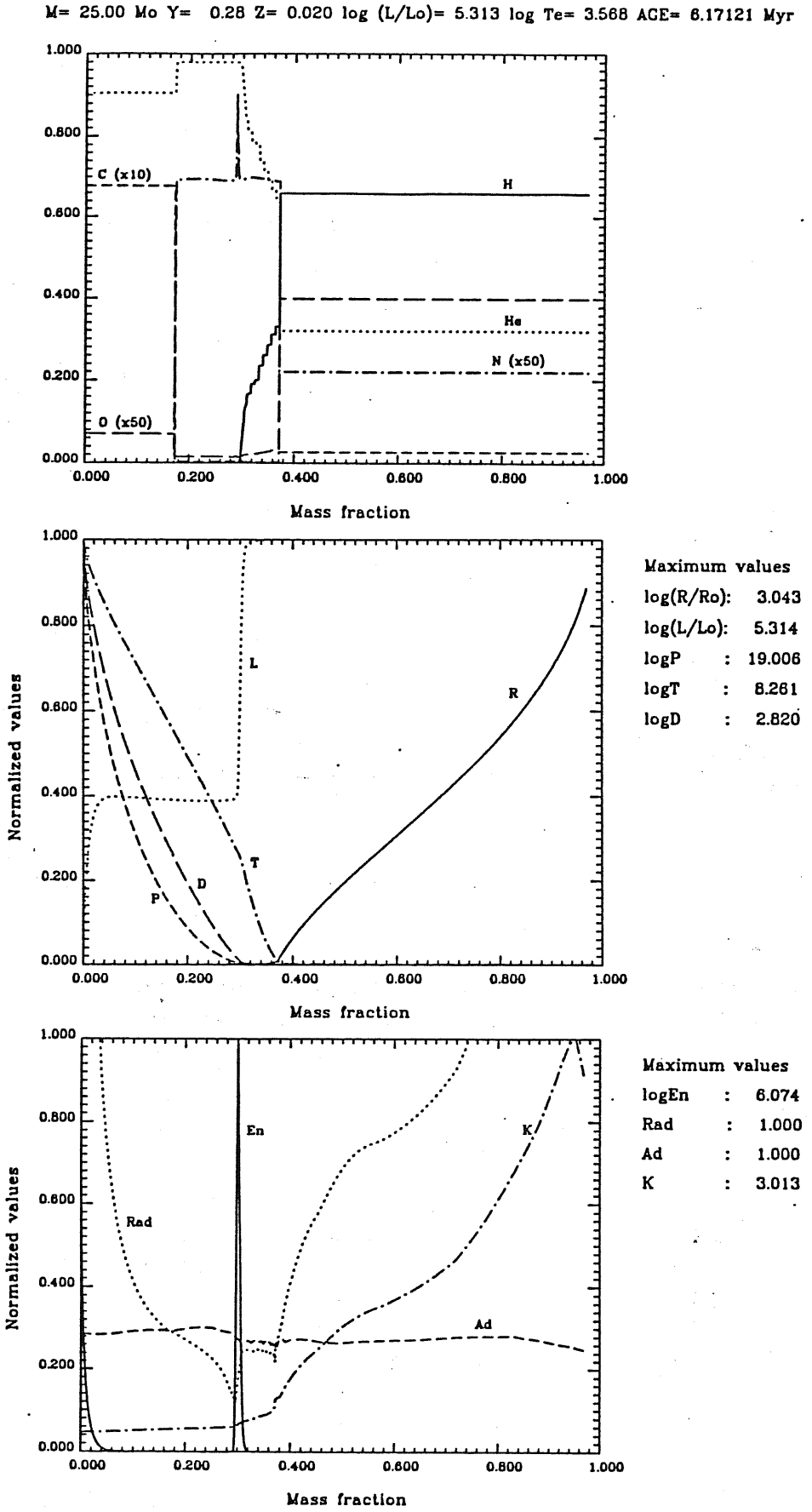

Figure 2.6: The chemical and physical stucture of the 25 $M_{\odot}$ pop.I star during the He–core burning, when the convective envelope has reached the maximum extension.

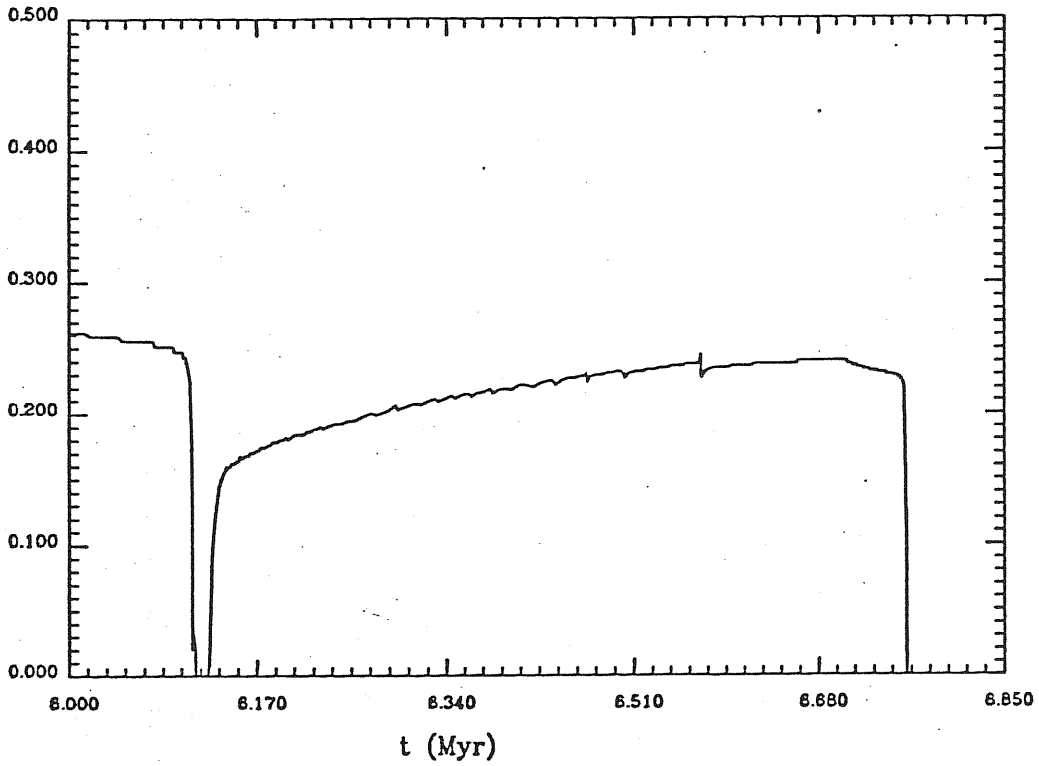

Figure 2.7: The fractional mass extension of the convective core from the end of H–burning till the end of He–burning.

He conversion into C first, and into O later, makes the opacity (which is essentially due to free–free processes) become larger and the increasing chemical discontinuity that occurs at the edge of the convective core leads to a growing discontinuity in the radiative gradient of the type:

$$\nabla^e_{rad} \leq \nabla_{ad} \simeq 0.4 < \nabla^i_{rad},$$

where the superscripts e and i refer to the external side and the internal one of the interface between the convective core and the outer radiative region. But this kind of situation is not physically acceptable (Schwarzschild, 1958), and it is solved by mixing the core with external material from the radiative region, thus creating a layer of increased opacity which becomes unstable against convection. The discontinuity in the radiative gradient is moved from the internal to the external side of the boundary (see figure 2.8) and the stability condition:

$$\nabla^i_{rad} = \nabla_{ad}$$

is obtained, which implies a widening of the convective core. However, as the evolution goes on, the scenario becomes more complex, and the radiative gradient experiences a minimum. Extension of convection beyond the minimum drives an

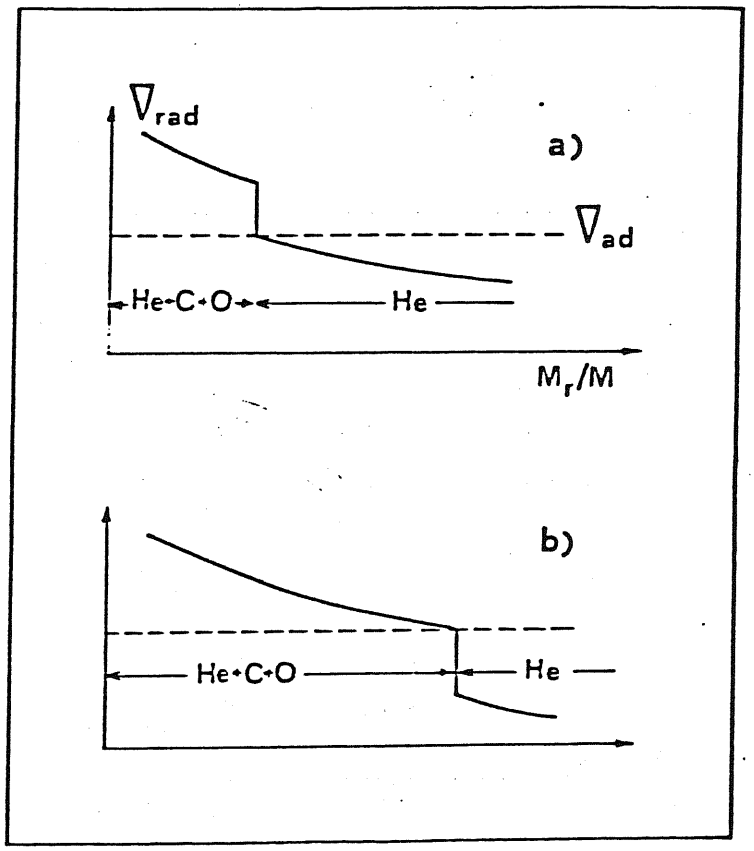

Figure 2.8: Schematic behaviour of the temperature gradients near the boundary of a convective core: a) with a grown chemical discontinuity; b) in the time-stable situation (Castellani et al., 1971a).

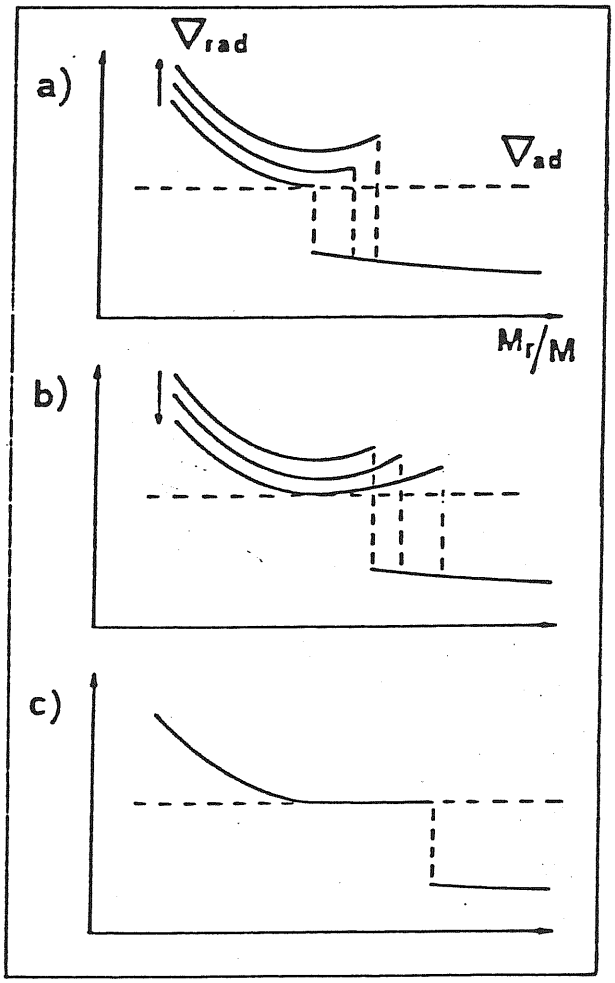

Figure 2.9: Schematic behaviour of the radiative temperature gradient against mass fraction after the minimum of ∇_{rad} has been reached (Castellani et al., 1971b).

increasing super–adiabacity at the core boundary. Correspondingly, the propagation of convection tends to become more efficient and larger mass shells captured and mixed until finally ∇_{rad} starts to decrease in the whole convective region. It will finally reach the value of the adiabatic gradient at the minimum location, creating a cut–off point for convection. The outer superadiabatic layer will be mixed with external material until the Schwarzschild's condition is established in the whole area: an intermediate region of semiconvection is formed, not in the classical way (as briefly outlined in a previous section), but as a consequence of the partial mixing induced by the unstability of the core. This is why the mechanism is called "Induced Semiconvection". In figure 2.9 a schematic picture of this process is given. The story repeats itself until a maximum value for the convective core is reached; in our model it is given by $M_{cc}^{max} = 6.114\ M_{\odot}$. Later on the convective core starts to recede, and a radiative region with varying chemical composition is left outside the core.

When Y_c goes below $\sim$0.26, the $^{12}C(\alpha,\gamma)^{16}O$ reaction becomes effective, and carbon starts to decrease in favour of oxigen. The central temperature and density are 2.128 $\times 10^8$ K and 7.980 $\times 10^2$ g/cm^3 respectively.

At the end of He–burning, the photospheric values of the star are: $\log(L/L_{\odot}) = 5.343$, and $\log T_e = 3.567$ K, while the central ones are $\log T_c = 8.539$ K and $\log\rho_c = 3.524$ g/cm^3. The star is left with a carbon–oxigen core $M_{CO} = 6.295\ M_{\odot}$, where carbon and oxigen mass fractions are $X_C \simeq 0.17$ and $X_O \simeq 0.80$ (figure 2.10), inside a H–exhausted core $M_{\alpha} = 8.876\ M_{\odot}$. As we can see, the He core has increased by $\sim$31% since the end of the H–core burning. The whole He–burning phase lasted 0.634528 Myr, and this means that the ratio between the core He–burning to the core H–burning meanlives is $\Delta t_{He}/\Delta t_H = 0.104$.

2.4.4 Comparison With Previous Works

We must remind that we are dealing with a canonical model, that is a model without mass loss and overshooting. Canonical models of 15 and 25 $M_{\odot}$ stars with a solar composition were analyzed by Lamb et al.(1976) and Weaver et al. (1978), and a grid of three evolutionary sequences for M = 15, 30 and 40 $M_{\odot}$ stars were run by Brunish and Truran (1982a), who also considered the effects of mass loss. We must also remember the two papers by Maeder (1981a,b), who investigated the evolution of 9–170 $M_{\odot}$ stars of X = 0.70, Z = 0.03 composition with and without mass loss. Many are the differencies between these works and ours, and it isn't easy to point out which of them plays the dominant role in producing discrepancies. In particular, our model was evolved with the CFHZ85 $^{12}C(\alpha,\gamma)^{16}O$ reaction rate. This is a very critical question, since this rate strongly affects the whole evolution of a star, and in particular the core helium burning phase. But up to now this fundamental nuclear input is still poorly known: the recent compilation of thermonuclear reaction rates by Caughlan and Fowler (1988) gives it within an uncertainty of a factor 2.

In order to investigate this point, we performed a run of our 25 $M_{\odot}$ $Y = 0.28$ $Z = 0.02$ star, changing the CHHZ rate into the FCZ75 one, which is about 3 times

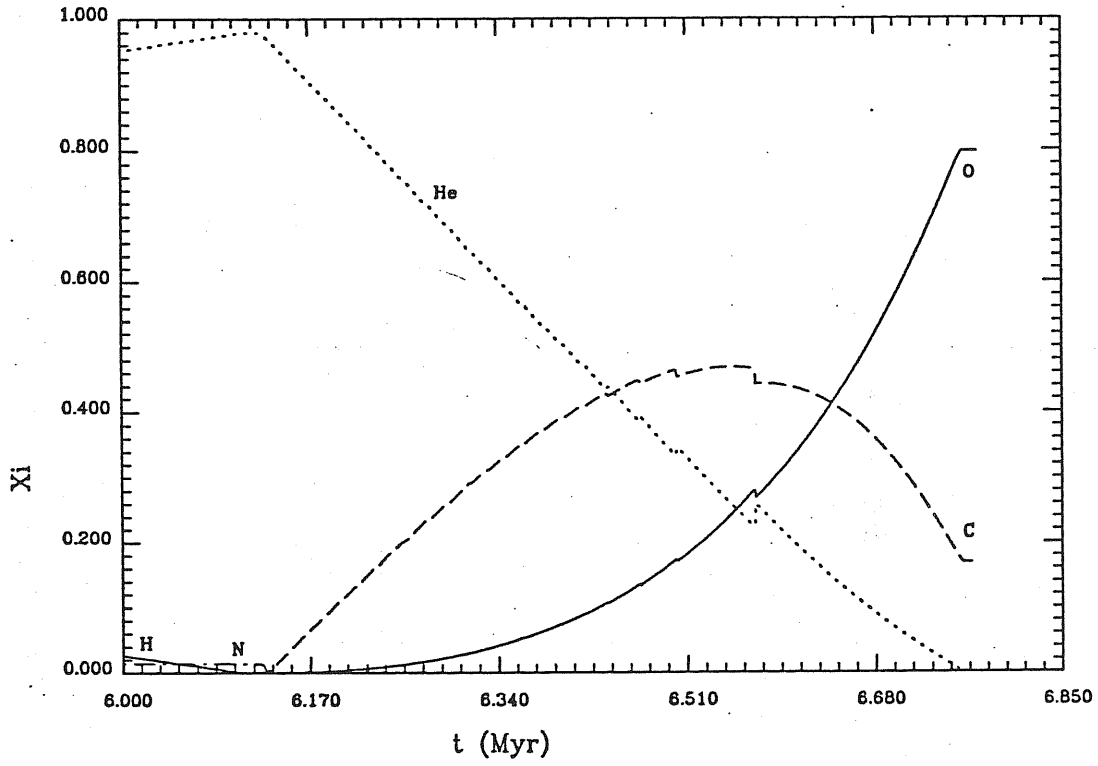

Figure 2.10: Evolution of the main chemical species (mass fractions) from the end of H–burning till past the end of He–burning.

lower. The results are that the He–burning phase is shortened by about 12%: it lasts only 0.560050 Myr, and $\Delta t_{He}/\Delta t_H = 0.092$ now. Consequently the convective He–burning core has no time to grow to the point it reached in the previous case: the maximum value of M_{cc} is only 5.853 $M_\odot$, and at the He–exhaustion the proportions between the carbon and oxigen abundances are obviously changed: carbon is ~47%, and oxygen is ~50%. The Helium and Carbon–Oxygen cores are also slightly reduced: $M_\alpha = 8.864\ M_\odot$, and $M_{CO} = 6.037\ M_\odot$. The other relevant parameters are pratically the same.

Let us now compare our results to the ones of the past literature. There is a general agreement in the results; in particular our model correctly places in between the 15 and 30 $M_\odot$ models by either Maeder (1981a,b) and Brunish and Truran (1982a). A few remarks must be made, however:

1. Our star ignites He in the blue part of the HR diagram, but then rapidly moves to the red: as a matter of fact, if we consider $\log T_e = 3.8$ K as the separation point between the blue and the red, we have that $\Delta t_{BLU} \simeq 0.011943$ Myr, while $\Delta t_{RED} \simeq 0.622585$ Myr. This means that more than 98% of the total He–burning lifetime is spent in the red! Brunish and Truran found that the 15 $M_\odot$ model spends only 2.4% of its lifetime as a red supergiant; for the 30 $M_\odot$ model this number is 1.5%. Since the post–He burning evolution of a massive star requires less than 0.1% of the total lifetime (Weaver et al., 1978), we estimate that our model lives more than 9% of its life in the red, in disagreement with the Brunish and Truran finding that "*Stars with $M_i \leq 30\ M_\odot$ evolve redward very slowly and spend less than 1% of their total lifetimes as red supergiants*", even when a moderate mass loss was included. However, these authors stressed that in order to match the observations an increase in the rate of redward evolution was needed, possibly achieved by using higher mass loss rates.

   The 25 $M_\odot$ model by Lamb et al. on the contrary never becomes a red supergiant, and the authors had to conclude that most of the RSG are accounted for by Intermediate Mass Stars (IMS) in the double shell burning phase.

   Finally, Maeder reported that the ratio between the red and the blue star numbers from observations within the galactocentric distances 8–10 Kpc is 0.02–0.08 (we have 0.09!). He was able to match this number considering mass loss, which he found to be able to increase the lifetime in the red supergiants by a factor of 4–5.

   The different behaviour of all these tracks can be mainly the consequence of the changed atmospheric conditions: we have new opacities data and a higher value for the α parameter which is used in the treatment of superficial convection ($\alpha = 1.6$ instead of $\alpha = 1.0$ adopted by Lamb et al. and $\alpha = 0.7$ by Brunish and Truran). As a final result, the behaviour of the envelope is very different: in the Lamb et al. model the surface temperature is always too high

in order to allow H–recombination. The opacity thus doesn't increase to the extent of making the envelope become convective and no dredge–up occurs. In the models by Brunish and Truran instead, a first dredge–up takes place, but only at the end of the core He–burning. No influence of the $^{12}C\ (\alpha\ ,\ \gamma\ )\ ^{16}O$ rate was found in our models as far as the shape of the HR diagram is concerned.

2. All the models by Lamb et al. (1976), Maeder (1981a,b), and those by Brunish and Truran (1982a) develop large convective shells just above the position of the maximum energy generation for shell–hydrogen burning during the central He–burning phase. In our model the hydrogen shell pratically ends at the base of the convective envelope.

3. At the end of He–burning the model by Lamb et al. is denser and hotter, but this might be due to the different cross sections for the 3α and $^{12}C(\alpha,\gamma)^{16}O$ reactions they adopted. They used the rates given by Fowler et al. (1971), which differ from the FCZ75 ones by:

$$\varepsilon_{3\alpha}(1971) \sim 0.65\ \varepsilon_{3\alpha}(1975)$$

$$\varepsilon_{co}(1971) \sim 1.48\ \varepsilon_{co}(1975)$$

(Notice that ε_{co} is roughly one half of the CFHZ85 rate).

A reduced He–burning efficiency implies a smaller expansion of the internal structure that is hence more compact and hotter.

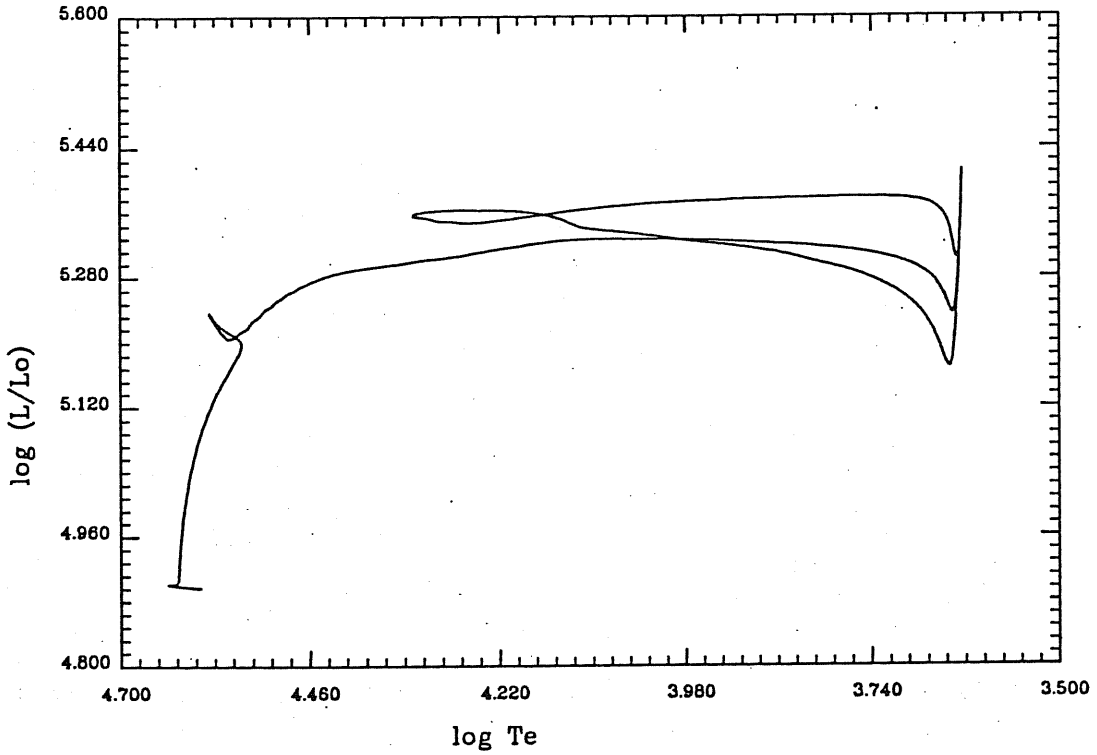

Figure 2.11: The HR diagram of the 25 $M_\odot$ pop.II star.

2.5 THE LOW METALLICITY CASE

We have investigated the effects of changing the initial chemical composition on the evolution of our 25 $M_\odot$ star, and as a first step, we have lowered Z down to 0.001, that is $\sim$1/20 of the solar–standard case, leaving Y fixed at 0.28. This gives us the possibility to make a test on the role of metallicity only. The first run was performed with the CFHZ85 thermonuclear reaction rates. Figure 2.11 shows the behaviour in the HR diagram of the new model, while figure 2.12 gives the evolution of the physical conditions from the ZAMS till the end of core helium burning and beyond.

Let us look at the HR diagram of our pop.II star (figure 2.11): the new track is always brighter and hotter in comparison to the standard one; moreover, it presents a blue loop extending up to $\log T_e = 4.329$ K. The star sets up on the ZAMS with $\log(L/L_\odot) = 4.901$, $\log T_e = 4.638$ K, $\log T_c = 7.639$ K, and $\log\rho_c = 0.816$ g/cm^3. It has a H–burning convective core of 12.99568 $M_\odot$. The hydrogen central burning lasts 6.107233 Myr, and when the convective core shrinks to zero, the star has $\log(L/L_\odot) = 5.207$, $\log T_e = 4.555$, $\log T_c = 7.931$ and $\log\rho_c = 1.721$ g/cm^3. The helium core is much greater than in the standard case: $M_\alpha = 7.945\ M_\odot$.

The ignition of the H–shell is violent as can be seen in figure 2.13, and a lot of energy is released, making the point in the HR diagram move towards the Hayashi

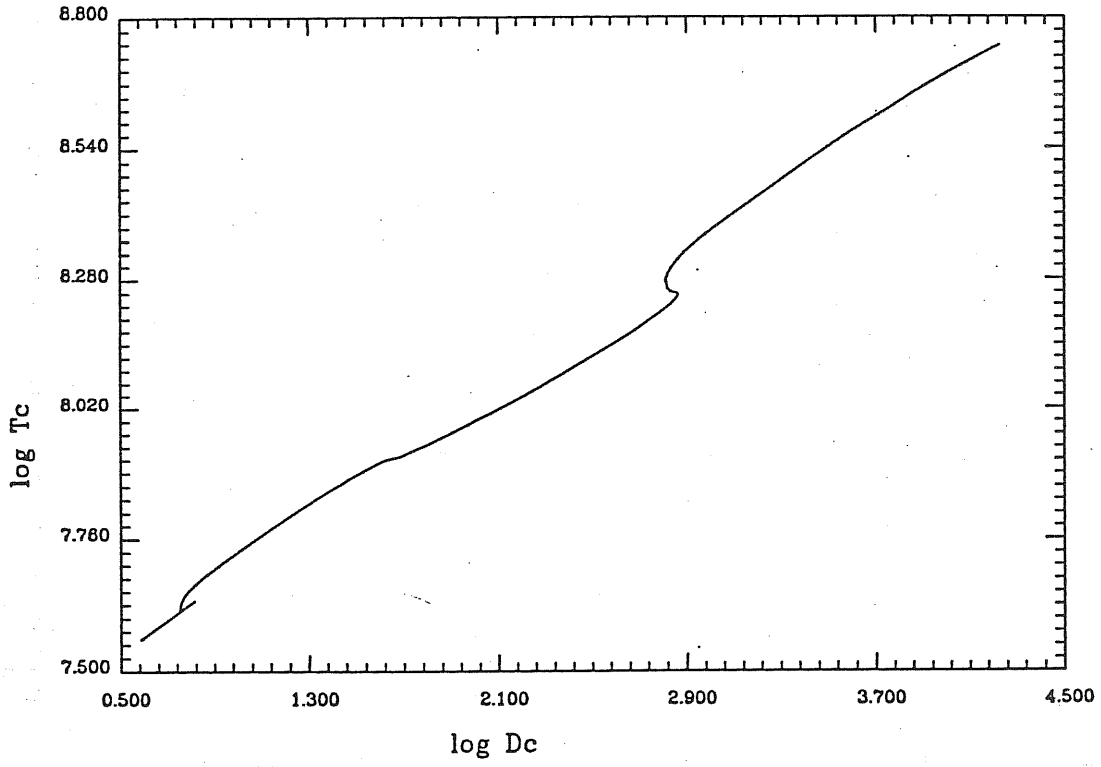

Figure 2.12: The evolution of the central conditions for the 25 $M_\odot$ pop.II star.

track; when it arrives at $\log(L/L_\odot) = 5.253$, $\log T_e = 3.645$ K the envelope becomes convective and starts to penetrate inward just as in the standard case. Now, however, we have a more efficient H–burning shell, and the star leaves the Hayashi track, pointing to the blue. It reaches a maximum extension of $\log T_e = 4.329$ K, then moves back to the red, exhausting He at $\log(L/L_\odot) = 5.355$, $\log T_e = 4.151$. The values of the central temperature and density are: $\log T_c = 8.542$ K, $\log \rho_c = 3.502$ g/ cm^3; we find here the same physical conditions as in the pop.I case! The helium–burning phase has lasted 0.6696247 Myr, that is, ~6% more than in the standard case; now $\Delta t_{He}/\Delta t_H = 0.1096445$. The maximum value of the convective core is $M_{cc}^{max} = 6.625\ M_\odot$, more than 8% larger than before. At He exhaustion, $M_\alpha = 9.508\ M_\odot$, while $M_{co} = 6.788\ M_\odot$, and the central abundances of carbon and oxygen are $X_C \simeq 0.13$, and $X_O \simeq 0.86$ respectively (figure 2.14).

When we repeated the run with the old FCZ75 rate for the $^{12}C\ (\alpha, \gamma)\ ^{16}O$ reaction we found the same features as for the pop.I case: the helium burning lifetime is decresed to 0.5869948 Myr, and the maximum of the convective core is $M_{cc}^{max} = 6.375\ M_\odot$. At helium exhaustion the surface luminosity and effective temperature and also the central temperature and density were the same as in the CFHZ85 model, but now $X_C = 0.46$ and $X_O = 0.53$, while $M_\alpha = 9.378\ M_\odot$ and $M_{co} = 6.398\ M_\odot$.Moreover, the blue loop in the HR diagram is slightly reduced, in agreement with what was found for Intermediate Mass Stars by Bertelli et al.

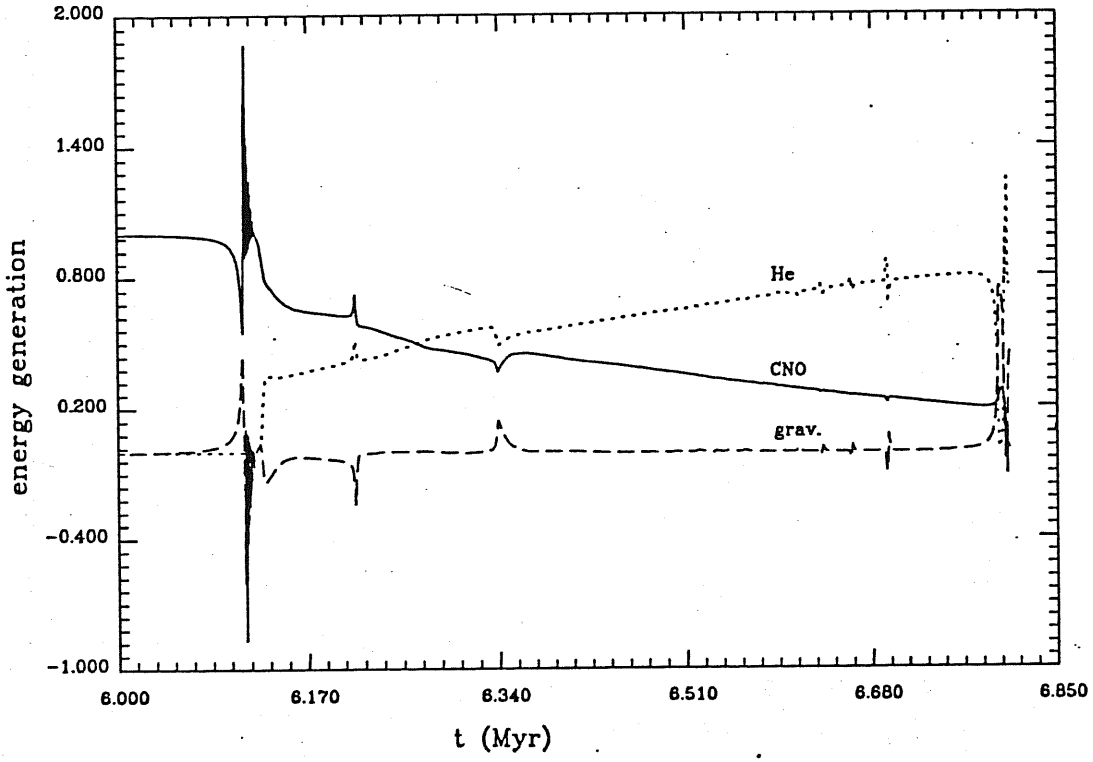

Figure 2.13: The energy generation for the 25 $M_\odot$ pop.II star from the end of the H–burning till past the end of He–burning.

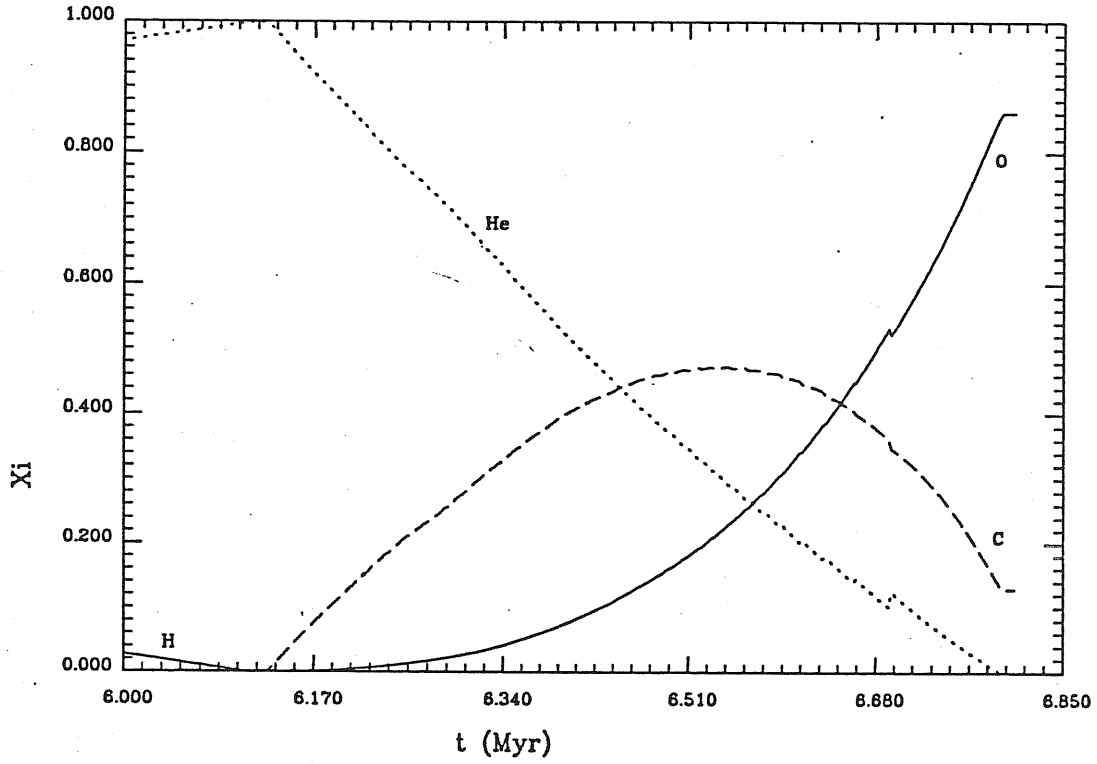

Figure 2.14: The evolution of the main chemical species (mass fractions) from the end of H–burning till past the end of He–burning for the 25 msun pop.II star.

(1985).

In the following run we also lowered the helium content, and thus we studied the case of a 25 $M_\odot$, $Y = 0.28$, $Z = 0.001$ star. Since this star has a much greater hydrogen initial abundance, the MS phase is longer, lasting about 6.7017703 Myr, that is $\sim$ 10% more than in the $Y = 0.28$ case, and the hydrogen–depleted core which is left is only $M_\alpha = 7.67084\ M_\odot$, $\sim$ 3% smaller because more time was available for the core to shrink. As a consequence, during core helium burning the duration and size of the central convective core are both reduced: the maximum value for the core mass is 6.38497 $M_\odot$ now, and the convective phase lasts 0.6758195 Myr.

At helium–exhaustion the physical parameters characterizing our star are: $\log(L/L_\odot) = 5.316$, $\log T_e = 4.045$, $\log T_c = 8.542$, $\log\rho_c = 3.520$ g/cm^3, $M_\alpha = 9.14212\ M_\odot$, and $M_{CO} = 6.35918\ M_\odot$. The central carbon and oxygen abundances by mass fraction are: $X_C \sim 0.15$, and $X_O \sim 0.84$.

There are not many calculations of low metallicity massive stars in the literature before the explosion of SN1987A in the Large Magellanic Cloud brought new interest on the subject.

We can compare our results with the work by Brunish and Truran (1982b), who followed the evolution of M = 15, 30, 40 $M_\odot$ stars with $Y = 0.28$ and metallicities of $Z = 0.01$, 0.001, 0.0002, and of a 50 $M_\odot$ star with $Z = 0.0002$ from the ZAMS up to the central helium exhaustion, with and without mass loss. They discussed the effects of a lower metal content on the evolution of massive stars, and were able to point out the following features:

- for a given evolutionary stage, the star is bluer, that is it has a higher effective temperature;
- while a 15 $M_\odot$ is brighter when Z is lower, the more massive stars experience a maximum in the luminosity in connection with some intermediate value of Z; Brunish and Truran found a correlation between luminosity and the maximum extension of the convective core at the beginning of H–burning: the greater M_{cc}^{max}, the more compact is the star in the center, the higher the central temperature and density and thus the brighter the star;
- the Main Sequence lifetime is longer around $Z = 0.001$ for every mass;
- all the models ignite helium as blue supergiants;
- there is a mass value for which the redward evolution during the helium burning phase is faster that depends upon the initial composition: if we decrease Z the slower going to the cool regions of the HR diagram happens for smaller masses;
- if the mass loss is a function of the effective temperature T_e, a reduced metal content implies a higher mass loss rate;

- the semiconvection reduction due to mass loss is more pronounced.

The behaviour of Brunish and Truran's tracks in the HR diagram are very different from ours: for $Z = 0.001$ the 15 $M_\odot$ and 30 $M_\odot$ stars move from the Main Sequence towards lower effective temperatures without becoming red giants and without looping during the helium burning. Anyway the stellar evolution in the HR diagram is a very delicate point, as the lot of computations of low metallicity massive stars which were made in the attempt of explaining why the SN1987A progenitor was a blue supergiant can confirm (see Weiss, 1989 for a critical review). Some comments above the possible causes which can play a role on the evolutionary tracks have already been done when discussing our pop.I model.

Chapter 3

THE s–PROCESS THEORY

3.1 THE NEUTRON–CAPTURE PROCESSES

The primordial nucleosynthesis following the Big Bang is believed to have created only hydrogen, helium and some other light nuclei with $A \leq 12$. The chemical enrichment of the Galaxy is due to nuclear processing occurring in the interiors of stars, converting H into He, He into C, and so on until iron is synthetized in the most massive stars. The processed material then goes into the interstellar medium through mass loss by stellar winds, ejection of a planetary nebula, or supernova explosion.

^{56}Fe is the most stable nucleus, so that a nuclear process involving the fusion of iron would be endoenergetic. Elements heavier than iron (the "heavy elements" in the language of the nuclear astrophysicists) can only be obtained by neutron–capture processes on iron seed nuclei, that do not require such high temperatures as charged particle reactions do (Burbidge et al., 1957).

Two kinds of this nucleosynthesis mechanism can be recognized: the s–process and the r–process.

In the s–process nuclei are built up along the stability valley in the chart of nuclides: (figure 3.1) starting from the iron seeds, stable nuclei capture neutrons while unstable isotopes decay, because they usually have beta decay rates greater than their neutron capture rates. At some points in the chain however, there are nuclei whose rates are comparable; in this case a branching in the s–process path occurs. Here the competition between capture and decay depends upon the physical conditions, and so the study of branching points can give information on the neutron density, the temperature, and the electron density during the nucleosynthetic event, and also test the kind of neutron irradiation that was responsible for it. This "slow" neutron capture process happens when neutron densities are small ($\sim 10^8$ cm^{-3}), as it is found during the hydrostatic He–burning phases of stellar evolution. The neutron–capture time scale is of the order of 1 to 10 yr. The smaller the neutron–capture cross section, the larger the abundance of the nucleus. If we look at the

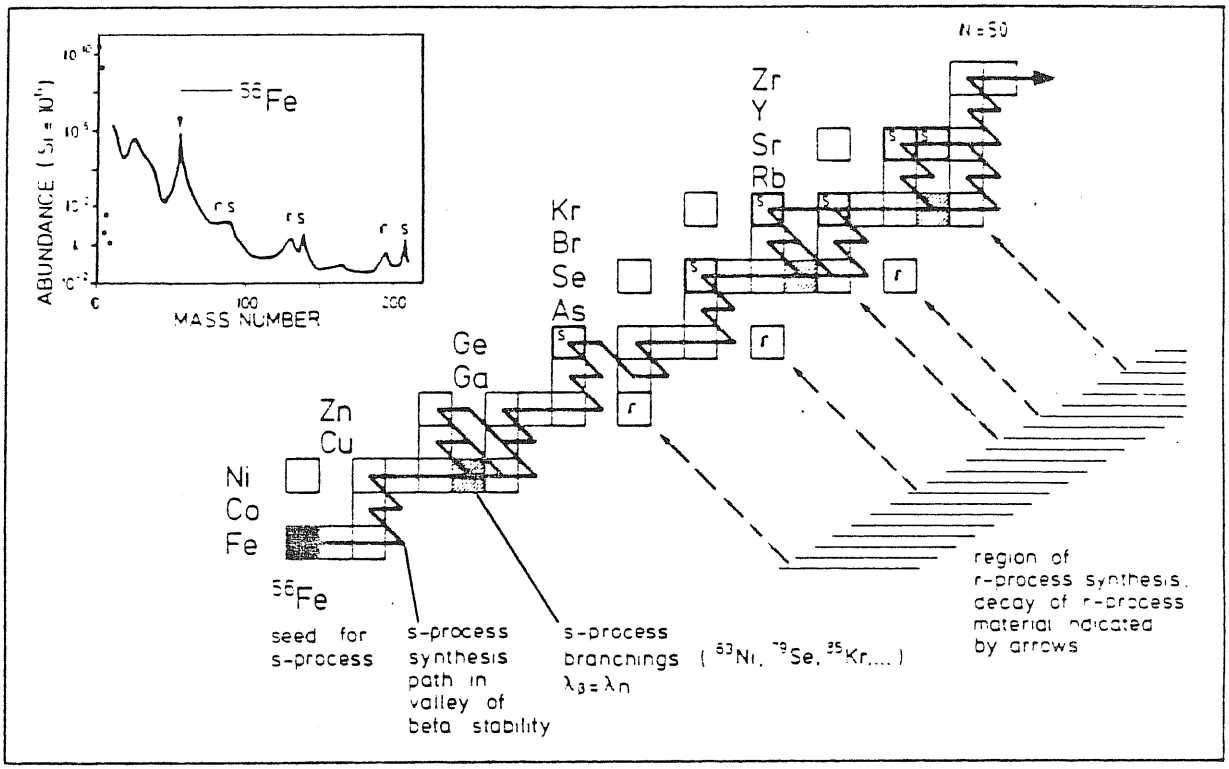

Figure 3.1: Section of the chart of nuclides for a discussion of the main features of neutron–capture nucleosynthesis. (Kappeler et al., 1989a)

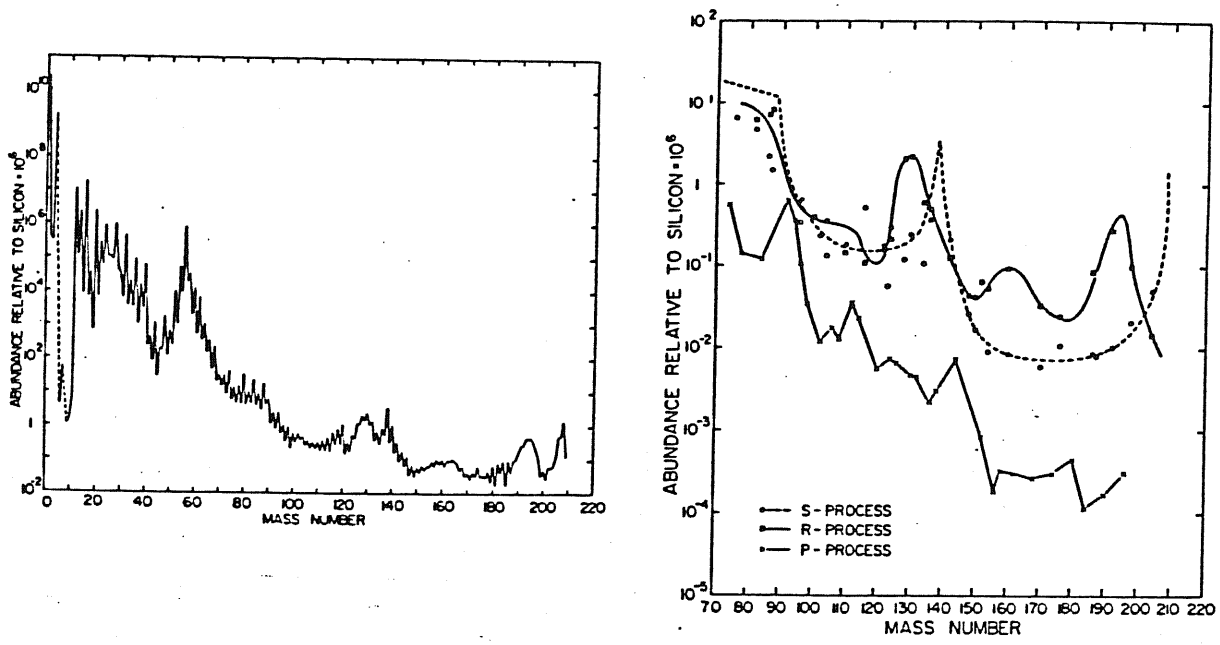

Figure 3.2: (a) Heavy–element abundances as a function of atomic mass . (b) Heavy–element abundances as a function of atomic mass approximately divided into (o)s–,(□)r– and (×)p–process contributions. (Cameron, 1982)

solar–system abundance versus atomic number plot (figure 3.2), we see that there are peaks corresponding to isotopes with a "magic" number of neutrons: $N = 50$, 82, 126 which correspond to closed neutron shells. They have particularly small cross–sections.

On the contrary, astrophysical sites must exist where "rapid" neutron captures on a time scale of some hundred milliseconds lead to the formation of very neutron–rich nuclei, that undergo a series of beta decays towards the stability valley as soon as the neutron irradiation stops. This is the mechanism of the r–process which requires large neutron densities ($\sim 10^{20}$ cm^{-3}) and presumably takes place in connection to the supernova phenomenon. r–isotopes with a magic neutron number have longer half–lives so they pile up and determine the r–peaks in figure 3.2 that slightly precede the s–peaks.

Most of the heavy elements receive both s– and r– contributions, but as we can see from figure 3.1, if the cascade of beta decays following a rapid irradiation meets a stable nucleus, that one will be a r–only isotope, and it stands as a screen for a corresponding isobar, which thus receives only the s–contribution: a s–only nucleus will result. The aim of s–process calculations is precisely to reproduce the solar–system abundance distribution of these s–only nuclei.

There are also some proton–rich nuclei that are out of reach from both s– and r– processes. They are attributed to the so–called p–process, where "p" stands for proton–capture and/or photodisintegration. They are generally neglected when the heavy elements nucleosynthesis is analized because their abundances are very low

and the mechanism of their synthesis very poorly known. Anyway, the p–process is supposed to affect the production of some nuclei of prevailing other origin too, and p–process corrections to the s–only isotopes must be taken into account when a deep investigation of the s–process is under way.

Clayton et al. (1961) showed that if we plot the product of cross section times abundance as a function of the atomic weight A, we see that σN_s is a smooth and decreasing function, whereas σN_r shows uncorrelated scatter. This strongly supports the idea that s– and r– processes have to be studied as separate nucleosynthetic events. Moreover, they demonstrated that a single neutron irradiation was not suitable for reproducing the empirical σN_s curve, while some years after Seeger et al. (1965) found that an exponential distribution of neutron exposures on seed material better fitted the solar data.

The seed material is commonly referred to as iron group nuclei, because they have abundances which are comparable to the more abundant lighter elements, and also have larger neutron capture cross sections, so that the heavy nuclei are easier to synthetize starting from iron than from the light elements.

Let us examine the s–process in more details now.

3.2 THE CLASSICAL MODEL

3.2.1 The Exponential Exposure Distribution Model

The classical analysis of the s–process is a phenomenological approach which aimes to reproduce the s–only isotopes solar distribution, not caring about the astrophysical circumstances which make the mechanism work. Owing to the neutron–capture event, the abundance of an isotope with atomic weight A changes according to:

$$\frac{dN_s(A)}{dt} = \lambda_n(A-1)N_s(A-1) - [\lambda_n(A) + \lambda_\beta(A)]N_s(A), \qquad (1)$$

where $\lambda_\beta = ln2/T_{1/2}$ is the beta–decay rate if the nucleus A is radioactive, and λ_n is the neutron capture rate:

$$\lambda_n = N_n(t) < \sigma v >;$$

N_n is the neutron density, and $< \sigma v >$ is the product of the neutron capture cross section times the relative velocity of neutron and target, averaged over a Maxwell–Boltzmann distribution:

$$< \sigma v >= \int_0^\infty \sigma\, v\, \Phi(v)\, dv,$$

with

$$\Phi(v)\, dv = \frac{4}{(\pi)^{1/2}} \left(\frac{v}{v_T}\right)^2 exp[-\left(\frac{v}{v_T}\right)^2] \frac{dv}{v_T}.$$

v_T is the thermal neutron velocity:

$$v_T = \left(\frac{2KT}{\mu_n}\right)^{1/2},$$

with μ_n being the neutron reduced mass. Since for most nuclei the differential cross section $\sigma \sim v^{-1}$, the product σv is almost independent of the temperature, and so we can assume $< \sigma v >=< \sigma > v_T$. In order to find an analytic solution to the set of coupled differential equations (1), the classical analysis must make some assumptions:

- depending on the relative value of λ_n and λ_{β^-}, radioactive nuclei are treated as stable nuclei or they are completely neglected; branching points are treated in a separate way;
- the temperature is kept constant in order to deal with well defined cross sections and decay rates;
- a steady neutron flux is assumed.

Then, if we define the *time integrated neutron flux* τ as:

$$\tau \equiv \int N_n(t)\, v_T\, dt,$$

the system of equations becomes:

$$\frac{dN_s(A)}{d\tau} = \sigma(A-1)N_s(A-1) - \sigma(A)N_s(A), \tag{3.1}$$

and can be solved analytically in terms of an exponential distribution of neutron exposures τ of the kind:

$$\rho(\tau)\, d\tau = G\, exp(-\tau/\tau_0)\, d\tau,$$

where $\rho(\tau)d\tau$ is the number of iron seed exposed to an integrated flux τ in the interval $d\tau$. If the neutron irradiation is long enough, equilibrium between production and destruction can be reached, and equation 3.1 leads to a constant σN_s value. In a more general context, the σN_s product will be a smooth function of the atomic number.

It is believed that two components are necessary to correctly describe the s–process (Ward and Newman, 1978):

- the *main component*, which is responsible for the synthesis of the isotopes with atomic mass number $A > 90$;
- the *weak component*, that accounts for the formation of isotopes in the atomic mass range 60–90.

A third component may be required to reproduce the s–abundances at the lead–peak, but the existence of this *strong component* and its s–process model are under discussion.

For a two–component distribution of the form:

$$\rho(\tau) = \frac{f_1 N_{56}}{\tau_{01}} exp(-\tau/\tau_{01}) + \frac{f_2 N_{56}}{\tau_{02}} exp(-\tau/\tau_{02}),$$

the classical (unbranched) solution is given by:

$$\sigma(A)N_s(A) = \frac{f_1 N_{56}}{\tau_{01}} \prod_{i=56}^{A} \left[1 + \frac{1}{\sigma(i)\tau_{01}}\right]^{-1} + \frac{f_2 N_{56}}{\tau_{02}} \prod_{i=56}^{A} \left[1 + \frac{1}{\sigma(i)\tau_{02}}\right]^{-1} \tag{3.2}$$

if α–recycling among the isotopes of lead and bismuth is neglected. f_i is the fraction of the iron seed nuclei N_{56} that have been subjected to the i–component of the exponential distribution of exposures; τ_{0i} is the mean neutron exposure. Both f_i and τ_{0i} must be determined by fitting the empirical σN_s values in the following way: the main component is determined by a least square fit in the $A > 100$ range, where

the contribution of the weak component is negligible. Once the parameters f_2 and τ_{02} have been found, another fit for $A < 97$ allows f_1 and τ_{01} to be obtained.

Note that in equation 3.2 only those nuclei with small cross sections can give significant contributions and will play a major role in modelling the σN_s curve. As we said before, these are nuclei with a magic number of neutrons.

Kappeler et al. (1982) obtained a best fit with

$$f_1 = (2.7 \pm 0.2)\%, \qquad \tau_{01} = 0.056 \pm 0.005\ mb^{-1}$$

for the weak component, and

$$f_2 = (0.092 \pm 0.015)\%, \qquad \tau_{02} = 0.24 \pm 0.01\ mb^{-1}$$

for the main one.

In a subsequent paper (Kappeler, 1986) an improved calculation using updated solar–system abundances and cross sections led to increased mean neutron exposures and reduced fractional seed abundances. The new estimated parameters are:

$$f_1 = 1.6\%, \qquad \tau_{01} = (0.068 \pm 0.007)\left(\frac{KT(KeV)}{30}\right)^{1/2} mb^{-1}$$

and

$$f_2 = (0.043 \pm 0.002)\%, \qquad \tau_{02} = (0.30 \pm 0.01)\left(\frac{KT(KeV)}{30}\right)^{1/2} mb^{-1}.$$

Figure 3.3 shows the resulting σN_s curve, that is now considered as accurate within 10% : the main component is plotted as a thick solid line showing the contribution of the weak component explicitely.

In the same paper, a possible scenario for the strong component was also given, where a very low fractional seed abundance $f = 1.2 \times 10^{-4}$ experiences a neutron–capture process with a very high mean neutron exposure $\tau_0 = 7.0\ mb^{-1}$.

3.2.2 The Single Flux Model

If it is accepted that the main component is better reproduced by an exponential distribution of neutron exposures (Kappeler et al., 1982; Kappeler, 1986; Beer, 1986), difficulties in the final yields of some isotopes make this assumption questionable for the weak s–flow: as a matter of fact the two s–only isotopes ^{70}Ge and ^{76}Se are underproduced, while ^{58}Fe, ^{92}Zr and ^{94}Zr are overproduced.

Recently Beer and Macklin (1989) (but see also Beer, 1986) have found that a single–exposure s–process with a time integrated flux

$$\tau = (0.23 \pm 0.03)(KT/30)^{1/2}\ mb^{-1}$$

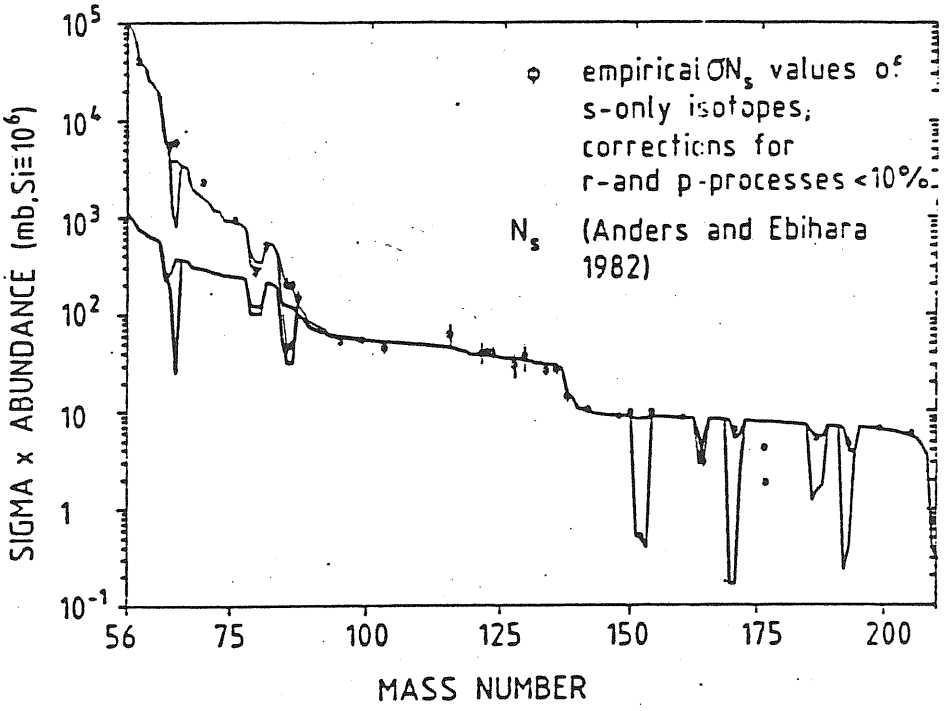

Figure 3.3: The characteristic product of cross section times s-process abundance versus mass number. Symbols with error bars denote the empirical products of pure or almost pure s-isotopes. (Kappeler et al., 1989a)

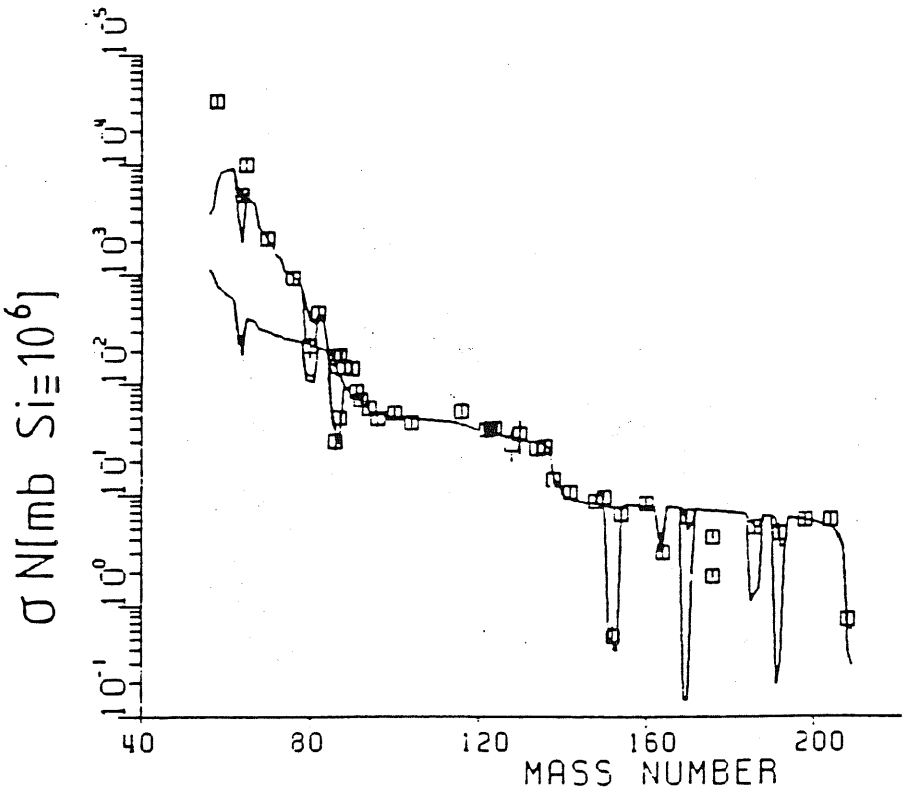

Figure 3.4: Product of capture cross section and s–process abundance as a function of mass number A. Symbols are empirical data. Below $A = 90$ the superposed weak component is effective, as given by the single flux model. (Beer and Macklin, 1989)

and a fraction of iron seeds $N(^{56}Fe)/N_{\odot}(^{56}Fe) = 0.0026 \pm 0.0014$ gives a better fit to the empirical data in the $A < 90$ range. But, as can be seen in figure 3.4, the single flux approximation falls short in reproducing the ^{58}Fe abundance: only $\sim 20\%$ of the solar value can be obtained. It is true that the ^{58}Fe synthesis is a questionable subject. Some attempts have been made to justify its production during neutron–rich equilibrium processes, but the best choice is probably to assume it as totally produced by the weak component of the s–process (Kappeler et al., 1982).

A single flux model can also be formulated for the strong component of the s–process. In this case, the fraction of iron seed that is needed in order to reach the lead and bismuth atomic weights is 0.9×10^{-4}, and the time integrated neutron flux is given by $\tau \geq 2.5$ (Beer, 1986).

3.2.3 The Neutron Absorption

It is common to describe the s–process efficiency by calculating the number of neutrons captured per ^{56}Fe seed nucleus (Clayton et al., 1961):

$$n_c(A_{seed}) \equiv \frac{\sum_{A=A_{seed}}^{209}(A - A_{seed})N_s(A)}{fN_{56}} = \sum_{A=A_{seed}}^{209} \frac{(A - A_{seed})}{\sigma(A)\tau_0} \prod_{j=56}^{A} \left[1 + \frac{1}{\sigma(j)\tau_0}\right]^{-1},$$

where the last term results from using an exponential distribution of neutron exposures $\rho(\tau)$. Many investigations of the s–process have referred to $n_c(56)$ ("n_c" by default), that is the number of neutrons captured by the heavy nuclei starting from ^{56}Fe, per ^{56}Fe seed nucleus. Typical values that were found according to the exponential exposure distribution approximation are 11.2 ± 0.7 for the main component; 1.4 ± 0.4 for the weak component, and $\simeq 150$ for the strong one.

But the total number of neutrons captured during the s–process is $\sum_i n_c(i)$, where i runs over all seeds. Since a lot of light elements have showed to be very strong neutron absorbers, behaving as poisons for the s–process, they must be taken into account when the neutron economy of the nucleosynthetic mechanism is discussed as a whole.

Assuming a fraction f of light nuclei (the same as for the heavy nuclei) and running the summation from $i = 20$ to $i = 56$, Kappeler et al. (1989a) indicate a value for $\sum_i n_c(i)$ of 18.2 ± 1.3 for the main component, and of 23.1 for the weak component, while in the case of the strong component $\sum_i n_c(i) = 141$.

So the difference between n_c and $\sum_i n_c(i)$ is not so large for the main component, but it is dramatic for the weak one, showing the fundamental role of the light poisons in this process. Finally, it seems reasonable to have values of the same order for the strong component, since were a good poisoning effect from the light elements found, it would be extremely difficult to produce lead.

3.3 THE BRANCHING ANALYSIS

The analitic description of the s–nucleosynthesis occurring at branching points is due to Ward et al.(1976); it is very useful to define the *branching factor*

$$f_{=}\frac{\lambda_{\beta^-}}{\lambda_{\beta^-}+\lambda_n}, \tag{3.3}$$

that is the fraction of the neutron flow that goes through the β^- decay channel instead of the neutron capture one. In the same way we can define f_+ for the β^+ (or electron capture) weak interactions. Of course, the possibility exists that both processes are involved in a branching. In this case all the rates must appear in the denominator of 3.3.

The classical analysis describes the neutron flow through a branching nucleus by means of propagators. Let us consider a simple case in which a nucleus with atomic mass number A and Z protons (A,Z) can either capture a neutron or β^- decay into the $(A,Z+1)$ nucleus. Then, for the neutron–capture channel we have:

$$\sigma N(A,Z)=\zeta(A,Z)\sigma N(A-1,Z),$$

where

$$\zeta(A,Z)=\left[\frac{1}{1-f_-(A,Z)}+\frac{1}{\tau_0\sigma(A,Z)}\right]^{-1}\sigma N(A-1,Z)$$

is a propagator. For the beta decay channel the solution is instead:

$$\sigma N(A,Z+1)=\eta(A,Z+1)\left\{\frac{f_-(A,Z)}{1-f_-(A,Z)}\right\}\sigma N(A,Z),$$

with

$$\eta(A,Z+1)=\left[1+\frac{1}{\tau_0\sigma(A,Z+1)}\right]^{-1}.$$

If we consider branching points that do not depend on the temperature, λ_{β^-} has a well–defined value; then by a fit to the empirical σN_s curve, f_- can be obtained and hence λ_n , that is the neutron density, can be derived by the definition 3.3. This is the case for ^{85}Kr, ^{147}Pm, ^{148}Pm, ^{169}Er and ^{185}W.

Branchings that do depend on temperature such as ^{79}Se, ^{151}Sm and ^{191}Os, on the other side, can be used as thermometers, once the neutron density is known.

3.3.1 Evaluation Of The Neutron Density

The best branching point to derive a value for the neutron density of the main component is probably that occurring at ^{185}W (see figure 3.5). As a matter of fact,

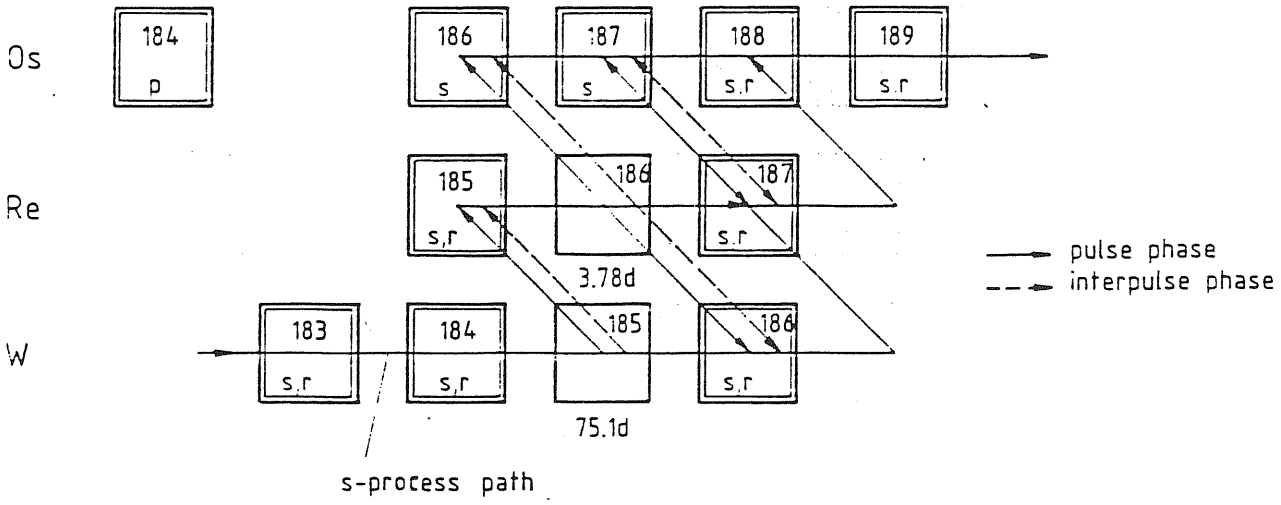

Figure 3.5: The neutron–capture path through W and Os. (Beer and Macklin, 1988)

the ^{185}W half–life is almost independent of temperature, and by fitting the empirical ratio $\sigma N_{\odot}(^{186}\mathrm{Os})/\sigma N(^{184}\mathrm{Os}) = 0.77 \pm 0.09$ a neutron density

$$N_n^{main} = (1.3 \pm 0.7) \times 10^8\ cm^{-3}$$

was obtained by Beer and Macklin (1988). The estimated uncertainty on this value is 55%, but the authors above claimed that it is however more reliable than the result reported by Winters et al. (1986) of $N_n^{main} = (1.0 \pm 0.4) \times 10^8\ cm^{-3}$ derived via the ^{148}Pm branching, which hides a problem on how to treat one of its isomeric states.

In order to calculate the neutron density for the weak component, Klay and Kappeler (1988) studied the ^{85}Kr branching (figure 3.6). It is worth to remind that in this region of atomic weight both the main and the weak contributions are involved. So they first fitted the main component with a steady neutron flux of $N_n = 1.3 \times 10^8$ cm $^{-3}$ at a temperature of KT = 23 KeV. Then they considered the region from ^{58}Fe to ^{88}Sr to determine the weak component. From the ^{85}Kr branching a neutron density of:

$$0.8 \leq N_n^{weak}/10^8 cm^{-3} \leq 1.9$$

was derived. Smaller values would strengthen the β–decay channel leading to an overproduction of ^{86}Sr, whereas larger values would enhance the neutron capture, and ^{86}Kr would be overproduced.

Notice that N_n^{weak} strongly depends on the assumptions made for the main component. As a matter of fact, were the ground state and the 137 KeV isomer in

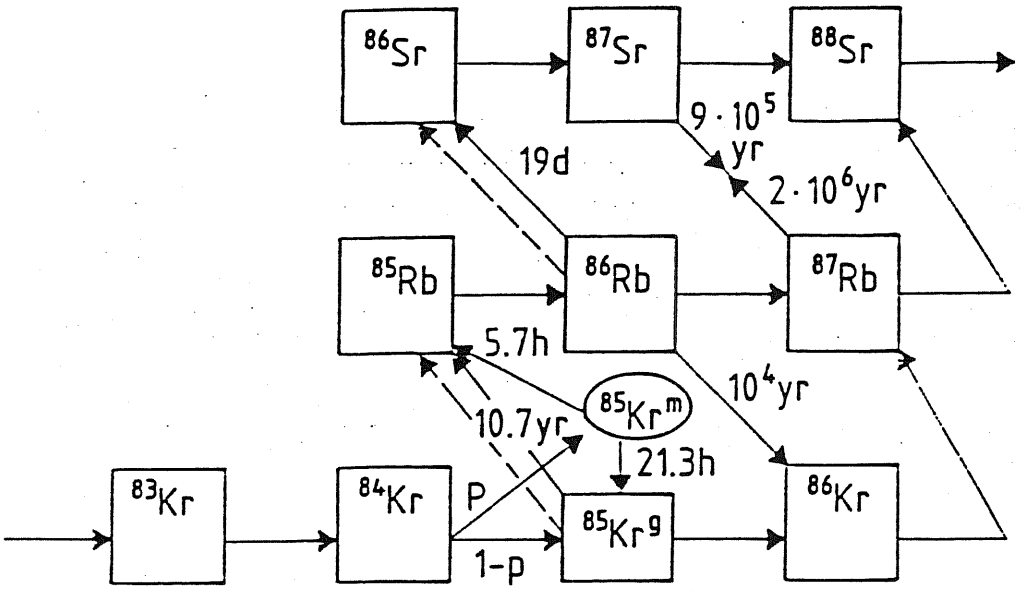

Figure 3.6: The neutron–capture path through Kr and Sr. (Beer and Macklin, 1989)

^{148}Pm thermally equilibrated, the parameter space for the main component would center around $N_n^{main} = 2.5 \times 10^8\ cm^{-3}$ and KT = 27 KeV, and this would imply lower neutron densities for the weak component.

3.3.2 The Thermometers

Starting from the evaluation of the neutron density for the main component, Beer and Macklin (1988) analized the ^{151}Sm branching in order to derive the temperature by reproducing the solar ratio $\sigma N(^{152}\mathrm{Gd})/\sigma N(^{154}\mathrm{Gd})$ (figure 3.7). They estimated a temperature ranging from 18 up to 29.5 KeV for the main component, that is:

$$209 \leq T_{main}/(10^6 K) \leq 342.$$

As for the weak component, in the paper by Klay and Kappeler (1988) the behaviour of the ^{79}Se decay–rate as a function of the temperature was estimated. Since competition between neutron–capture and beta decay at ^{79}Se determines the relative abundances of ^{80}Kr and ^{82}Kr, in order to reproduce the empirical σN, values of these two isotopes an half–life of 2.3–16 yr for ^{79}Se has to be postulated and this implies a temperature for the weak component of 16–25 KeV, or:

$$182 \leq T_{weak}/(10^6 K) \leq 295.$$

Anyway, as pointed out by Beer and Macklin (1989), the fact that neutron density and temperature for the weak flow are found to be similar to those for the main process depends on the model, that is on the assumption of exponential exposure distributions and continuous neutron irradiations for both components.

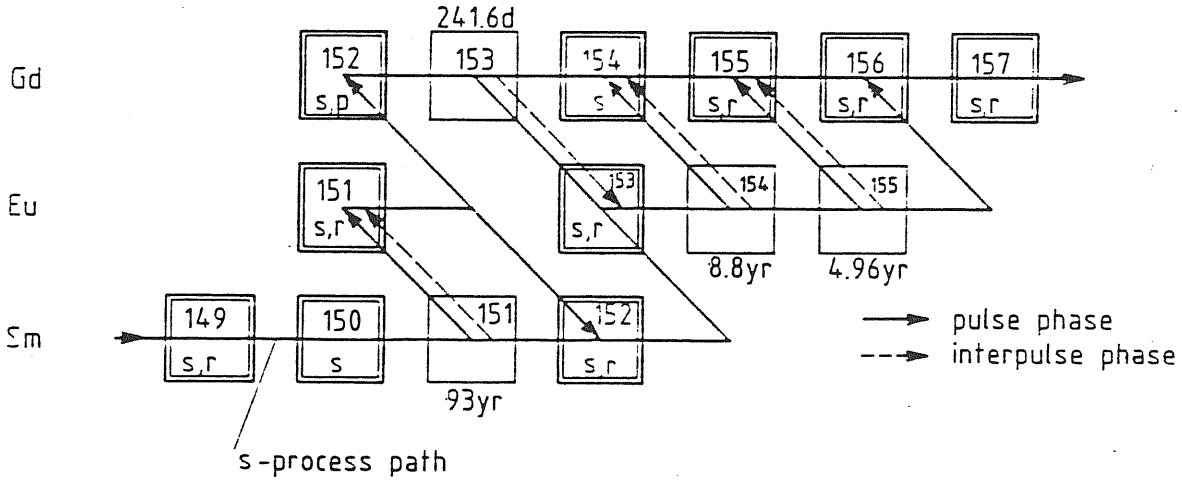

Figure 3.7: The neutron–capture path through Sm and Gd . (Beer and Macklin, 1988)

3.3.3 The Barometers

The electron capture rates in the highly ionized stellar plasma are dominated by capture of continuum electrons, and hence depend on the electron density. Since the electron to barion ratio is almost exactly 0.5, we can calculate the mass density from a branching whose unstable nucleus is characterized by such a density dependent electron capture rate. Beer et al. (1985) discussed the ^{163}Dy–^{163}Ho branching, from which the ^{164}Er production depends through the ^{163}Dy $(\beta^-)^{163}$Ho (n, γ) ^{164}Ho $(\beta^-)^{164}$Er reaction chain. In order to reproduce the ^{164}Er abundance, a certain value of the branching factor is required, which depends on the relative rate of beta decay of ^{163}Dy and electron capture on ^{163}Ho, that is on the electron density. This is found to be $n_e \simeq (0.8 - 4) \times 10^{27}$ cm $^{-3}$, corresponding to a matter density of 2600–13000 g/cm^3 for the He–burning environment of the main s–process component.

3.3.4 The Pulsed s–Process

Talking about branchings, we would like to mention that some of them are affected by the kind of the adopted neutron exposure (Ward and Newman, 1978; Beer, 1986; Beer and Macklin, 1988, 1989).

If we consider a pulsed neutron flux as suggested by the stellar models for the main s–process (see below) instead of a continuous irradiation, the unstable branching–point nucleus may decay in the time interval between two successive neutron exposures. During the following irradiation it has to be built again and this process is controlled by the strength and width of the neutron burst.

The branching points that are sensible to this effect are those for which the total life time $\tau_{tot} = (\lambda_n + \lambda_\beta)^{-1}$ is shorter than or comparable to the neutron irradiation Δt. For $\Delta t \ll \tau_{tot}$ the branching does not exist at all, and the branch point isotope behaves like a short lived radioactive nucleus, whereas for $\Delta t \gg \tau_{tot}$ the effect of the pulsation disappears and the conditions of the continuous classical s–process are reached.

In the limit of a sufficiently large number of pulses, a steady state is achieved where the pulsed results can be calculated from the classical ones by additional terms proportional to preceding branch–point isotopes. These additional terms will contain factors in which the dependence on the pulse width Δt and the interpulse time t_{ip} are included. The shape of the pulse is assumed rectangular, which is a simplification of the real physical conditions occurring inside stars.

From the analysis of some characteristic branchings, Beer (1986) and Beer and Macklin (1988, 1989) were able to deduce the pulse duration for the main component, which is in the range of 3–25 yr.

They started from the classical solution, characterized by the following parameters:

$$N_n = 1.3 \times 10^8 cm^{-3}; \qquad KT = 23 K\epsilon V; \qquad n_e = 2 \times 10^{27} cm^{-3} \qquad (3.4)$$

which is assumed as the asymptotic solution for the pulsed model when very large exposures per pulse are considered, and the effect of the pulsed irradiation was investigated by comparing the σN_s values for ^{152}Gd, ^{154}Gd and ^{186}Os (which depend on the branchings at ^{151}Sm, ^{153}Gd, ^{154}Eu and ^{185}W) with the empirical ones.

As is shown in figure 3.8 the lower limit for Δt is given by ^{152}Gd, which would be overproduced for pulse widths shorter than 3 yr.

Since there is more than one parameter involved (N_n, T, Δt), we would think that more than one solution may be found beside that given by (3.4). But this is not true, because if we vary the physical parameters, we can't get a common solution for all the branchings analized (Beer and Macklin, 1988). The classical s–process solution thus seems to be the most likely asymptotic solution for the pulsed s–process.

In order to place an upper limit to the pulse width, the ^{85}Kr and ^{86}Rb branchings were studied. The ^{86}Kr abundance, which is determined by these branchings, strongly urges on the adoption of a pulsed mechanism for the main component, since within the classical model ^{86}Kr is too much produced.

Beer and Macklin (1989) stated that the uncertainties affecting the various parameters do not allow to deduce an upper limit for the pulse width, but a value below 25 yr should always lead to a consistent description of the critical ^{86}Kr abundance.

It is worth to stress that the s–main contribution to the ^{79}Se and ^{85}Kr branchings, the only two points where information on the weak component can be derived, strongly depends on whether a pulsed model or a continuous flux one is assumed. In other words, a pulsed main s–process is expected to affect the weak component description given by the classical analysis.

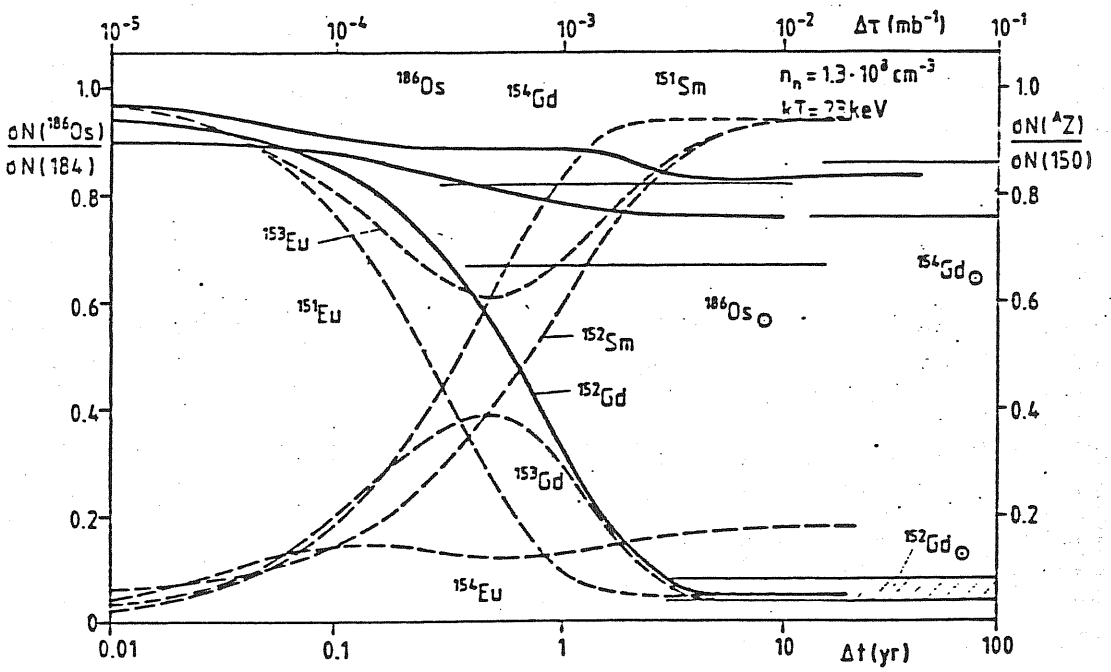

Figure 3.8: Normalized σN values for the isotopes discussed in the text, as a function of the pulse width Δt and the exposure per pulse $\Delta\tau$. The isotopes for which empirical values indicated by hatched areas can be given are drawn as solid lines. (Beer and Macklin, 1988)

3.4 THE ASTROPHYSICAL SITES

3.4.1 The Neutron Sources

Observations of surface abundances in red giant stars have revealed the presence of s–elements as well as a carbon enhancement. This strongly supports the idea that the s–process occurs during the helium burning stages of stellar evolution, and that the processed material is then brought to the surface by some dredge–up or mixing mechanism.

The best candidate nuclear reactions that can produce neutrons during He–burning are the ^{13}C (α, n) ^{16}O and ^{22}Ne (α, n) ^{25}Mg reactions (Cameron, 1955; Burbidge et al., 1957; Reeves, 1966).

The first one becomes efficient at relative low temperatures ($T \simeq 1.5 \times 10^8$ K), but requires some mixing of protons with the helium burning processed material to be possible in order to get ^{13}C through the chain:

$$^{12}\mathrm{C}\ (\mathrm{p}\ ,\gamma)\ ^{13}\mathrm{N}\ (\beta^+\ \nu)\ ^{13}\mathrm{C}.$$

On the contrary, ^{22}Ne is naturally obtained at the beginning of He burning, when all the ^{14}N which was synthetized by the CNO cycle during the preceding hydrogen burning phase is transformed into ^{18}O first, and into ^{22}Ne then, via the reaction path:

$$^{14}\mathrm{N}\ (\alpha\ ,\gamma)\ ^{18}\mathrm{F}\ (\beta^+\ \nu)\ ^{18}\mathrm{O}\ (\alpha\ ,\gamma)\ ^{22}\mathrm{Ne}.$$

The ^{22}Ne neutron source starts to be effective when higher temperatures are reached ($T \geq 2.2 \times 10^8$ K).

If we consider stars that are massive enough to experience further nuclear burnings besides the helium one, we first notice that not the whole ^{22}Ne supply might be burnt during the helium burning episode, and some neutrons could be released through the ^{22}Ne(α,n) ^{25}Mg source at the beginning of carbon burning (Arcoragi, 1986). However, Gallino and Busso (1985) estimated a neutron density of $N_n \geq 5 \times 10^{12}$ cm^{-3} in this case. Under such conditions, the average neutron capture time scale of some unstable nuclei becomes lower than the corresponding β–decay lifetime, and a n–process intermediate between the s– and the r– ones is believed to occur.

Then, at the low temperatures ($T \leq 8 \times 10^8$ K) characterizing core carbon burning in stars less massive than $\sim$ 15 $M_\odot$, Arnett and Thielemann (1985) found that the reaction sequence ^{12}C(p,γ)^{13}N (β^+)^{13}C(α,n)^{16}O, sustained by protons and α particles from the ^{12}C+^{12}Cfusion reaction, is a powerful neutron source.

Other neutron sources could also be found, such as the ^{12}C (^{12}C, n) ^{23}Mg reaction during carbon burning, or the ^{16}O (^{16}O, n) ^{31}S one during oxygen burning. But these reactions require such high temperatures ($T \geq 10^9$) that the neutron–capture path of the s–process promoted by them is expected to yield a non–solar σN_s curve.

Moreover, this s–processed material would probably be confined inside the compact stellar remnant which is the final product of the massive star life, and thus would not be allowed to give a contribution to the chemical enrichment of the interstellar medium.

Higher temperature burning stages can be ruled out as possible sites for neutron–capture, since above T$\sim 20\times10^8$ K (γ , n) reaction rates begin to exceed the neutron capture rates.

3.4.2 The Weak Component

It has long been recognized that massive stars during the central He–burning stages of their lives can produce heavy nuclei up to $A \sim 90$ through the ^{22}Ne (α, n) ^{25}Mg neutron source (Couch et al., 1974; Lamb et al., 1977; Gallino and Busso, 1985; Arnett and Thielemann, 1985; Busso and Gallino, 1985; Prantzos et al., 1987; Langer et al., 1989).

The efficiency and the details of the process as reported by the various works on the subject were not always in agreement, but this is due to the fact that the nucleosynthesis mechanism depends on so many evolutionary as well as nuclear parameters, which are continuously improving with time.

Anyway, as we shall extensively discuss in the following sections of this thesis, the astrophysical model for the weak component can be forced neither into a single flux nor into an exponential exposure distribution model. Indeed, we shall see that a whole spectrum of single neutron irradiation episodes occurring under realistic – that is dynamic – physical conditions must be taken into account if we want to explain the solar abundances curve.

3.4.3 The Main Component

The main component was traditionally ascribed to the thermal instabilities which develop in intermediate mass stars ($3\leq M/M_\odot \leq 8$) during the Asymptotic Giant Branch (AGB) phase of their evolution. Here, during the He–shell burning, neutrons are released through the ^{22}Ne (α , n) ^{25}Mg reaction, and the overlapping of the periodic convective pulses that develop in the shell provide for an exponential distribution of neutron exposures (Ulrich, 1973) which was found to reproduce the solar system distribution of the heavy elements (Iben, 1975; Truran and Iben, 1977; Cosner et al., 1980).

This scenario has recently been argued against (Busso et al., 1988, and references therein) in the light of new calculations with updated nuclear inputs, which strongly reduce the s–processing efficiency. Moreover, the observational counterparts of such bright models have not been found in significant number in the Magellanic Clouds, and no strong overabundances of ^{25}Mg and ^{26}Mg isotopes have been observed in those stellar atmospheres showing enhancements of s–process elements.

In low mass stars the ^{22}Ne source is slightly effective because of the lower temperatures involved, but Iben and Renzini (1982a,b) showed that at least for the low metallicity stars ($Z = 0.001$) an alternative neutron source can be provided by the ^{13}C (α , n) ^{16}O reaction. As a matter of fact, following a thermal pulse, the outer edge of the carbon rich zone expands to such temperatures that carbon recombination occurs. This leads to an increase of the opacity, and a semiconvective region develops just below the envelope, which mixes hydrogen–rich matter with carbon–rich material. During the subsequent evolution this region heats up and ^{12}C is converted into ^{13}C and ^{14}N by an incomplete CN cycle. A ^{13}C–rich pocket forms which will be ingested by the following pulse, allowing the liberation of a neutron flux. A confirmation of the effectiveness of this mechanism was obtained by Hollowell and Iben (1988, 1989), who found that the ^{13}C–rich pocket is created in stars with metallicities up to 6×10^{-3}.

Gallino et al. (1988), Gallino (1988), and Kappeler et al. (1989b) have recently investigated the s–process nucleosynthesis in such low mass stars following both the Iben and Renzini and the Hollowell and Iben models. They found strong overabundances for all the s–isotopes with $A > 80$ in a solar system distribution, and a substantial agreement with the classical s–analysis results.

3.4.4 The Strong Component

At the moment, it seems as if a strong s–process mechanism has to operate in order to give account of the 30% missing abundance of ^{208}Pb, the s–only isotope at the termination of the s–path. The most promising site for this strong component up to now was identified in the core helium flashes experienced by low mass stars ($M \leq 1\ M_{\odot}$) at He–ignition (Truran and Iben, 1977). This scenario has not been investigated in details yet, and we can't be sure that a single event rather than more than one is needed to best fit the empirical data. We only know that the neutron source has to be the ^{13}C (α, n) ^{16}O reaction, since the temperature is too low for the alternative ^{22}Ne source to be effective.

Another suggestion for the synthesis of ^{208}Pb has very recently been advanced (Gallino et al., 1989): according to this scenario, the strong component might occur in low mass, low metallicity stars during the He–shell thermal pulses they undergo while ascending the AGB. The mechanism in a word would be the same that, for higher metallicities, allows the main component to be obtained, but now the same amount of neutrons (that depends on the ^{13}C–rich pocket which is of primary origin and thus metal independent) is to be distributed on a lower seed content. The result is that a ^{208}Pb abundance more than ten times greater than that reached in the usual main component is produced by stars with $Z = 5 \times 10^{-4} \div 10^{-3}$.

Chapter 4

s–PROCESSING IN MASSIVE STARS

4.1 THE COMPUTATIONAL METHOD

In this section an outline is given of the procedure we followed in order to calculate the s–nucleosynthesis, starting from the evolutionary physical data previously obtained. During He–burning, the number densities of the various isotopes change as these nuclei get involved in (α , γ), (α , n), (n , γ), (n , p), (n , α) reactions and weak interactions.

The set of differential equations governing s–processing is given by:

$$\begin{aligned}\frac{dN_i}{dt} &= N_\alpha \sum_j (N_j < \sigma v >_{j\alpha} - N_i < \sigma v >_{i\alpha}) + \\ &+ N_n (N_j < \sigma v >_{jn} - N_i < \sigma v >_{in}) + \\ &+ \sum_j (\lambda_{ji} N_j - \lambda_{ij} N_i), \end{aligned} \tag{4.1}$$

where N_i is the number abundance of the element i and λ_{ji} the weak interaction rate that leads from nucleus j to nucleus i. In particular for the neutron density we have:

$$\frac{dN_n}{dt} = N_\alpha \sum_j N_j < \sigma v >_{\alpha j} - N_n \sum_l N_l < \sigma v >_{nl},$$

and assuming equilibrium between production and destruction ($dN_n/dt = 0$) because of the very short timescales on which the neutron–capture occurs (of the order of 10^{-6} s), N_n can be obtained as:

$$N_n = \frac{N_\alpha \sum_j N_j < \sigma v >_{\alpha j}}{\sum_l N_l < \sigma v >_{nl}} = \tau_n N_\alpha \sum_j N_j < \sigma v >_{\alpha j} . \tag{4.2}$$

We have defined here:

$$\tau_n \equiv \frac{1}{\sum_l N_l < \sigma v >_{nl}}$$

as the neutron mean lifetime; in the denominator all the neutron absorbers must be included. At each time step the neutron flux resulting from the (α , n) reactions is distributed over the seed nuclei proportionally to their n–capture cross sections and to the relative abundances (Busso and Gallino, 1985).

We know that the ^{22}Ne doesn't burn before the temperature reaches about 2.2×10^8 K. So only the last phase of the central He–burning needs to be considered as far as the s–element production is concerned. If we look at the temperature and density mass profiles during this phase we see that they don't change in an appreciable way, so we can tabulate them and use single T and ρ gradients for the whole calculation. We divided the core mass into meshes: at the maximum mass extension we have 60 meshes.

We also need the temporal evolution of the central convective core mass, and of the central temperature and density, that were obtained by an opportune fit of the evolutionary data.

4.2 NUCLEAR INPUTS

As far as the α-capture reactions are concerned, the nucleosynthesis code assignes to every mesh an average rate $\overline{\lambda_\alpha} = \overline{N_A < \sigma v >}$, which is calculated as:

$$\overline{\lambda}_\alpha(T,\rho) = \lambda_\alpha(\overline{T},\overline{\rho}).$$

The very fine grid of mass points assures us that this will be accurate enough.

The thermonuclear reaction rates were taken from CFHZ85 or CF88 accordingly to the set of data that was used in the evolutionary computation.

The s-processing phase in our model star involves central temperatures in the range $\sim$2.2–3.5 $\times 10^8$ K, and central densities in the range $\sim$1000–3000 g/cm^3. Over the wide field of physical parameters considered, the β-decay rates can change in an appreciable way, and the same is true for those neutron-capture cross sections that do not go as $1/v$ (see below).

We set up three different nuclear networks at the three reference temperatures T_{8c} = 2.5, 3.0, 3.5 K, including all the decay rates and the n-capture cross sections for the 271 isotopes involved, and inserting 41 branching points. Radioactive isotopes are included only if the producing reactions are fast enough, that is if the velocity of production is greater than 1% of the velocity of destruction. Table 4.1 shows the reaction network employed in the calculations.

4.2.1 Weak Interaction Rates

When temperatures are as high as hundreds of millions degrees several mechanisms can strongly modify the terrestrially measured beta decay rates (Kappeler, 1986; Takahashi and Yokoi, 1987).

Let us consider a thermal population of the atomic levels and call p_i the population probability of the state i. Then the total β-decay rate is the sum over all the possible states i of the parent nucleus of all the allowed transition rates to the daughter nucleus state j:

$$\lambda_\beta^{tot} = \sum_i (p_i \sum_j \lambda_{\beta ij}) \qquad (4.3)$$

The result is that the contribution of the excited states leads to larger decay rates, as happens for ^{79}Se, ^{87}Rb, ^{99}Tc, ^{107}Pd, ^{113}Cd, ^{115}In, ^{135}Cs.

Measurements of β decay rates from excited states are very difficult to perform because in most cases γ decay dominates over beta transition. This is not the case when we are considering the *isomeric states*, that is the long-lived excited states of some isotopes such as ^{79}Se, whose isomeric state at 96 KeV has a half-life of 3.9 m before γ-decaying to the ground state. At KT = 30 KeV this isomer is populated to $\sim$ 1%, and its decay represents the only significant term in equation 4.3.

Another important mechanism which plays a major role in affecting the β decay rates is the *bound state beta decay*. As a matter of fact, under the physical conditions

1	HE	4	2	C	12	3	O	16	4	NE	20	5	MG	24	6	SI	28	7	N	14											
8	O	18	9	NE	21	10	NE	22	11	MG	25	12	MG	26	13	SI	29	14	SI	30											
15	C	13	16	C	14	17	N	15	18	O	17	19	O	19	20	F	19	21	F	20											
22	NA	23	23	AL	27	24	P	31	25	S	32	26	S	33	27	S	34	28	S	36											
29	CL	35	30	CL	36	31	CL	37	32	AR	36	33	AR	38	34	AR	39	35	AR	40											
36	K	39	37	K	40	38	K	41	39	CA	40	40	CA	41	41	CA	42	42	CA	43											
43	CA	44	44	CA	46	45	CA	48	46	SC	45	47	TI	46	48	TI	47	49	TI	48											
50	TI	49	51	TI	50	52	V	51	53	CR	52	54	CR	53	55	CR	54	56	MN	55											
57	FE	54	58	FE	55	59	FE	56	60	FE	57	61	FE	58	62	CO	59	63	NI	58											
64	NI	59	65	NI	60	66	NI	61	67	NI	62	68	NI	63	69	NI	64	70	CU	63											
71	CU	65	72	ZN	64	73	ZN	66	74	ZN	67	75	ZN	68	76	ZN	70	77	GA	69											
78	GA	71	79	GE	70	80	GE	72	81	GE	73	82	GE	74	83	GE	76	84	AS	75											
85	SE	76	86	SE	77	87	SE	78	88	SE	79	89	SE	80	90	SE	82	91	BR	79											
92	BR	81	93	KR	80	94	KR	81	95	KR	82	96	KR	83	97	KR	84	98	KR	86											
99	RB	85	100	RB	87	101	SR	86	102	SR	87	103	SR	88	104	Y	89	105	ZR	90											
106	ZR	91	107	ZR	92	108	ZR	93	109	ZR	94	110	ZR	96	111	NB	93	112	MO	94											
113	MO	95	114	MO	96	115	MO	97	116	MO	98	117	MO100		118	TC	99	119	RU	98											
120	RU	99	121	RU100		122	RU101		123	RU102		124	RU104		125	RH103		126	PD104												
127	PD105		128	PD106		129	PD107		130	PD108		131	PD110		132	AG107		133	AG109												
134	CD108		135	CD109		136	CD110		137	CD111		138	CD112		139	CD113		140	CD114												
141	CD116		142	IN113		143	IN115		144	SN114		145	SN115		146	SN116		147	SN117												
148	SN118		149	SN119		150	SN120		151	SN122		152	SN124		153	SB121		154	SB123												
155	TE122		156	TE123		157	TE124		158	TE125		159	TE126		160	TE128		161	TE130												
162	I	127	163	XE128		164	XE129		165	XE130		166	XE131		167	XE132		168	XE134												
169	XE136		170	CS133		171	CS135		172	BA134		173	BA135		174	BA136		175	BA137												
176	BA138		177	LA139		178	CE140		179	CE142		180	PR141		181	ND142		182	ND143												
183	ND144		184	ND145		185	ND146		186	ND148		187	ND150		188	SM147		189	SM148												
190	SM149		191	SM150		192	SM151		193	SM152		194	SM154		195	EU151		196	EU153												
197	GD152		198	GD153		199	GD154		200	GD155		201	GD156		202	GD157		203	GD158												
204	GD160		205	TB159		206	DY160		207	DY161		208	DY162		209	DY164		210	HO163												
211	HO164		212	HO165		213	ER164		214	ER166		215	ER167		216	ER168		217	ER170												
218	TM169		219	YB170		220	YB171		221	YB172		222	YB173		223	YB174		224	YB176												
225	LU175		226	LU176		227	HF176		228	HF177		229	HF178		230	HF179		231	HF180												
232	TA179		233	TA180		234	TA181		235	W	180	236	W	182	237	W	183	238	W	184											
239	W	186	240	RE185		241	RE187		242	OS186		243	OS187		244	OS188		245	OS189												
246	OS190		247	OS192		248	IR191		249	IR193		250	PT192		251	PT193		252	PT194												
253	PT195		254	PT196		255	PT198		256	AU197		257	HG198		258	HG199		259	HG200												
260	HG201		261	HG202		262	HG204		263	TL203		264	TL205		265	PB204		266	PB205												
267	PB206		268	PB207		269	PB208		270	BI209		271	BI999																		

Table 4.1: The nuclear network that was used in our computations.

we are dealing with, the stellar matter is almost completely ionized. So a certain number of atomic orbits are free and can be occupated by electron emission. In these cases the binding energy must be added to the Q–value of the decay. As a consequence some isotopes such as ^{157}Gd, ^{160}Gd, ^{163}Dy, ^{179}Hf, ^{205}Tl, which are stable under terrestrial conditions, become unstable and lead to branching points along the s–process path.

To determine the weak interaction rates for the heavy elements, we started from the data by Takahashi and Yokoi (1983), who calculated beta decay rates for heavy nuclides ($26 \leq Z \leq 83$, $59 \leq A \leq 210$) for a range of stellar temperatures 1–5 $\times 10^8$ K and electron number densities 3–30 $\times 10^{26}$ cm^{-3} (that is matter densities of 1000–10000 g/cm^{-3}).

The β–decay processes they considered are:

- electron emission (β^- decay) into the continuum as well as into the bound state;
- positron emission (β^+ decay);
- capture of the orbital and free electrons.

Given the temperature and density mass gradients, each mass shell is characterized by a set of $\overline{T}, \overline{\rho}$ values. A program was written which interpolates among the Takahashi and Yokoi grid points in order to give the beta decay rates for every nucleus corresponding to the values of $\overline{T}$ and $\overline{\rho}$ of every shell. The resulting $\lambda_{\beta\pm}$ were then averaged in mass over the whole convective core and inserted into the network.

The β–decay rates for ^{79}Se was taken from Klay and Kappeler (1988), and the rates for the lighter nuclei ($Z < 26$) from Cosner and Truran (1981) and Fuller et al. (1982).

4.2.2 Neutron–Capture Cross Sections

We took the (n , γ), (n , p) and (n , α) reactions rates from the Bao and Kappeler compilation (1987). They give Maxwellian–averaged cross sections for the standard thermal energy of KT = 30 KeV as [1]:

$$< \sigma >= \frac{< \sigma v >}{v_T} = \frac{2}{\sqrt{\pi}} \frac{\int_0^\infty \sigma(E_n)\, E_n\, exp(-E_n/KT)\, dE_n}{\int_0^\infty E_n\, exp(-E_n/KT)\, dE_n},$$

where E_n is the total kinetic energy in the center–of–mass system, and $\sigma(E_n)$ is the differential cross section. The factor $2/\sqrt{\pi}$ comes out from having normalized to the thermal velocity $v_T = \sqrt{2KT/\mu}$ instead of the average velocity.

[1] We have seen in the previous chapter that the stellar neutron capture rate is rather insensitive to temperature.

The experimental neutron capture cross sections are determined with a precision of 4–5 % for favourable cases with smooth energy dependence. Resonant cross sections are more difficult to treat and usually exhibit systematic uncertainties of the order of 5–10 %. In few cases theoretical calculations are needed. This is so for those radioactive isotopes that are responsible for branchings along the s–process path, and in general when the experimental information is missing. The reliability of the calculated cross sections is at best 20–25 %.

A certain number of neutron capture cross sections were recently updated by Ratynski and Kappeler (1988a,b) and by Kappeler (1989) (see also Kappeler et al., 1989b), and these new data were included in our networks.

In the case of ^{64}Cu and ^{80}Br we took the analytical fit for the (n , γ) rate from Woosley et al. (1978), as well as for some (n , p) and (n , α) rates that are not taken into account in the Bao and Kappeler compilation.

A quite important point is that some nuclei have a non–standard behaviour, that is their neutron cross section doesn't follow the $1/v$ law (see paragraph 2.2). For: ^{24}Mg, ^{26}Mg, ^{28}Si, ^{30}Si, ^{54}Fe, ^{56}Fe, ^{57}Fe, ^{84}Kr, ^{93}Zr, ^{148}Sm, ^{150}Sm, and ^{208}Pb (Bao and Kappeler, 1987) and for ^{85}Rb and ^{87}Rb (Beer and Macklin, 1989) we scaled $\sigma(E_n)$ as $E_n^{-\beta}$, with β differing from 0.5, according to Bao and Kappeler and Beer and Macklin. Then we inserted in our nuclear networks the values obtained by averaging over the core meshes according to the neutron flux (that is by averaging over the neutron production rate).

Another point concerns those nuclei whose neutron–capture cross section depends on the temperature because of some low lying excited states that under stellar physical conditions are populated to a significant extent. They may be characterized by a different cross section than the ground state. Correction factors to the laboratory rates must then be applied when stellar quantities are needed, but they usually are lower than 5%. We checked their importance on the final yields of our computed process by adopting the *astrophysical factors* by Holmes et al. (1976) and Cosner and Truran (1981) for $A < 56$, but we found no sensitive variations in the $A < 90$ range.

4.3 THE CHEMICAL ABUNDANCES

As we said before, the aim of a s–process calculation, both in a classical analysis context than in a stellar evolution one, is to explain the solar abundance distribution of the s–isotopes, which is thus the direct empirical counterpart of the theoretical work. From here, if we assume the solar composition as typical of our Galaxy, we can derive materials to discuss its chemical evolution.

Solar–system abundances can be obtained from different sources; in particular from:

- *meteorites*, under the hypothesis that their composition corresponds to the solar–nebula one. This is the main source of information on solar–system abundances, which can now be estimated with a precision of 5–10 % for most elements;

- *solar spectrum*, if it is true that the Sun has not experienced mixing processes that can bring to the surface products of the internal nuclear activity, modifying the original composition of the envelope. The abundances obtained in this way are known with larger uncertainties in comparison to the previous case: they are of the order of 15–25 %. Moreover, the observation of the Sun can only give us elemental abundances, and not the isotopic information we need for the s–process study.

We shall present most of our results in terms of "*overabundances*" that we define as the ratio between the stellar and the initial abundances (ZAMS abundances) of a given isotope. The recent compilation of solar abundances by Anders and Grevesse (1989) was used (see tables 4.2 and 4.3).

As far as the initial composition is concerned, let us remind that we started our calculation from an advanced stage of He–burning, when the central temperature was T$\sim 2.2 \times 10^8$ K. At this stage, we took from the evolutionary calculation the abundances of the main isotopes, which have already suffered some He–burning. ^{17}O and ^{15}N were given CNO–equilibrium abundances, while ^{22}Ne was set as the sum of the CNO initial abundances [2]. To all the other isotopes, that are supposed not to have been processed in any way in the preceding evolution, solar–system abundances were assigned.

[2]Remember that during the H–burning all the CNO initial content is converted into ^{14}N, which at helium ignition is burnt to give ^{18}O and later ^{22}Ne through the reaction chain: $^{14}N(\alpha,\gamma)^{18}F(\beta^+)^{18}O(\alpha,\gamma)^{22}Ne$.

Element	This Work*	Anders & Ebihara (1982)*	σ (%)	N†	Mean CI Chondr.‡		Orgueil§		N
1 H	2.79×10^{10}	2.72×10^{10}		–			2.02	%	2
2 He	2.72×10^{9}	2.18×10^{9}		–			56	nL/g	
3 Li	57.1	59.7	9.2	4	1.50	ppm	1.49	ppm	3
4 Be	0.73	0.78	9.5	(8)	24.9	ppb	24.9	ppb	0
5 B	21.2	24	10	1	870	ppb	870	ppb	1
6 C	1.01×10^{7}	1.21×10^{7}		–			3.45	%	7
7 N	3.13×10^{6}	2.48×10^{6}		–			3180	ppm	4
8 O	2.38×10^{7}	2.01×10^{7}	10	–			46.4	%	4
9 F	843	843	15	7	60.7	ppm	58.2	ppm	5
10 Ne	3.44×10^{6}	3.76×10^{6}	14	–			203	pL/g	
11 Na	5.74×10^{4}	5.70×10^{4}	7.1	20	5000	ppm	4900	ppm	14
12 Mg	1.074×10^{6}	1.075×10^{6}	3.8	15	9.89	%	9.53	%	11
13 Al	8.49×10^{4}	8.49×10^{4}	3.6	19	8680	ppm	8690	ppm	13
14 Si	1.00×10^{6}	1.00×10^{6}	4.4	9	10.64	%	10.67	%	4
15 P	1.04×10^{4}	1.04×10^{4}	10	4	1220	ppm	1180	ppm	3
16 S	5.15×10^{5}	5.15×10^{5}	13	5	6.25	%	5.25	%	2
17 Cl	5240	5240	15	10	704	ppm	698	ppm	8
18 Ar	1.01×10^{5}	1.04×10^{5}	6	–			751	pL/g	7
19 K	3770	3770	7.7	29	558	ppm	566	ppm	20
20 Ca	6.11×10^{4}	6.11×10^{4}	7.1	15	9280	ppm	9020	ppm	12
21 Sc	34.2	33.8	8.6	18	5.82	ppm	5.83	ppm	12
22 Ti	2400	2400	5.0	7	436	ppm	436	ppm	7
23 V	293	295	5.1	9	56.5	ppm	56.2	ppm	7
24 Cr	1.35×10^{4}	1.34×10^{4}	7.6	13	2660	ppm	2660	ppm	9
25 Mn	9550	9510	9.6	20	1990	ppm	1980	ppm	12
26 Fe	9.00×10^{5}	9.00×10^{5}	2.7	19	19.04	%	18.51	%	14
27 Co	2250	2250	6.6	18	502	ppm	507	ppm	12
28 Ni	4.93×10^{4}	4.93×10^{4}	5.1	27	1.10	%	1.10	%	21
29 Cu	522	514	11	8	126	ppm	119	ppm	5
30 Zn	1260	1260	4.4	27	312	ppm	311	ppm	17
31 Ga	37.8	37.8	6.9	14	10.0	ppm	10.1	ppm	10
32 Ge	119	118	9.6	31	32.7	ppm	32.6	ppm	23
33 As	6.56	6.79	12	18	1.86	ppm	1.85	ppm	13
34 Se	62.1	62.1	6.4	18	18.6	ppm	18.2	ppm	11
35 Br	11.8	11.8	19	(18)	3.57	ppm	3.56	ppm	10
36 Kr	45	45.3	18	–			8.7	pL/g	7
37 Rb	7.09	7.09	6.6	19	2.30	ppm	2.30	ppm	13
38 Sr	23.5	23.8	8.1	18	7.80	ppm	7.80	ppm	15
39 Y	4.64	4.64	6.0	5	1.56	ppm	1.53	ppm	4
40 Zr	11.4	10.7	6.4	5	3.94	ppm	3.95	ppm	5
41 Nb	0.698	0.71	1.4	2	246	ppb	246	ppb	2
42 Mo	2.55	2.52	5.5	2	928	ppb	928	ppb	2
44 Ru	1.86	1.86	5.4	9	712	ppb	714	ppb	5
45 Rh	0.344	0.344	8	(7)	134	ppb	134	ppb	0
46 Pd	1.39	1.39	6.6	25	560	ppb	556	ppb	17
47 Ag	0.486	0.529	2.9	6	199	ppb	197	ppb	5
48 Cd	1.61	1.69	6.5	30	686	ppb	680	ppb	21
49 In	0.184	0.184	6.4	24	80	ppb	77.8	ppb	16
50 Sn	3.82	3.82	9.4	11	1720	ppb	1680	ppb	9
51 Sb	0.309	0.352	18	22	142	ppb	133	ppb	15
52 Te	4.81	4.91	10	17	2320	ppb	2270	ppb	12
53 I	0.90	0.90	21	(11)	433	ppb	433	ppb	0
54 Xe	4.7	4.35	20	–			8.6	pL/g	6
55 Cs	0.372	0.372	5.6	20	187	ppb	186	ppb	11
56 Ba	4.49	4.36	6.3	8	2340	ppb	2340	ppb	8
57 La	0.4460	0.448	2.0	4	234.7	ppb	236	ppb	9
58 Ce	1.136	1.16	1.7	4	603.2	ppb	619	ppb	8
59 Pr	0.1669	0.174	2.4	(20)	89.1	ppb	90	ppb	2
60 Nd	0.8279	0.836	1.3	4	452.4	ppb	463	ppb	11
62 Sm	0.2582	0.261	1.3	4	147.1	ppb	144	ppb	10
63 Eu	0.0973	0.0972	1.0	4	56.0	ppb	54.7	ppb	17
64 Gd	0.3300	0.331	1.4	4	196.6	ppb	199	ppb	7
65 Tb	0.0603	0.0589	2.2	(21)	36.3	ppb	35.3	ppb	4
66 Dy	0.3942	0.398	1.4	4	242.7	ppb	246	ppb	6
67 Ho	0.0889	0.0875	2.4	(23)	55.6	ppb	55.2	ppb	3
68 Er	0.2508	0.253	1.3	4	158.9	ppb	162	ppb	6
69 Tm	0.0378	0.0386	2.3	(20)	24.2	ppb	22	ppb	1
70 Yb	0.2479	0.243	1.6	4	162.5	ppb	166	ppb	12
71 Lu	0.0367	0.0369	1.3	4	24.3	ppb	24.5	ppb	12
72 Hf	0.154	0.176	(1.9)	(3)	104	ppb	108	ppb	3
73 Ta	0.0207	0.0226	1.8	2	14.2	ppb	14.0	ppb	1
74 W	0.133	0.137	5.1	3	92.6	ppb	92.3	ppb	3
75 Re	0.0517	0.0507	9.4	21	36.5	ppb	37.1	ppb	15
76 Os	0.675	0.717	6.3	16	486	ppb	483	ppb	12
77 Ir	0.661	0.660	6.1	36	481	ppb	474	ppb	27
78 Pt	1.34	1.37	7.4	10	990	ppb	973	ppb	9
79 Au	0.187	0.186	15	41	140	ppb	145	ppb	27
80 Hg	0.34	0.52	12	–	258	ppb	258	ppb	0
81 Tl	0.184	0.184	9.4	18	142	ppb	143	ppb	12
82 Pb	3.15	3.15	7.8	3	2470	ppb	2430	ppb	1
83 Bi	0.144	0.144	8.2	13	114	ppb	111	ppb	7
90 Th	0.0335	0.0335	5.7	9	29.4	ppb	28.6	ppb	1
92 U	0.0090	0.0090	8.4	16	8.1	ppb	8.1	ppb	7

*Abundances of Mg, S, and Fe are based on average of mean values for individual meteorites. For the remaining elements, a straight average of all acceptable analyses was used.

†Dashes indicate solar or interpolated abundances, parentheses mean that the abundance is based at least in part on meteorites of other classes. See Sec. 3.6 for explanation of the REE values.

‡The CI chondritic mean (for Si = 10.64%) is calculated from the atomic abundances in column 2, using the relation $C = 3.785 \times 10^{-3} HA$, where C = weight concentration (ppm), H = atomic abundance, and A = atomic weight. However, these values have not been renormalized to 100%.

§Abundances of HCNO in Orgueil are from sources given in Anders & Ebihara (1982). Abundances of noble gases (in nL/g or pL/g at STP) are not for the elements but for the principal isotopes He^4, Ne^{20}, Ar^{36}, Kr^{84}, and Xe^{132} (J2, Mazor et al., 1970). As He and Ne in bulk Orgueil are derived mainly from the solar wind, the indigenous values for these two are based on ratios for NaOH-etched Orgueil silicates: $Ne^{20}/Ar^{36} = 0.27$ and $He^4/Ne^{20} = 277$ (J2).

Table 4.2: Solar-system abundances of the elements, based on meteorites (atoms/10^6 Si) (Anders and Grevesse, 1989).

Element, A	Atom Percent	Process*	Abund.†
1 H 1	99.9966		2.79×10^{10}
2	0.0034	U	9.49×10^{5}
2 He 3	0.0142	U,h?	3.86×10^{5}
4	99.9858	U,h	2.72×10^{9}
3 Li 6	7.5	X	4.28
7	92.5	U,x,h	52.82
4 Be 9	100	X	0.73
5 B 10	19.9	X	4.22
11	80.1	X	16.98
6 C 12	98.90	He	9.99×10^{5}
13	1.10	H,N	1.11×10^{5}
7 N 14	99.634	H	3.12×10^{6}
15	0.366	H,N	1.15×10^{6}
8 O 16	99.762	He	2.37×10^{7}
17	0.038	N,H	9.04×10^{5}
18	0.200	He,N	4.76×10^{6}
9 F 19	100	N	843
10 Ne 20	92.99	C	3.20×10^{6}
21	0.226	C,Ex	7.77×10^{3}
22	6.79	He,N	2.34×10^{5}
11 Na 23	100	C/NeEx	5.74×10^{4}
12 Mg 24	78.99	N,Ex	8.48×10^{5}
25	10.00	Ne,Ex,C	1.07×10^{5}
26	11.01	Ne,Ex,C	1.18×10^{5}
13 Al 27	100	Ne,Ex	8.49×10^{4}
14 Si 28	92.23	O,Ex	9.22×10^{5}
29	4.67	Ne,Ex	4.67×10^{4}
30	3.10	Ne,Ex	3.10×10^{4}
15 P 31	100	Ne,Ex	1.04×10^{4}
16 S 32	95.02	O,Ex	4.89×10^{5}
33	0.75	Ex	3.86×10^{3}
34	4.21	O,Ex	2.17×10^{4}
36	0.02	Ex,Ne,S	1.03×10^{2}
17 Cl 35	75.77	Ex	2860
37	24.23	Ex,C,S	913
18 Ar 36	84.2	Ex	8.50×10^{4}
38	15.8	O,Ex	1.60×10^{4}
40		S,Ne	26
40			*25±14*
19 K 39	93.2581	Ex	3516
40	0.01167	S,Ex,Ne	0.440
40			*5.48*
41	6.7302	Ex	253.7
20 Ca 40	96.941	Ex	5.92×10^{4}
42	0.647	Ex,O	395
43	0.135	Ex,C,S	82.5
44	2.086	Ex,S	1275
46	0.004	Ex,Ne	2.4
48	0.187	E,Ex	114
21 Sc 45	100	Ex,Ne,E	34.2
22 Ti 46	8.0	Ex	192
47	7.3	Ex	175
48	73.8	Ex	1771
49	5.5	Ex	132
50	5.4	E	130
23 V 50	0.250	Ex,E	0.732
51	99.750	Ex	292
24 Cr 50	4.345	Ex	587
52	83.789	Ex	1.131×10^{4}
53	9.501	Ex	1283
54	2.365	E	319
25 Mn 55	100	Ex,E	9550
26 Fe 54	5.8	Ex	5.22×10^{4}
56	91.72	Ex,E	8.25×10^{5}
57	2.2	E,Ex	1.96×10^{4}
58	0.28	He,E,C	2.52×10^{3}
27 Co 59	100	E,C	2250
28 Ni 58	68.27	E,Ex	3.37×10^{4}
60	26.10	E	1.29×10^{4}
61	1.13	E,Ex,C	557
62	3.59	E,Ex,O	1770
64	0.91	Ex	449
29 Cu 63	69.17	Ex,C	361
65	30.83	Ex	161

Element, A	Atom Percent	Process*	Abund.†
30 Zn 64	48.63	Ex,E	613
66	27.90	E	352
67	4.10	E,S	51.7
68	18.75	E,S	236
70	0.62	E,S	7.8
31 Ga 69	60.108	S,e,r	22.7
71	39.892	S,e,r	15.1
32 Ge 70	20.5	S,e	24.4
72	27.4	S,e,r	32.6
73	7.8	e,r	9.28
74	36.5	e,r	43.4
76	7.8	E	9.28
33 As 75	100	R,s	6.56
34 Se 74	0.88	P	0.55
76	9.0	S,p	5.6
77	7.6	R,s	4.7
78	23.6	R,s	14.7
80	49.7	R,s	30.9
82	9.2	R	5.7
35 Br 79	50.69	R,s	5.98
81	49.31	R,s	5.82
36 Kr 78	0.339	P	0.153
80	2.22	S,p	0.999
82	11.45	S	5.15
83	11.47	R,s	5.16
84	57.11	R,S	25.70
86	17.42	S,r	7.84
37 Rb 85	72.165	R,s	5.12
87	27.835	S	1.97
87			*2.11*
38 Sr 84	0.56	P	0.132
86	9.86	S	2.32
87	7.00	S	*1.64*
87			*1.51*
88	82.58	S,r	19.41
39 Y 89	100	S	4.64
40 Zr 90	51.45	S	5.87
91	11.22	S	1.28
92	17.15	S	1.96
94	17.38	S	1.98
96	2.80	R	0.320
41 Nb 93	100	S	0.698
42 Mo 92	14.84	P	0.378
94	9.25	P	0.236
95	15.92	R,s	0.406
96	16.68	S	0.425
97	9.55	R,s	0.244
98	24.13	R,s	0.615
100	9.63	R	0.246
44 Ru 96	5.52	P	0.103
98	1.88	P	0.0350
99	12.7	R,s	0.236
100	12.6	S	0.234
101	17.0	R,s	0.316
102	31.6	R,S	0.588
104	18.7	R	0.348
45 Rh 103	100	R,s	0.344
46 Pd 102	1.020	P	0.0142
104	11.14	S	0.155
105	22.33	R,s	0.310
106	27.33	R,S	0.380
108	26.46	R,S	0.368
110	11.72	R	0.163
47 Ag 107	51.839	R,s	0.252
109	48.161	R,s	0.234
48 Cd 106	1.25	P	0.0201
108	0.89	P	0.0143
110	12.49	S	0.201
111	12.80	R,S	0.206
112	24.13	S,R	0.388
113	12.22	R,S	0.197
114	28.73	S,R	0.463
116	7.49	R	0.121
49 In 113	4.3	p,s,r	0.0079
115	95.7	R,S	0.176
50 Sn 112	0.973	P	0.0372
114	0.659	P,s	0.0252
115	0.339	p,s,r	0.0129
116	14.538	S,r	0.555
117	7.672	R,S	0.293
118	24.217	S,r	0.925
119	8.587	S,R	0.328
120	32.596	S,R	1.245
122	4.632	R	0.177
124	5.787	R	0.221

Element, A	Atom Percent	Process*	Abund.†
51 Sb 121	57.362	R,s	0.177
123	42.638	R	0.132
52 Te 120	0.09	P	0.0043
122	2.57	S	0.124
123	0.89	S	0.0428
124	4.76	S	0.229
125	7.10	R,s	0.342
126	18.89	R,S	0.909
128	31.73	R	1.526
130	33.97	R	1.634
53 I 127	100	R	0.90
54 Xe 124	0.121	P	0.00571
126	0.108	P	0.00509
128	2.19	S	0.103
129	27.34	R	1.28
130	4.35	S	0.205
131	21.69	R	1.02
132	26.50	R,s	1.24
134	9.76	R	0.459
136	7.94	R	0.373
55 Cs 133	100	R,s	0.372
56 Ba 130	0.106	P	0.00476
132	0.101	P	0.00453
134	2.417	S	0.109
135	6.592	R,s	0.296
136	7.854	S	0.353
137	11.23	S,r	0.504
138	71.70	S	3.22
57 La 138	0.089	P	0.000397
138			*0.000409*
139	99.911	S,r	0.446
58 Ce 136	0.19	P	0.00216
138	0.25	P	0.00284
138			*0.00283*
140	88.48	S,r	1.005
142	11.08	R	0.126
59 Pr 141	100	R,S	0.167
60 Nd 142	27.13	S	0.225
143	12.18	R,S	0.101
143			*0.100*
144	23.80	S,R	0.197
145	8.30	R,s	0.0687
146	17.19	R,S	0.142
148	5.76	R	0.0477
150	5.64	R	0.0467
62 Sm 144	3.1	P	0.00800
147	15.0	R,s	0.0387
147			*0.0399*
148	11.3	S	0.0292
149	13.8	R,S	0.0156
150	7.4	S	0.0191
152	26.7	R,S	0.0689
154	22.7	R	0.0586
63 Eu 151	47.8	R,s	0.0465
153	52.2	R,s	0.0508
64 Gd 152	0.20	P,s	0.00066
154	2.18	S	0.00719
155	14.80	R,s	0.0488
156	20.47	R,s	0.0676
157	15.65	R,s	0.0516
158	24.84	R,s	0.0820
160	21.86	R	0.0721
65 Tb 159	100	R	0.0603
66 Dy 156	0.056	P	0.000221
158	0.096	P	0.000378
160	2.34	S	0.00922
161	18.91	R	0.0745
162	25.51	R,s	0.101
163	24.90	R	0.0982
164	28.19	R,S	0.111
67 Ho 165	100	R	0.0889
68 Er 162	0.14	P	0.000351
164	1.61	P,S	0.00404
166	33.6	R,s	0.0843
167	22.95	R	0.0576
168	26.8	R,S	0.0672
170	14.9	R	0.0374
69 Tm 169	100	R,s	0.0378
70 Yb 168	0.13	P	0.000322
170	3.05	S	0.00756
171	14.3	R,s	0.0354
172	21.9	R,S	0.0543
173	16.12	R,s	0.0400
174	31.8	S,R	0.0788
176	12.7	R	0.0315

Element, A	Atom Percent	Process*	Abund.†
71 Lu 175	97.41	R,s	0.0357
176	2.59	S	0.000951
176			*0.001035*
72 Hf 174	0.162	P	0.000249
176	5.206	S	0.00802
176			*0.00793*
177	18.606	R,s	0.0287
178	27.297	R,S	0.0420
179	13.629	R,s	0.0210
180	35.100	S,R	0.0541
73 Ta 180	0.012	p,s,r	2.48×10^{-6}
181	99.988	R,S	0.0207
74 W 180	0.13	P	0.000173
182	26.3	R,s	0.0350
183	14.3	R,s	0.0190
184	30.67	R,s	0.0408
186	28.6	R	0.0380
75 Re 185	37.40	R,s	0.0193
187	62.60	R	0.0324
187			*0.0351*
76 Os 184	0.018	P	0.000122
186	1.58	S	0.0107
187	1.6	S	0.0108
187			*0.00807*
188	13.3	R,s	0.0898
189	16.1	R	0.109
190	26.4	R	0.178
192	41.0	R	0.277
77 Ir 191	37.3	R	0.247
193	62.7	R	0.414
78 Pt 190	0.0127	P	0.000170
192	0.78	S	0.0105
194	32.9	R	0.441
195	33.8	R	0.453
196	25.2	R	0.338
198	7.19	R	0.0963
79 Au 197	100	R	0.187
80 Hg 196	0.1534	P	0.00052
198	9.968	S	0.0239
199	16.873	R,S	0.0574
200	23.096	S,r	0.0785
201	13.181	S,r	0.0448
202	29.863	S,r	0.1015
204	6.865	R	0.0233
81 Tl 203	29.524	R,S	0.0543
205	70.476	S,R	0.1297
82 Pb 204	1.94	S	0.0611
206	19.12	R,S	0.602
206			*0.593*
207	20.62	R,S	0.650
207			*0.644*
208	58.31	R,s	1.837
208			*1.828*
83 Bi 209	100	R,s	0.144
90 Th 232	100	RA	0.0335
232			*0.0420*
92 U 235	0.7200	RA	6.48×10^{-5}
235			*0.00573*
238	99.2745	RA	0.00693
238			*0.0181*

*Assignments to nucleosynthetic processes are from Cameron (1982), Schramm (private communication, 1982), Wallner et al. (1986), Woosley and Hoffman (1986, 1989), and Beer and Penzhorn (1987). Processes are listed in the order of importance, with minor processes (10-30% for r- and s-processes) shown in lower case. See above references for details.

U = cosmological nucleosynthesis
H = hydrogen burning
N = hot or explosive hydrogen burning
He = helium burning
C = carbon burning
O = oxygen burning
Ne = neon burning
Ex = explosive nucleosynthesis
E = nuclear statistical equilibrium
S = s-process
R = r-process
RA = r-process producing actinides
P = p-process
X = cosmic-ray spallation

†Italicized values refer to abundances 4.55×10^{9} yr ago.

Table 4.3: Abundance of the nuclides (atoms/10^6 Si) (Anders and Grevesse, 1989).

	CFHZ85	CF88
$\overline{N_n^{max}}(\times 10^5\ \mathrm{cm}^{-3})$	7.027	5.402
$N_n^{peak}(\times 10^7\ \mathrm{cm}^{-3})$	1.866	1.524
$\tau\ (\mathrm{mb}^{-1})$	0.224	0.239
n_c	6.645	7.301

Table 4.4: The final values of some characteristic parameters in our s–process calculations. The two cases CFHZ85 (above) and CF88 (below) with different thermonuclear reaction rates are considered.

4.4 RESULTS

4.4.1 The Overabundances Plot

Table 4.4 shows the final values (at helium central exhaustion) of the mean neutron density maximum, the peak central density, the total neutron exposure and the number of neutrons captured per iron seed nucleus. In our computations n_c is calculated as the ratio between the total number of neutrons captured by all the seeds starting from ^{51}V and the initial ^{56}Fe abundance.

Table 4.5 gives the final overabundances for our networks isotopes, and figure 4.1 is a plot of the overabundances as a function of the atomic mass. The dark stars refer to s–only nuclei, while the crosses to nuclei with overabundances greater than 0.1.

The following main features can be recognized:

- In the range $A \leq 70$ the most overabundant nucleus is ^{40}K, while ^{26}Mg, ^{64}Ni, ^{65}Cu, ^{66}Zn, ^{67}Zn, ^{68}Zn, ^{69}Ga and ^{71}Ga have overproduction factors over 100. There are also other isotopes which are efficiently produced, such as ^{22}Ne, ^{25}Mg, ^{36}S, ^{58}Fe, ^{61}Ni, ^{63}Cu, whose overabundances are over 70.

- In the range $70 \leq A \leq 90$ ^{80}Kr is by far the dominant nucleus, followed by ^{70}Ge, ^{76}Se, ^{82}Kr, ^{86}Sr, ^{87}Sr. These are all s–only isotopes, with overabundances greater than 100. After ^{87}Sr, the overproduction factors are decreasing: for ^{88}Sr, ^{89}Y, ^{90}Zr, ^{91}Zr, and ^{92}Zr they range in between 10 and 100.

- When $A \geq 90$ the curve goes down to overproduction factors that average about 4–5 in the case of the s–only isotopes. There are two exceptions: ^{152}Gd and ^{180}Ta that have overabundances of 44 and 264 respectively in the CFHZ85 case, and 48 and 295 in the CF88 case.

The fall of the plot beyond $A = 90$ is a well known feature: it is due to the poisoning action of the light elements, first of all the ^{22}Ne daughter nucleus ^{25}Mg, which

6.64

HE 4	9.27179D-08	*	C 12	8.72218D+01	*	O 16	8.44365D+01	*	NE 20	2.24226D+00	*	MG 24	8.28443D-01
SI 28	6.85351D-01	*	N 14	0.00000D+00	*	O 18	0.00000D+00	*	NE 21	4.78790D+00	*	NE 22	8.90294D+01
MG 25	8.63952D+01	*	MG 26	1.14676D+02	*	SI 29	3.34300D+00	*	SI 30	7.39341D+00	*	C 13	0.00000D+00
C 14	0.00000D+00	*	N 15	1.05237D-01	*	O 17	4.80262D+00	*	O 19	0.00000D+00	*	F 19	3.00082D-01
F 20	2.93501D+23	*	NA 23	6.55377D+00	*	AL 27	1.14945D+00	*	P 31	3.11986D+01	*	S 32	4.37529D-01
S 33	1.08877D+00	*	S 34	8.63043D-01	*	S 36	9.04604D+01	*	CL 35	1.92844D+00	*	CL 36	2.16719D+23
CL 37	6.71349D+01	*	AR 36	1.70320D-01	*	AR 38	3.46199D+00	*	AR 39	3.66172D+22	*	AR 40	5.41076D+01
K 39	2.81612D+00	*	K 40	3.10245D+02	*	K 41	5.93601D+00	*	CA 40	2.24578D-01	*	CA 41	2.82318D+23
CA 42	5.28508D+00	*	CA 43	7.40223D+00	*	CA 44	1.99061D+00	*	CA 46	3.06847D-01	*	CA 48	8.21902D-01
SC 45	6.98183D+00	*	TI 46	3.64353D+00	*	TI 47	1.53964D+00	*	TI 48	2.76724D-01	*	TI 49	4.52801D+00
TI 50	1.64734D+01	*	V 51	6.63873D-01	*	CR 52	1.65497D-01	*	CR 53	2.75236D-01	*	CR 54	1.58061D+01
MN 55	1.06981D-01	*	FE 54	5.93295D-04	*	FE 55	1.14746D+19	*	FE 56	9.92019D-02	*	FE 57	1.64949D+00
FE 58	7.41833D+01	*	CO 59	3.29751D+01	*	NI 58	2.17450D-04	*	NI 59	3.99567D+21	*	NI 60	7.94902D+00
NI 61	8.27549D+01	*	NI 62	5.11677D+01	*	NI 63	4.83898D+21	*	NI 64	1.90896D+02	*	CU 63	9.60330D+01
CU 65	2.60747D+02	*	ZN 64	4.43411D+01	*	ZN 66	1.44088D+02	*	ZN 67	2.11108D+02	*	ZN 68	2.16795D+02
ZN 70	1.07597D-01	*	GA 69	2.70091D+02	*	GA 71	3.57899D+02	*	GE 70	3.47903D+02	*	GE 72	2.75827D+02
GE 73	1.87824D+02	*	GE 74	1.47991D+02	*	GE 76	2.82242D-02	*	AS 75	9.04911D+01	*	SE 76	3.26688D+02
SE 77	1.37150D+02	*	SE 78	1.72201D+02	*	SE 79	5.01868D+19	*	SE 80	4.34722D+00	*	SE 82	1.44530D-02
BR 79	5.88222D+01	*	BR 81	6.11131D+00	*	KR 80	7.69323D+02	*	KR 81	5.62816D+23	*	KR 82	3.55237D+02
KR 83	1.03379D+02	*	KR 84	8.14964D+01	*	KR 86	4.10001D-01	*	RB 85	5.20056D+01	*	RB 87	3.61132D-01
SR 86	2.79981D+02	*	SR 87	2.48071D+02	*	SR 88	5.79898D+01	*	Y 89	3.84404D+01	*	ZR 90	1.29189D+01
ZR 91	1.58139D+01	*	ZR 92	1.23926D+01	*	ZR 93	1.57202D+22	*	ZR 94	8.26216D+00	*	ZR 96	8.80312D-02
NB 93	1.23157D-02	*	MO 94	3.88162D-02	*	MO 95	3.47280D+00	*	MO 96	7.66009D+00	*	MO 97	4.23310D+00
MO 98	5.02665D+00	*	MO100	2.45977D-10	*	TC 99	2.40125D+17	*	RU 98	2.38943D-22	*	RU 99	1.38642D+00
RU100	5.85995D+00	*	RU101	8.84330D-01	*	RU102	2.36659D+00	*	RU104	2.21715D-16	*	RH103	8.70922D-01
PD104	5.42424D+00	*	PD105	6.46227D-01	*	PD106	2.37754D+00	*	PD107	3.95092D+20	*	PD108	2.75150D+00
PD110	6.46035D-15	*	AG107	9.39037D-02	*	AG109	1.14065D+00	*	CD108	1.07706D+00	*	CD109	9.42577D+15
CD110	3.88894D+00	*	CD111	9.92200D-01	*	CD112	2.14433D+00	*	CD113	1.25168D+00	*	CD114	2.41088D+00
CD116	7.54195D-10	*	IN113	3.41492D-01	*	IN115	1.25938D+00	*	SN114	9.24556D-02	*	SN115	7.44112D-02
SN116	2.88559D+00	*	SN117	1.21794D+00	*	SN118	2.13676D+00	*	SN119	1.48160D+00	*	SN120	2.08371D+00
SN122	5.92015D-03	*	SN124	5.92015D-03	*	SB121	8.58617D-01	*	SB123	4.37856D-04	*	TE122	2.81423D+00
TE123	2.76493D+00	*	TE124	2.64391D+00	*	TE125	6.35856D-01	*	TE126	1.08796D+00	*	TE128	1.51370D-02
TE130	3.15545D-02	*	I 127	1.56371D-01	*	XE128	3.28825D+00	*	XE129	1.32643D-01	*	XE130	2.64523D+00
XE131	2.34365D-01	*	XE132	1.16316D+00	*	XE134	2.26745D-03	*	XE136	8.51741D-01	*	CS133	4.29479D-01
CS135	3.25873D+17	*	BA134	3.45302D+00	*	BA135	6.16236D-01	*	BA136	3.52979D+00	*	BA137	3.14001D+00
BA138	4.97605D+00	*	LA139	3.55187D+00	*	CE140	4.03459D+00	*	CE142	1.76670D-02	*	PR141	2.08028D+00
ND142	3.57252D+00	*	ND143	1.43171D+00	*	ND144	1.58682D+00	*	ND145	1.01551D+00	*	ND146	1.46609D+00
ND148	2.06685D-19	*	ND150	1.43693D-20	*	SM147	8.06090D-01	*	SM148	4.02871D+00	*	SM149	6.00712D-01
SM150	3.62547D+00	*	SM151	2.02738D+16	*	SM152	8.50557D-02	*	SM154	9.57670D-26	*	EU151	1.83642D-01
EU153	2.37730D-01	*	GD152	4.37512D+01	*	GD153	2.16998D+16	*	GD154	4.84223D+00	*	GD155	2.30295D-01
GD156	6.24512D-01	*	GD157	4.29629D-01	*	GD158	1.62972D+00	*	GD160	4.59434D-16	*	TB159	2.57173D-01
DY160	4.07604D+00	*	DY161	2.06320D-01	*	DY162	5.20586D-01	*	DY164	2.66368D-01	*	HO163	1.11973D-01
HO164	2.47437D+15	*	HO165	2.28511D-01	*	ER164	6.56272D+00	*	ER166	4.75943D-01	*	ER167	3.00800D-01
ER168	9.74779D-01	*	ER170	7.06220D-25	*	TM169	5.52582D-01	*	YB170	4.77115D+00	*	YB171	5.31262D-01
YB172	1.04830D+00	*	YB173	7.48977D-01	*	YB174	1.58497D+00	*	YB176	7.52384D-01	*	LU175	5.74172D-01
LU176	3.85288D-04	*	HF176	6.04059D+00	*	HF177	6.13977D-01	*	HF178	1.62836D+00	*	HF179	9.79142D-01
HF180	2.03645D+00	*	TA179	9.89586D+18	*	TA180	2.64052D+02	*	TA181	1.36892D+00	*	W 180	1.42052D-23
W 182	2.04583D+00	*	W 183	2.24120D+00	*	W 184	1.98968D+00	*	W 186	9.65683D-02	*	RE185	6.42958D-01
RE187	1.08290D-03	*	OS186	4.36443D+00	*	OS187	2.45345D+00	*	OS188	5.53543D-01	*	OS189	1.54644D-01
OS190	3.64341D-01	*	OS192	7.15823D-03	*	IR191	5.72236D-02	*	IR193	9.83581D-03	*	PT192	4.40506D+00
PT193	3.87367D+19	*	PT194	1.30346D-01	*	PT195	3.58477D-02	*	PT196	2.88615D-01	*	PT198	7.78554D-07
AU197	1.56847D-01	*	HG198	2.80686D+00	*	HG199	7.54199D-01	*	HG200	1.71264D+00	*	HG201	1.45445D+00
HG202	1.93610D+00	*	HG204	8.50984D-05	*	TL203	2.13108D+00	*	TL205	1.83340D-02	*	PB204	2.64540D+00
PB205	1.66738D+21	*	PB206	2.94533D+00	*	PB207	3.86674D+00	*	PB208	2.96662D+00	*	BI209	3.17550D-01
BI999	0.00000D+00	*											

7.30

HE 4	1.79212D-08	*	C 12	1.39156D+02	*	O 16	5.84352D+01	*	NE 20	2.66458D+00	*	MG 24	8.46713D-01
SI 28	6.72029D-01	*	N 14	0.00000D+00	*	O 18	0.00000D+00	*	NE 21	4.79176D+00	*	NE 22	7.78390D+01
MG 25	9.31970D+01	*	MG 26	1.30537D+02	*	SI 29	3.31488D+00	*	SI 30	7.37632D+00	*	C 13	0.00000D+00
C 14	0.00000D+00	*	N 15	1.05237D-01	*	O 17	3.10670D+00	*	O 19	0.00000D+00	*	F 19	2.76887D-01
F 20	3.03228D+23	*	NA 23	6.60643D+00	*	AL 27	1.24951D+00	*	P 31	3.37265D+01	*	S 32	4.25578D-01
S 33	1.05773D+00	*	S 34	8.46699D-01	*	S 36	9.72963D+01	*	CL 35	1.92113D+00	*	CL 36	2.14934D+23
CL 37	6.79892D+01	*	AR 36	1.51627D-01	*	AR 38	3.52507D+00	*	AR 39	2.75136D+22	*	AR 40	5.83930D+01
K 39	2.92811D+00	*	K 40	3.25409D+02	*	K 41	6.24235D+00	*	CA 40	2.03244D-01	*	CA 41	2.55484D+23
CA 42	5.47451D+00	*	CA 43	7.67068D+00	*	CA 44	2.09295D+00	*	CA 46	2.83551D-01	*	CA 48	8.11197D-01
SC 45	7.35657D+00	*	TI 46	3.86841D+00	*	TI 47	1.64022D+00	*	TI 48	2.95866D-01	*	TI 49	4.76702D+00
TI 50	1.70246D+01	*	V 51	6.85826D-01	*	CR 52	1.53160D-01	*	CR 53	2.52386D-01	*	CR 54	1.51753D+01
MN 55	9.91586D-02	*	FE 54	3.57974D-04	*	FE 55	3.89530D+18	*	FE 56	8.50143D-02	*	FE 57	1.39485D+00
FE 58	6.73044D+01	*	CO 59	3.04181D+01	*	NI 58	1.23829D-04	*	NI 59	2.27340D+21	*	NI 60	7.54709D+00
NI 61	7.96415D+01	*	NI 62	5.08924D+01	*	NI 63	1.79150D+21	*	NI 64	2.09518D+02	*	CU 63	9.65592D+01
CU 65	2.82998D+02	*	ZN 64	4.57868D+01	*	ZN 66	1.62633D+02	*	ZN 67	2.40858D+02	*	ZN 68	2.61587D+02
ZN 70	9.27048D-02	*	GA 69	3.29629D+02	*	GA 71	4.50658D+02	*	GE 70	4.32213D+02	*	GE 72	3.56413D+02
GE 73	2.44304D+02	*	GE 74	1.97632D+02	*	GE 76	2.22385D-02	*	AS 75	1.21246D+02	*	SE 76	4.42434D+02
SE 77	1.86535D+02	*	SE 78	2.38398D+02	*	SE 79	1.37927D+19	*	SE 80	6.01347D+00	*	SE 82	1.08902D-02
BR 79	8.15973D+01	*	BR 81	9.04237D+00	*	KR 80	1.07681D+03	*	KR 81	7.85955D+23	*	KR 82	5.07806D+02
KR 83	1.48869D+02	*	KR 84	1.20834D+02	*	KR 86	3.86283D-01	*	RB 85	7.75415D+01	*	RB 87	3.40276D-01
SR 86	4.23174D+02	*	SR 87	3.78473D+02	*	SR 88	8.67820D+01	*	Y 89	5.10091D+01	*	ZR 90	1.77324D+01
ZR 91	2.11919D+01	*	ZR 92	1.61355D+01	*	ZR 93	2.01769D+22	*	ZR 94	1.04572D+01	*	ZR 96	7.48368D-02
NB 93	1.78993D-02	*	MO 94	5.89481D-02	*	MO 95	4.39077D+00	*	MO 96	9.64341D+00	*	MO 97	5.31846D+00
MO 98	6.27950D+00	*	MO100	5.63099D-11	*	TC 99	7.91134D+16	*	RU 98	9.24824D-24	*	RU 99	1.72907D+00
RU100	7.29525D+00	*	RU101	1.10046D+00	*	RU102	2.93579D+00	*	RU104	2.01712D-17	*	RH103	1.07955D+00
PD104	6.70671D+00	*	PD105	7.98501D-01	*	PD106	2.92973D+00	*	PD107	4.80139D+20	*	PD108	3.36822D+00
PD110	7.34736D-16	*	AG107	1.27494D-01	*	AG109	1.40064D+00	*	CD108	1.49082D+00	*	CD109	4.01910D+15
CD110	4.76043D+00	*	CD111	1.09122D+00	*	CD112	2.61088D+00	*	CD113	1.51988D+00	*	CD114	2.91101D+00
CD116	1.85995D-10	*	IN113	4.61618D-01	*	IN115	1.51846D+00	*	SN114	1.21776D-01	*	SN115	9.36498D-02
SN116	3.43787D+00	*	SN117	1.44651D+00	*	SN118	2.49114D+00	*	SN119	1.71821D+00	*	SN120	2.34707D+00
SN122	4.20274D-03	*	SN124	4.20274D-03	*	SB121	9.65157D-01	*	SB123	3.10836D-04	*	TE122	3.14848D+00
TE123	3.08825D+00	*	TE124	2.92759D+00	*	TE125	7.01727D-01	*	TE126	1.18128D+00	*	TE128	1.55621D-02
TE130	2.50484D-02	*	I 127	1.69362D-01	*	XE128	3.53903D+00	*	XE129	1.42228D-01	*	XE130	2.80472D+00
XE131	2.46598D-01	*	XE132	1.18371D+00	*	XE134	1.50981D-03	*	XE136	8.42654D-01	*	CS133	4.35427D-01
CS135	2.05422D+17	*	BA134	3.47047D+00	*	BA135	6.16732D-01	*	BA136	3.45689D+00	*	BA137	3.03671D+00
BA138	5.08375D+00	*	LA139	3.66282D+00	*	CE140	4.29518D+00	*	CE142	1.34915D-02	*	PR141	2.22345D+00
ND142	3.85810D+00	*	ND143	1.54883D+00	*	ND144	1.72475D+00	*	ND145	1.10500D+00	*	ND146	1.60076D+00
ND148	1.18562D-20	*	ND150	6.91593D-22	*	SM147	8.81114D-01	*	SM148	4.40833D+00	*	SM149	6.57452D-01
SM150	3.96956D+00	*	SM151	4.80844D+15	*	SM152	8.51414D-02	*	SM154	1.13215D-25	*	EU151	2.00894D-01
EU153	2.59949D-01	*	GD152	4.80895D+01	*	GD153	5.29368D+15	*	GD154	5.30083D+00	*	GD155	2.52196D-01
GD156	6.84665D-01	*	GD157	4.71358D-01	*	GD158	1.79704D+00	*	GD160	4.38630D-17	*	TB159	2.83744D-01
DY160	4.50211D+00	*	DY161	2.27972D-01	*	DY162	5.75495D-01	*	DY164	2.96068D-01	*	HO163	1.23791D-01
HO164	4.18846D+14	*	HO165	2.53208D-01	*	ER164	7.25480D+00	*	ER166	5.28329D-01	*	ER167	3.34215D-01
ER168	1.08614D+00	*	ER170	3.17363D-25	*	TM169	6.16164D-01	*	YB170	5.32166D+00	*	YB171	5.92462D-01
YB172	1.16658D+00	*	YB173	8.32450D-01	*	YB174	1.76301D+00	*	YB176	7.38211D-01	*	LU175	6.38880D-01
LU176	7.27748D-05	*	HF176	6.73586D+00	*	HF177	6.84789D-01	*	HF178	1.81905D+00	*	HF179	1.09384D+00
HF180	2.28669D+00	*	TA179	1.10992D+19	*	TA180	2.94994D+02	*	TA181	1.53955D+00	*	W 180	1.52769D-23
W 182	2.30764D+00	*	W 183	2.52953D+00	*	W 184	2.23914D+00	*	W 186	1.08329D-01	*	RE185	7.23171D-01
RE187	1.17705D-03	*	OS186	4.89718D+00	*	OS187	2.75073D+00	*	OS188	6.19841D-01	*	OS189	1.73125D-01
OS190	4.08009D-01	*	OS192	8.03289D-03	*	IR191	6.40892D-02	*	IR193	1.11574D-02	*	PT192	4.93640D+00
PT193	4.34375D+19	*	PT194	1.46039D-01	*	PT195	4.01503D-02	*	PT196	3.22375D-01	*	PT198	3.04624D-07
AU197	1.75004D-01	*	HG198	3.11506D+00	*	HG199	8.34675D-01	*	HG200	1.87524D+00	*	HG201	1.58308D+00
HG202	2.05599D+00	*	HG204	4.55216D-05	*	TL203	2.22315D+00	*	TL205	1.72992D-02	*	PB204	2.67469D+00
PB205	1.57327D+21	*	PB206	2.69842D+00	*	PB207	3.81860D+00	*	PB208	3.18657D+00	*	BI209	3.36077D-01
BI999	0.00000D+00	*											

Table 4.5: Final overabundances ($N_i(star)/N_i(init)$) at the end of core helium burning, for the two cases CFHZ85 (above) and CF88 (below).

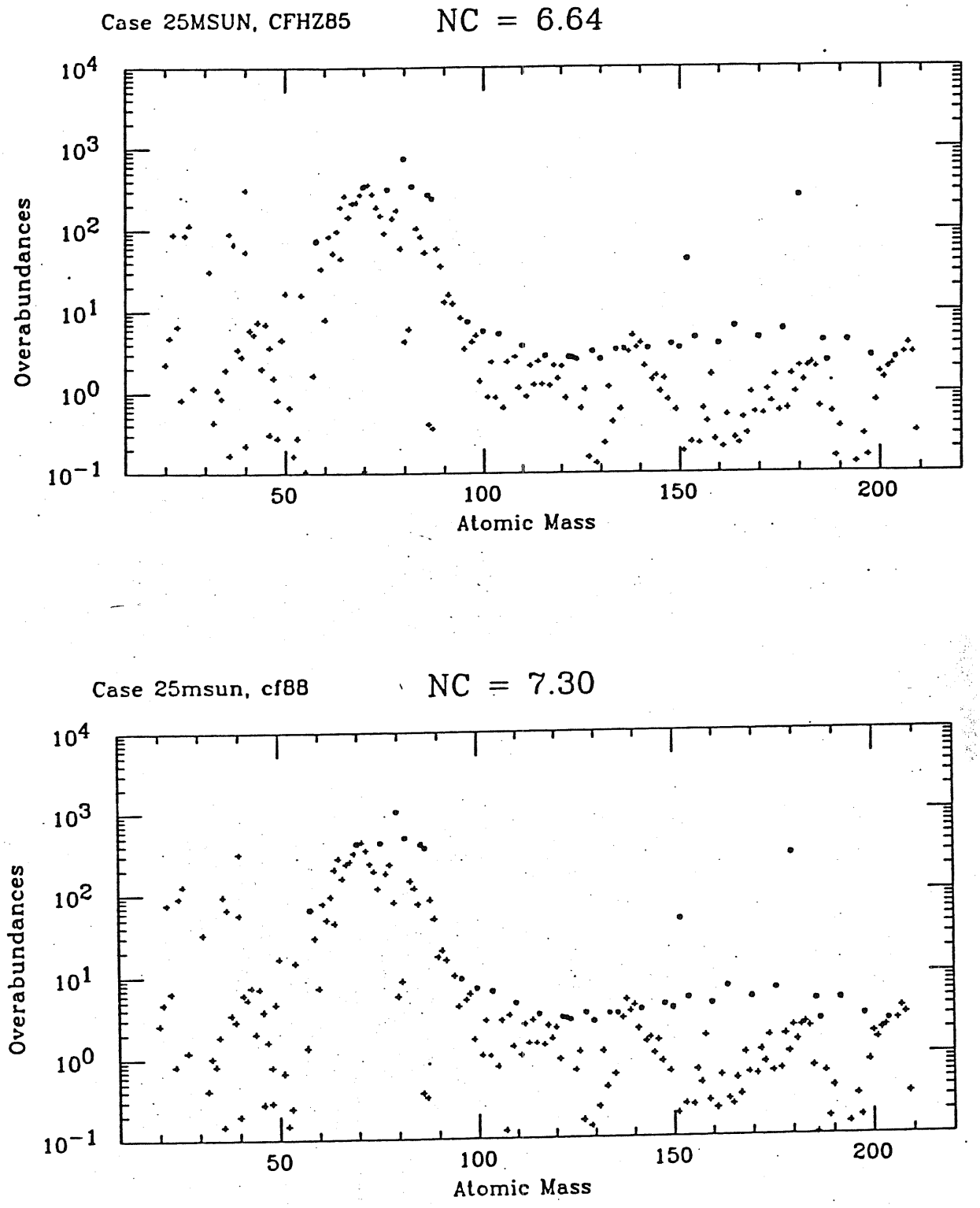

Figure 4.1: Overabundances as a function of the atomic mass number at central He–exhaustion for the two cases CFHZ85 (above) and CF88 (below).

LIGHT		HEAVY	
^{22}Ne	3.271	^{56}Fe	2.684
^{24}Mg	5.321	^{58}Fe	6.360
^{25}Mg	142.8	^{59}Co	7.301
^{26}Mg	2.239	^{60}Ni	7.984
^{29}Si	3.191	^{61}Ni	8.165
^{30}Si	4.504	^{62}Ni	7.960
^{23}Na	2.133	^{64}Ni	2.090
^{32}S	2.544	^{63}Cu	7.794

Table 4.6: $Y_l\sigma_{nl}$ values ($\times 10^{-5}$) for some characteristic nuclei at $T_{8c} \sim 3.0$ K and $\rho_c = 2277$ g/cm^{-3}.

efficiently captures neutrons allowing only a minor fraction of the neutrons released by the ^{22}Ne (α , γ) ^{25}Mg source to be captured by the iron seeds (Couch et al., 1974).

We would like to investigate this point by performing some numerical evaluations concerning the relative weigths as neutron absorbers of the various isotopes included in our network. Let us rewrite equation 4.2 as:

$$N_n = \rho N_A Y_\alpha \frac{\sum_j Y_j < \sigma v >_{\alpha j}}{\sum_l Y_l < \sigma v >_{nl}}, \tag{4.4}$$

where

$$Y_i \equiv \frac{X_i}{A_i} = \frac{N_i}{\rho N_A}$$

is the ratio between the mass fraction X_i and the atomic number A_i of element i, and N_A is the Avogadro's number. Since here the neutron production reaction is ^{22}Ne (α , n) ^{25}Mg, $\sum_j Y_j < \sigma v >_{\alpha j} = Y_{22} < \sigma v >_{\alpha 22}$, while the denominator tells us that the critical quantity for an estimate of the neutron depletion is the product of the abundance times the neutron capture cross section.

To be more precise, consider a given time when the central temperature is $T_{8c} \sim 3.0$ K and the central density is $\rho_c = 2277$ g/cm^{-3}.

Then $Y_\alpha = 2.692 \times 10^{-4}$, $Y_{22} = 5.451 \times 10^{-4}$, $N_A < \sigma v >_{\alpha 22} = 1.86 \times 10^{-11}$, and the numerator of equation 4.4 becomes 6.216×10^{-15} cm^{-3}.

As for the denominator, table 4.6 gives a list of some important $Y_l\sigma_{nl}$ contributions, distinguishing between light nuclei ($Z < 26$) and heavy ones ($Z \geq 26$).

The table shows that ^{25}Mg is by far the dominant neutron poison, and that a certain number of light nuclei have a neutron capture strength which is comparable to that of the iron seeds at this stage of evolution.

Taking into account all the terms the sum is 2.163×10^{-3}. With a KT = 30 KeV

thermal velocity of $v = 2.3974 \times 10^8$ cm/s, equation 4.4 yields: $N_n \sim 1.2 \times 10^7$ cm^{-3} for the central neutron density.

Indeed, had we considered the beginning of the ^{22}Ne burning, we would obtain very different results: ^{22}Ne and ^{56}Fe are at their maximum value then, and little ^{25}Mg or (for instance) ^{61}Ni have been synthetized. In this case we have $Y_l\sigma_{nl}$ values equal to 6.488×10^{-5} for ^{22}Ne, 1.754×10^{-5} for ^{25}Mg, 2.270×10^{-4} for ^{56}Fe, and only 1.004×10^{-6} for ^{61}Ni! Thus the relative importance of the neutron absorbers strongly depends on the time the evaluation is made at.

4.4.2 Two Remarkable Cases: ^{152}Gd and ^{180}Ta

We said that our 25 $M_\odot$ model produces large overabundances for the s–only isotopes with $A < 90$, while for higher atomic mass numbers the overproduction factors fall as a consequence of the neutron absorption by the poisoning elements. There are however two heavy isotopes which are greatly enhanced during the operation of the weak s–process. They are ^{152}Gd and ^{180}Ta.

By following the temporal evolution of their abundances (see figure 4.2) we can try to explain the reason why this large production occurs.

The neutron flow path around ^{152}Gd has been shown in figure 2.7. The neutron density is so low that the branchings at ^{152}Eu and ^{151}Sm let almost all the neutron flux follow the β^- decay channel during all the process. As a consequence, when the process begins ^{152}Gd, whose solar number abundance normalized to Si = 10^6 is only 0.00066 (Anders and Grevesse, 1989), is rapidly enhanced because of the destruction of ^{151}Eu, that has a solar abundance of 0.0465. The subsequent evolution depends only on the ^{150}Sm behaviour, which becomes its direct feeder. This is firstly produced by the arrival of the neutron flow to its atomic mass number, and then decreases as the flow goes beyond it. The final enhancement is due to the strong increase of the central temperature at the end of the process.

As far as ^{180}Ta is concerned, its way of production is under debate (Kappeler et al., 1989a,b). In our networks there is a branching point at ^{179}Hf and another one at ^{179}Ta, that communicate through a double channel of β^- and β^+ decays. Notice that ^{178}Hf has a solar–system abundance of 0.0420, while ^{180}Ta is only 2.48×10^{-6} so that little variations of the former can have enormous consequences for the latter, if the branching ratios are favourable.

The branching ratio at ^{179}Hf is very temperature–dependent: we have that while f_- =0.16 when the central temperature is $T_{8c} = 2.5$ K, it becomes 0.37 at $T_{8c} = 3.0$ K, and then goes up to ~ 1 at $T_{8c} = 3.5$ K [3]. In the meanwhile, the corresponding branching ratios at ^{179}Ta are: $f_+ = 0.94$, 0.92 and ~ 1. This means that the final very steep increase of ^{180}Ta is due to the complete opening of the ^{179}Hf beta decay channel caused by the large enhancement of the temperature.

[3] In this last part of the nucleosynthesis mechanism the average neutron density has decreased by two order of magnitudes with respect to its maximum value and thus λ_n has pratically no weigth.

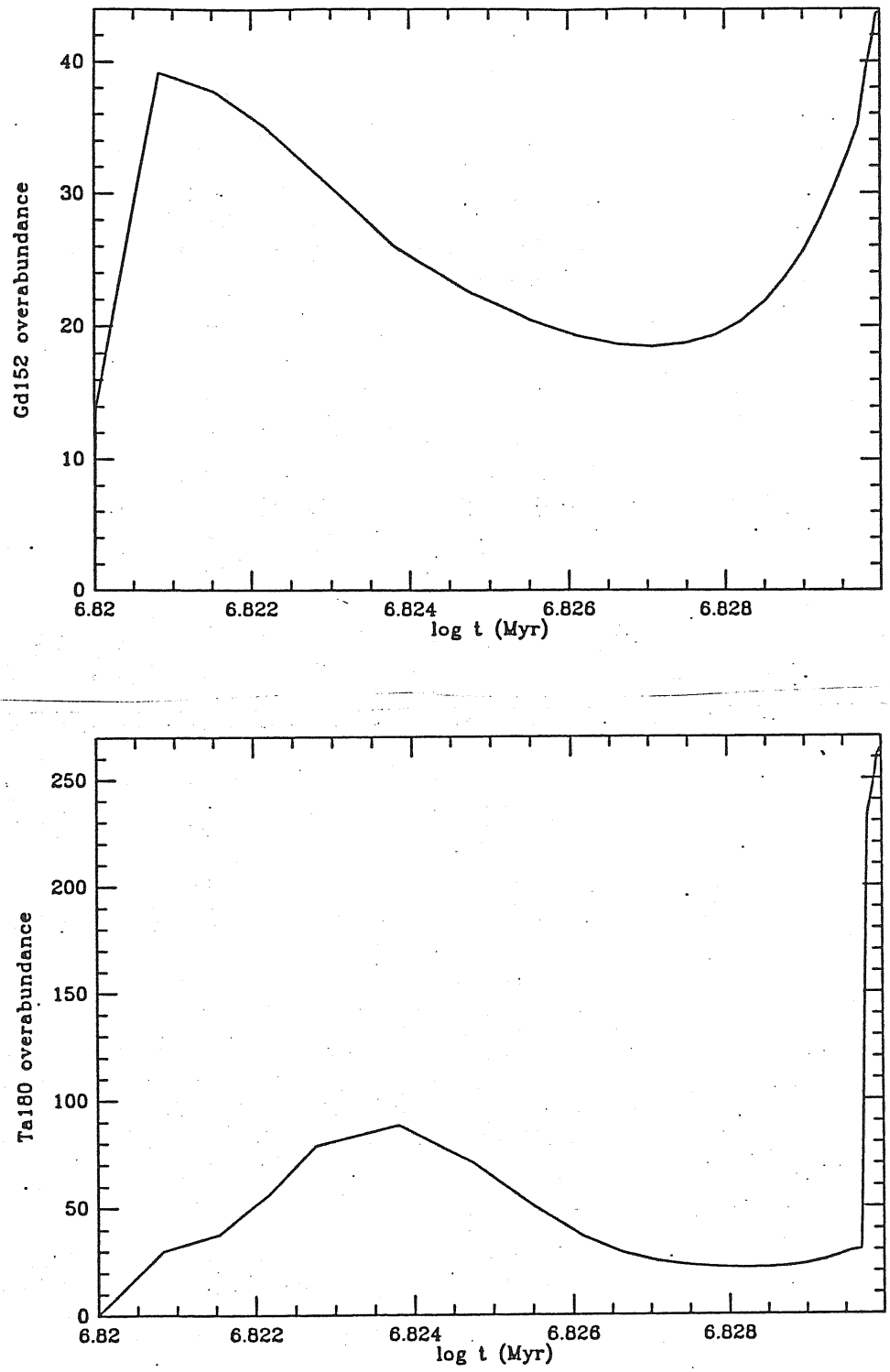

Figure 4.2: The evolution of ^{152}Gd (above) and ^{180}Ta (below) as a function of time

4.4.3 The Light Isotopes

We saw that some light isotopes are efficiently produced in our s–process calculation. Among them, ^{40}K is the best example, and its large overabundance has to be ascribed to the small neutron density acting on the ^{39}Ar branching: near all the flux is allowed to pass to ^{39}K through β^- decay and then, after n–capture, to ^{40}K, instead of going to ^{40}Ar with a direct capture of a neutron, or to ^{36}S via a (n,α) reaction.

But we must consider that up to now the possibility for beta decays of the long lived unstable isotopes has been neglected.

So let us imagine that the material that underwent neutron captures during central helium burning in our 25 $M_\odot$ model will stay some 10^4 years inside the star at a typical temperature of 5×10^8 K, and then be expelled into the interstellar medium, where it remains for 10^{10} yr. The radioactive nuclei will have time to decay according to their rates, and some isotopic abundances will change with respect to the values at central He–exhaustion.

We investigated this point and found out that the main results are:

- a fall of the ^{40}K overabundance, which goes from 310 to 2.5 because of the β^- decay to ^{40}Ca;
- a change of the ^{41}K overabundance from 5.9 to 7.0, due to the complete β^+ decay of ^{41}Ca;
- some heavy isotopes are also affected, such as ^{113}In and 115Sn which go from 0.34 to 32 and from 0.074 to 17 because of the β^- decays of ^{113}Cd and ^{115}In respectively.

Another point concerning the light isotopes is the set of beta decay rates adopted. We inserted in our network values extrapolated from the data by Fuller et al. (1982), which were derived for a higher temperatures range than the one we are concerned with, but we verified that substituting them with the Cosner and Truran (1981) weak interaction rates, calculated for lower temperatures, leads to no appreciable differences in the final overabundances. As a matter of fact, the most affected element is ^{36}S, being enhanced by only $\sim$ 4 %.

4.5 COMPARISONS

4.5.1 The CFHZ85 And The CF88 Cases

The main difference between the thermonuclear reaction rates compilations by Caughlan et al. (1985) and Caughlan and Fowler (1988) is the $^{12}C\ (\alpha\ ,\ \gamma\ )\ ^{16}O$ rate, which is a factor ~ 2 lower according to the most updated evaluation. We decided to perform our calculations with both the two sets of data because the α–capture rate on ^{12}C is still uncertain by a factor 2.

As for the evolutionary behaviour of the CF88 case, the same comments can be done that we already point out when comparing the CFHZ85 model with the FCZ75 one.

The s–process in the CF88 case gives results very close to the CFHZ85 one, but the overabundances are slightly enhanced, in particular for the $70 \leq A \leq 90$ isotopes.

As already stressed by Arnett and Thielemann (1985) , Busso and Gallino (1985), Prantzos et al. (1987), and Busso et al. (1988), a lower rate means that the competition between the $^{22}Ne\ (\alpha\ ,\ \gamma\ )\ ^{25}Mg$ and the $^{12}C\ (\alpha\ ,\ \gamma\ )\ ^{16}O$ reactions (which is very strong at the temperatures and densities we are concerned with) decreases, allowing more α–particles to be captured by ^{22}Ne, thus enhancing the production of neutrons. This is not a very strong effect: at the end of He–burning the ^{22}Ne mass fraction burnt is 0.0124 in the CFHZ85 case, and 0.0138 in the CF88 one, that is ^{22}Ne has decreased to 48% of its initial value in the first run, and to 42% in the second one. As a consequence, the number of neutrons captured per iron seed nucleus is increased by only 10% going from 6.45 in the CFHZ85 case to 7.10 in CF88, and the neutron exposure is enhanced from 0.224 to 0.239.

In figure 4.3 we have plotted the behaviour of the mean neutron density as a function of time for the two cases. Notice that for any given time the CF88 model shows a higher mean neutron density, but the run stops before, and so the maximum value that the mean neutron density is able to reach is lower than in the CFHZ85 model. Anyway, if we calculate the time averaged mean neutron density as:

$$N_n = \frac{1}{\Delta t} \int N_n(t) dt,$$

we obtain a value of 1.921×10^5 for CFHZ85, and 2.103×10^5 for CF88, that is an increase of 9% that explains why τ is higher by 7% even if the duration of the process is lower by 3%. This result is in agreement with what Arnett and Thielemann (1985) and Busso and Gallino (1985) have found, but is in opposition with the results of Bencivenni et al. (1987), who used the same evolutionary code we used. The latter authors obtained an increased s–processing efficiency when a higher rate was adopted that was explained in terms of a longer duration of the nucleosynthetic event. But as Arnett (1972a,b) showed, the whole story of a massive star can be told choosing the helium abundance X_α as independent variable instead of the time,

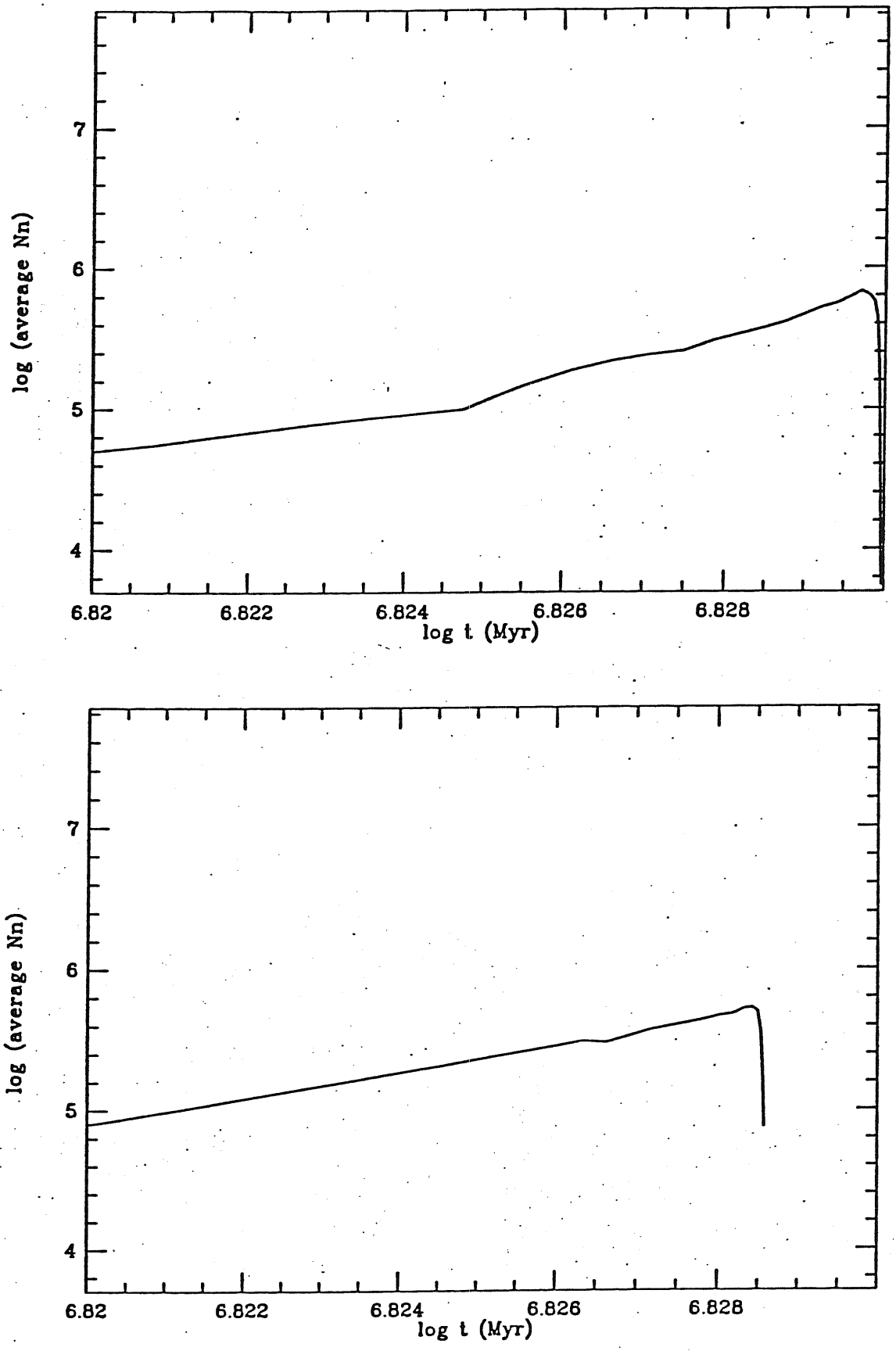

Figure 4.3: The temporal behaviour of the mean neutron density in the two cases CFHZ85 (above) and CF88 (below).

and our evolutionary data tell us that for a given X_α the central temperature and density do not change between the two models with different $^{12}C(\alpha\,,\,\gamma)^{16}O$ rate. What is important then is the higher ratio between the $^{22}Ne(\alpha\,,n)^{25}Mg$ rate and the $^{12}C(\alpha\,,\,\gamma)\,^{16}O$ one in the CF88 case.

4.5.2 Comparison With Previous Results

The comparison between our results and the results of previous works is some hard to perform because a lot of parameters are involved whose changing in time is sometimes not easy to follow.

If on the whole the evolutionary models agree on the main features of our star-story, there are a lot of details which can differ and play important roles when the nucleosynthesis calculations are made.

Moreover cross sections, thermonuclear reaction rates and beta-decay rates are continuously changing as long as better determinations are available.

Let us try to make some comments anyhow.

Arnett and Thielemann (1985) analized core helium and core carbon burning in stars of M_α = 1.5, 2, 4, 8 and 16 $M_\odot$ with a polytropic treatment of the convective core. Unfortunately their nuclear network was very limited, stopping at ^{74}Ge. During the core He-burning phase, they found a substantial production of light nuclei such as ^{21}Ne, ^{22}Ne, ^{25}Mg, ^{26}Mg, ^{36}S, ^{40}Ar, ^{58}Fe and ^{37}Cl for stars with main sequence mass greater than 15 $M_\odot$ ($M_\alpha \geq 4\ M_\odot$). As for the production of s-only isotopes the smaller masses (M_α = 1.5, 2, 4 $M_\odot$) produce only ^{58}Fe, while a M_α = 8 $M_\odot$ star shows overabundances averaged about 50 and a M_α = 16 $M_\odot$ star about 100. They also stressed the importance of an enhancement in the $^{12}C\ (\alpha\,,\,\gamma)\ ^{16}O$ rate, which can make the overabundances fall by a factor 2. First of all we must explain why their process in a M_α = 8 $M_\odot$ model, which should correspond to a 22-25 $M_\odot$ main sequence star, is so weak with respect to ours. An important point is the ^{22}Ne neutron-capture cross section: Arnett and Thielemann adopted the 0.5 mb value recommended by Woosley et al. (1978), while we have a value of 0.06 mb (Winters and Macklin, 1988). In our work ^{22}Ne is a good absorber, but with a neutron cross section nearly ten times higher it becomes the most important poison! We run a case with the old cross section and we saw that while there are only small differences in the overproduction factors for the light elements, the overabundances for the heavy isotopes are decreased by a factor of $\sim$ 3, bringing our results in better agreement with those of Arnett and Thielemann for the M_α = 8 $M_\odot$ model.

Let us examine the work by Busso and Gallino (1985) now. They run 3 cases in order to check the influence of variations on both the $^{12}C\ (\alpha\,,\,\gamma)\ ^{16}O$ reaction rate and the ^{22}Ne neutron capture cross section. They considered models of M_α = 4, 8, 16, 32 $M_\odot$ stars from Arnett (1972a) and adopted a very extensive network of 246 isotopes, up to ^{204}Pb. In the best case (their case A) they found a good production of the light elements, and in the atomic mass range $60 \leq A \leq 90$ they got overabundances of $10 \div 100$. Adopting an increased $^{12}C\ (\alpha\,,\,\gamma)\ ^{16}O$ rate the

nucleosynthesis was slightly less efficient (case B), while rising the ^{22}Ne neutron–capture cross section from the 0.05 mb value given by Lamb et al. (1977) to the 0.9 mb value proposed by Almeida and Kappeler (1983) (case C) causes the light n–rich isotopes to be reduced by a factor of 1.5 $\div$ 3.5 with respect to case A and the 60 $\leq A \leq$ 90 ones to be very poorly produced. Busso and Gallino's case B in principle corresponds to our CFHZ85 case, while our CF88 case is intermediate between their case A and case B, but why these authors obtained such low overabundances that forced them to conclude with the suggestion that another site for the weak component of the s–process must be found?

Some changes in critical cross sections are important to explain the different shape of the s–process path in Busso and Gallino's case and in ours. In particular, they found a fall in the overabundances after a value for the atomic mass number of, $A \simeq 70$. In this region, a critical isotope is ^{68}Zn, whose cross section has changed from 11 mb of Woosley et al. (1978) to 19.2 mb of Bao and Kappeler (1987). We made a calculation with the old value in the CFHZ85 case, and we saw that while n_c didn't change in a sensible way, ^{70}Ge decreased by 26%, ^{76}Se and ^{80}Kr by 28%, ^{82}Kr ^{86}Sr and ^{87}Sr by 29%. This is quite an important result, considering that ^{68}Zn is not the only isotope whose neutron capture cross section has recently been enhanced: other isotopes which experienced the same story and whose abundances during the operation of the s–process are high are: ^{60}Ni, ^{63}Cu, ^{65}Cu and ^{66}Zn. What happens when a case is run with the Woosley et al. (1978) neutron–capture cross sections for all these nuclides? We checked this point, but in order to be consistent we had to increase the ^{56}Fe cross section up to 19 mb instead of the 11–13 mb we have now. As a result, ^{70}Ge decreased by 53%, ^{76}Se by 62%, ^{80}Kr by 64%, and ^{82}Kr, ^{86}Sr, ^{87}Sr by 66% in comparison to the standard case.

A large gap remains anyway between our results and Busso and Gallino's, even if the "Woosley 1978" case goes closer to their data. The gap is related to the very high difference in n_c, which may be determined by differencies in the stellar models. A quite critical point may be the fact that Arnett's stars have constant core masses for all the helium core burning phase, while our star convective core shrinks in mass during the final stages of the He–burning. In figure 4.4 we plotted the behaviour of the neutron density as a function of mass fraction at the beginning of the core helium burning, normalized to the central value. The shape of this gradient will not change in time, but in our models the shrinkage of the core makes the mean neutron density get higher and higher. In other words, as the evolution goes on, the convective mixing is restricted to matter that has seen more and more neutrons. If the core mass is fixed, on the contrary, the mixing produce a stronger dilution of neutrons and the nucleosynthesis mechanism is damped.

We can also try to make a comparison with the work of Lamb et al. (1977) that studied the neutron capture nucleosynthesis during core helium burning for a 15 $M_\odot$ and a 25 $M_\odot$ stars using models computed by Lamb et al. (1976) and for a 9 $M_\odot$ star following a model by Iben (1972). They also simulated a 50 $M_\odot$ star by imposing a total exhaustion of ^{22}Ne in the core at the end of helium

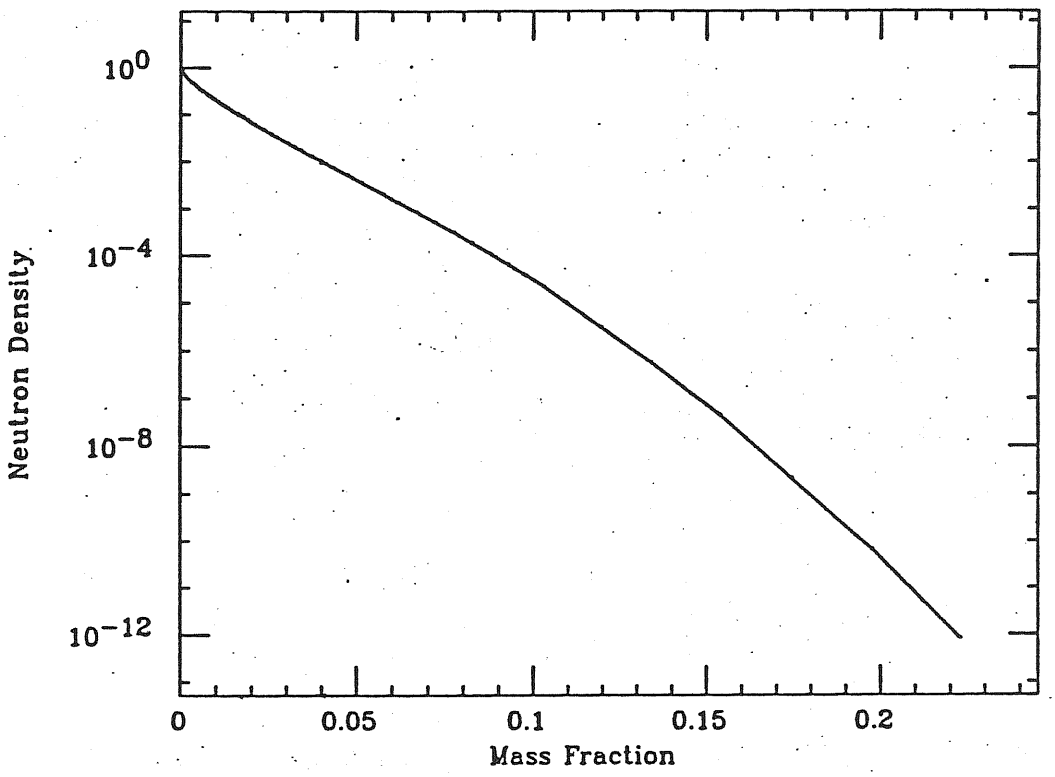

Figure 4.4: The neutron density normalized to the central value as a function of the mass fraction, at the beginning of core helium burning.

burning. They found that the most important enhancements are those for ^{25}Mg ^{26}Mg, ^{36}S, ^{37}Cl, ^{40}Ar, ^{40}K and ^{58}Fe, which are produced early during the s–process nucleosynthesis story. Just beyond ^{56}Fe and up to Sr they got enhancements of 50 $\div$ 100 for the s–only isotopes, while for $A \geq 90$ the overabundances go down to a value of $\sim$ 10. Their s–process is less efficient than ours, too: in particular for the 25 $M_\odot$ star they find a value of n_c equal to 4.6. Let us say first that their paper shows some inconsistencies if we look at the overabundances versus mass number plot (their figure 1) and then to the overabundances given in table 2; their figure 2 then shows some mistakes in the plot of overabundances as a function of time (the final behaviours of ^{4}He and ^{22}Ne have been exchanged, and the curves labeled ^{87}Sr and ^{70}Zn are unrealable). Coming back to our discussion, note that they use the thermonuclear reaction rates by FCZ71 for the 3α and ^{12}C (α, γ) ^{16}O reactions, that is a 3α which is less efficient than ours (by a factor $\sim$ 0.6), and a ^{12}C (α, γ) ^{16}O rate that is comparable with the CF88 one. So in principle their 25 $M_\odot$ model can be compared to our CF88 case, but since they adopted a lower 3α reaction rate, in their model the temperature tends to be higher and the He–burning proceeds slower: α–captures on ^{12}C are favoured and this means that in order to produce the same amount of energy only one helium nucleus instead of three has to be consumed (Bencivenni et al., 1987). When temperatures are high enough to allow the ^{22}Ne to burn with the consequent releasing of neutrons, Lamb et al.'s star has a higher He–content, and so a larger amount of α–particles is available for captures on ^{22}Ne and more neutrons are produced. From this would follow directly that the number of neutrons captured per iron seed nucleus is higher and the overabundances should be larger than in our case. But fortunately this is not the end of the story. Lamb et al. used the Cameron (1973) compilation of solar–system abundances. This means that the initial (pre–main sequence) CNO mass fraction and as a consequence the ^{22}Ne mass fraction at the beginning of core He–burning is lower than for us: they have $X_{22} = 0.0176$, while we've got 0.0238. A lower amount of ^{22}Ne implies that less neutrons can be released. But on the other side Cameron in 1973 gave a ^{56}Fe number density that is smaller by a factor of 0.92 with respect to the Anders and Grevesse (1989) data we use. Taking into account these considerations and adopting the values Lamb et al. inserted in their network for the neutron–capture cross sections of the most important isotopes (the major neutron absorbers – from Iben, 1975 and Allen et al., 1971), we performed a check–calculation. The result was extremely good in reproducing their findings. The only point is that in our simulation ^{58}Fe and ^{76}Se are lower, but our neutron cross sections for these nuclei are greater than those given by Allen et al. (1971), so that ^{58}Fe and ^{76}Se are more rapidly destroyed.

Very recently Langer et al. (1989) computed the evolution of a 15 $M_\odot$ star (M15) and a 30 $M_\odot$ one (M30) with initial composition $X = 0.7$, $Z = 0.03$ and using the Cameron (1982) compilation of solar–system abundances. Their models include mass loss according to the formulation by Lamers (1981) for hot stars ($T_e >$ 6500 K) and Reimers (1975) for cooler ones, and the 30 $M_\odot$ was also run with a

LANGER ET AL.('89)				THIS WORK
	M15	M30	MO30	M25
τ_H (Myr)	12.56	5.92	6.60	6.10
M_α ($M_\odot$)	2.70	7.60	11.10	6.77
$\log T_c$ (X=0)	7.97	8.01	8.02	7.90
$\log \rho_c$ (X=0)	2.67	1.99	1.88	1.68
τ_{He} (Myr)	2.14	0.91	0.86	0.63
M_α ($M_\odot$)	4.02	9.75	13.50	8.88
M_{CO}($M_\odot$)	2.37	7.79	12.26	6.29
$\log T_c$ (Y=0)	8.52	8.82	8.72	8.54
$\log \rho_c$ (Y=0)	3.83	4.59	3.92	3.52

Table 4.7: Comparison between the evolutionary features of the Langer et al. (1989) models and our standard model.

core overshooting of $l = 0.4H_p$ (MO30).

Table 4.7 shows some features of their models and the same quantities for our standard case. The upper part refers to H–burning, while the lower part concerns the He–burning.

There is a trend of our having a cooler and less compact object for which the helium burning phase is shorter. At helium exhaustion, the central conditions for the 25 $M_\odot$ we run are much closer to those of the Langer et al.'s M15, but the carbon–oxygen core is almost three times bigger. In their M15 star good production factors are found only for the light nuclei, while the overabundances of the s–only isotopes in the $70 \leq A \leq 90$ range increase in the M30 model and even more in the MO30 one. The most overproduced species are ^{40}K, ^{58}Fe, ^{65}Cu and ^{80}Kr.

If we want to compare these findings with our results, it is necessary to consider that Langer et al. used the Almeida and Kappeler (1983) neutron cross section for ^{22}Ne, that is $\sigma_{22} = 0.9 \pm 0.7$ mb. It is not surprising then that their process is so weak!

We run a case with $\sigma_{22} = 0.9$ mb in order to see the behaviour of our abundances in this case; the main trends we noticed are:

- a large increase of ^{23}Na, which is produced by neutron capture on ^{22}Ne and subsequent β^- decay of ^{23}Ne;
- a sensible increase of ^{58}Fe that is now 109 instead of 74;
- a strong decrease of all the overproduction factors starting from ^{64}Ni; in particular, ^{70}Ge falls from 348 down to 64, ^{76}Se from 327 to 39, ^{80}Kr from 769 to 81, ^{82}Kr from 355 to 36, ^{86}Sr from 280 to 31, and ^{87}Sr from 248 to 30.

This points out the extreme importance of the ^{22}Ne neutron capture cross section, and reconciles what we have found with Langer et al.'s M15 and M30 models, since our simulation sets in between them.

Finally, we would like to mention the work by Prantzos et al. (1987), who considered stars of 50, 60, 80 and 100 $M_\odot$ evolved by Prantzos et al. (1986) with mass loss and core overshooting. These massive stars are identified with Wolf–Rayet stars, and their evolutionary features are strongly affected by mass loss, which is able to convert a ZAMS 50 $M_\odot$ into a 22 $M_\odot$ at the end of core helium–burning. They give detailed data for the 60 $M_\odot$ model.

A short ($\sim$ 500 yr) neutron burst producing a neutron density of $\sim 3 \times 10^8$ cm^{-3} is found to occur just before helium ignition in the core, with pratically no consequences on the abundances of all isotopes but ^{40}K. It is due to α–captures on the little ^{13}C left after H–burning. When the temperature is high enough for ^{22}Ne to be burnt, a second neutron episode with a maximum central density of $\sim 10^7$ cm^{-3} produces substantial overabundances (larger than 50) of the light nuclei ^{23}Na, ^{25}Mg, ^{26}Mg, ^{36}S, ^{37}Cl, ^{40}K, while in the range $56 < A < 90$ overproduction factors of 250–775 are found for ^{65}Cu, ^{69}Ga, ^{71}Ga, ^{70}Ge, ^{72}Ge, ^{76}Se, ^{80}Kr, ^{82}Kr, ^{86}Sr, and ^{87}Sr. Prantzos et al. stressed the reduction in the s–process efficiency they got, which was ascribed to the $\sigma_{22} = 0.9$ mb and the high CFHZ85 reaction rate for the α–capture on ^{12}C they adopted. As a matter of fact, they obtain for the 60 $M_\odot$ star $n_c \approx 6.1$ and $\tau \approx 2.3 \times 10^{26}$ n/cm^{-2}, while we have for our 25 $M_\odot$ star $n_c = 6.4$ (starting from ^{56}Fe as seed) and $\tau = 2.2 \times 10^{26}$ n/cm^{-2}, and also our overabundances are comparable to theirs. They found that with $\sigma_{22} = 0.05$, n_c increased up to 9.5, and τ to 5.1×10^{26} n/cm^{-2}.

4.6 HINTS FOR THE s–PROCESS IN LOW METALLICITY STARS

The evolutionary calculations we reported in chapter 1 told us that as in the case of variations in the $^{12}C\ (\alpha\ ,\ \gamma\ )\ ^{16}O$ rate, also changes in the initial metal content do not affect the behaviour of the central physical conditions as a function of the helium mass fraction.

Moreover, both the fraction of iron seeds and the ^{22}Ne mass fraction at the beginning of the process scale with Z in the same way (the ^{22}Ne abundance depends on the CNO initial content), so that there is not a poison to seed ratio variation effect at the beginning of the process.

The s–process efficiency as a function of the initial content must be discussed again in terms of the competition among the various α-capture reactions. We would expect that in a lower metallicity star fewer helium nuclei could be captured by ^{22}Ne because of its lower abundance, and the resulting s–process would be weakened.

A confirmation of this suggestion comes from the low mass stars: in the computations by Gallino et al. (1988) and Gallino (1988) it is found that two neutron bursts are released during each thermal pulse. The first one is due to the ^{13}C source acting during the low temperature phase of the convective episode, while the second one becomes effective when the temperature increases and some ^{22}Ne is burnt. As we said while describing the neutron sources in a He–burning environment the ^{13}C source is metal independent, because the ^{13}C available is of primary origin. Thus those nuclei whose production is not affected by the high temperature phase, have higher production factors for lower metallicities, since the only effect they feel is a higher neutron irradiation, which is due to the lower fraction of iron seeds. On the contrary, there are nuclei, such as ^{86}Sr,^{87}Sr,^{80}Kr, ^{152}Gd,^{180}Ta, that are strongly dependent on the high temperature neutron burst. These nuclei are supposed to behave like the isotopes we are concerned with in our massive stars. The cited authors have performed a whole set of computations for various Z and they have found that those nuclei which are created by the ^{22}Ne source decrese when a lower metal content is adopted, in agreement with our thought.

In order to clarify this point, we decided to make a simulation of the population II model, with $Z = 0.001$ and a solar distribution of the heavy isotopic abundances properly scaled according to Z. We found that at the end of core helium burning τ diminishes by 8%, and n_c by 11%. As for the behaviour of the various isotopes compared with the solar one:

- the abundance of ^{12}C is the same; that of ^{16}O is slightly enhanced;
- a large production of ^{20}Ne is obtained since its overabundance is now 33.4 while it was 2.24; also ^{21}Ne is greatly enhanced: from 4.8 up to 23;
- the overproduction factor of ^{22}Ne is nearly the same, as ^{56}Fe ;

- apart from ^{58}Fe whose overabundance increases from 74 to 83, there is a general trend to have lower overabundances in the $Z = 0.001$ case, a feature which becomes stronger with increasing A. In particular, ^{40}K goes from 310 of the $Z = 0.02$ run to 292 of the $Z = 0.001$ one (-6%), ^{70}Ge from 348 to 257 (-35%), ^{76}Se from 327 to 217 (-51%), ^{80}Kr from 769 to 490 (-57%), ^{82}Kr from 355 to 221 (-61%), ^{86}Sr from 280 to 166 (-69%), and ^{87}Sr from 248 to 146 (-70%).

The explanation for these results is the following: since now we have 20 times less ^{22}Ne the α–particles are mostly captured via the ^{12}C (α, γ) ^{16}O (α, γ) ^{20}Ne chain, decreasing the production of neutrons. Moreover, a lot of ^{20}Ne is built up and through n–capture on ^{20}Ne a large amount of ^{21}Ne is created too. As a matter of fact, if in the solar case ^{20}Ne counts as a neutron poison only for 0.79% of the ^{25}Mg (at $T_{8c} \sim 3.0$ K), now the ratio gives 7.09%.

Chapter 5

THE WEAK s–PROCESS AND THE CHEMICAL ENRICHMENT OF THE GALAXY

5.1 INTRODUCTION

In the previous chapter we showed the results obtained by following the neutron capture nucleosynthesis during core helium burning of a 25 $M_{\odot}$ star.

The final overabundances at helium exhaustion were plotted in figure 4.1 as a function of the atomic mass number.

Before examining the galactic chemical enrichment of s–only isotopes, we must discuss two fundamental points: the first one deals with the story of the s–processed material after core helium burning, and the possibility that it can suffer further nucleosynthetic episodes before being ejected by the supernova explosion. The second one concerns a discussion of the s–process efficiency in stars of different masses which make up a stellar generation.

5.2 THE EVOLUTION AFTER CORE HELIUM BURNING

5.2.1 The Helium Shell Burning Phase

During the last stages of core helium burning, the shrinkage in mass of the convective core leaves matter with a variable chemical composition behind. However, concerning the s–processed material, owing to the very steep contraction of the convective core, the actual inhomogeneity is confined only to the outer 0.5 $M_\odot$, because at this time the integrated neutron exposure is pratically frozen. In any case, at core central exhaustion, a He–shell develops which rapidly smooths the chemical profiles of the carbon–oxygen core up to its external border.A possible contribution by the shell He–burning to the s–process could only occur during the temporal interval going from its ignition up to the first stages of carbon burning, because after that the temperature at the shell location decreases, and the ^{22}Ne meanlife against α–capture becomes much longer than the timescales characterizing the subsequent evolutionary stages, so that neutrons can no longer be released.

Investigations of the neutron capture nucleosynthesis occurring during this phase were done by Arcoragi (1986) and by Busso et al. (1987).

Arcoragi followed this process in a 15 and in a 30 $M_\odot$ stars evolved by Weaver et al. (1978) and Langer (1986a), concluding that no significant s–processing occurs in the He burning shell.

Busso et al. (1987) studied stars with helium core masses of 4 and 8 $M_\odot$ according to the models of Arnett (1972a,b) and found that only for the more massive star the radiative shell can be an efficient source of s–elements up to $A = 70 \div 80$. Its effect would be to increase the abundances left behind by the previous burning in the various zones of the core, so that the final mean abundances tend to become similar to the central ones.

We followed the evolution of a 25 $M_\odot$ up to central ^{12}C exhaustion and we found that the physical conditions in the He–shell are never suitable for the activation of the $^{22}Ne(\alpha,n)^{25}Mg$ reaction.

These results allow us to conclude that the helium shell phase cannot change in a sensible way the abundances obtained during the previous core helium burning phase.

5.2.2 The Carbon Burning Phase

When the central temperature reaches a value of $\sim 7 \times 10^8$ K, the carbon burning phase begins, whose features strongly depend upon the $^{12}C(\alpha,\gamma)^{16}O$ rate that operated in the previous He–burning phase. However, we have already stressed in chapter 2 that the present evaluation of this rate is poorly known, being uncertain by a factor of two, according to CF88. This is a very unpleasant situation,

since the advanced stages of evolution of massive stars are strongly affected by this uncertainty, leading to difficulties on the final scenario concerning the supernova event. This clearly comes out when considering that the $^{12}C(\alpha,\gamma)^{16}O$ reaction could or could not be competitive with the $^{16}O(\alpha,\gamma)^{20}Ne$ reaction operating near He depletion. When the low FCZ75 α–rate is used, a consistent amount of ^{12}C is left after He–exaustion, so that carbon burning ignites as a well developed, exoergic, convective burning stage (Arnett, 1972b); with the three times higher rate of CFHZ85, stars more massive than about 20 $M_\odot$ produce so little carbon during helium burning, that the following carbon and neon nuclear stages of stellar evolution are essentially skipped (Woosley and Weaver, 1986; Woosley, 1986). In this case the trace abundances of carbon and neon then burn away radiatively, without nuclear energy generation ever exceeding neutrino losses.

With an intermediate rate which roughly correspond to CF88, Lamb et al. (1976) saw that while in a 15 $M_\odot$ star a little carbon convective core can develop, in a 25 $M_\odot$ star carbon burns radiatively. With our 25 $M_\odot$ model run with the CF88 set of thermonuclear reaction rates, we found a complete agreement with the Lamb et al. (1976) results, that is no central convection was found during the carbon burning stage.

As for the possibility of s–processing during this phase, it is important to notice that not all the ^{22}Ne is consumed during He burning, particularly for the less massive stars, and that this residual ^{22}Ne is completely burnt at the very beginning of ^{12}C burning (Arnett and Truran, 1969), when α particles are released by the $^{12}C(^{12}C,\alpha)^{20}Ne$ and $^{12}C(^{12}C,p)^{23}Na(p,\alpha)^{20}Ne$ reactions. Consequently, neutrons can now be released by α–captures on ^{22}Ne.

At the low temperatures ($T\simeq 8\times10^8$ K) characterizing the less massive stars ($M\leq 15\ M_\odot$) a good production of neutrons is also supplied by the reaction chain $^{12}C(p,\gamma)^{13}N(\beta^+)\ ^{13}C(\alpha,n)^{16}O$, while only for the most massive stars, in which C–burning is activated at fairly high temperatures ($T\geq 10^9$), some contribution can be expected from the reaction $^{12}C(^{12}C,n)^{23}Mg$.

Calculations of the neutron capture nucleosynthesis occurring during carbon burning in a convective scenario were performed by Gallino and Busso (1985) and Arnett and Thielemann (1985), while Arcoragi (1986) studied the case of radiative carbon burning. In the first paper, Gallino and Busso found a not negligible synthesis of the s–nuclei, but they pointed out that this mechanism cannot be considered a pure s–process, but rather a neutron capture process intermediated between the s– and the r– ones, since neutron densities of $N_n \sim 10^{12}$ ncm^{-3} are involved.

Substantial overabundances for the light s–nuclei at the end of core carbon burning were also obtained by Arnett and Thielemann and by Arcoragi.

Anyway, it is reasonable to suppose that most of this carbon processed material will be locked up into the stellar remnant left by the supernova explosion, and will not participate to the chemical evolution of the Galaxy.

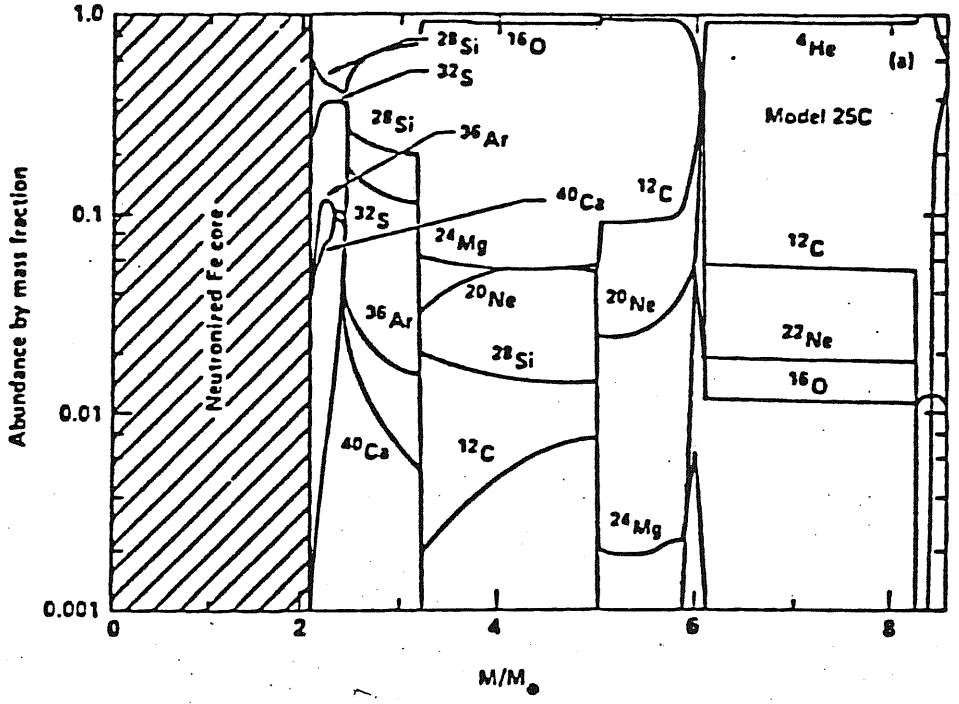

Figure 5.1: The chemical composition of a 25 $M_\odot$ star just before the core collapse. (Woosley and Weaver, 1986).

5.2.3 Up To The Supernova

In order to briefly describe the evolution after carbon burning we shall follow the results obtained by Woosley and Weaver (1986) for a 25 $M_\odot$ star, adopting the $^{12}C(\alpha,\gamma)^{16}O$ rate by CFHZ85. They found that carbon is depleted radiatively out to a mass of about 2.5 $M_\odot$, while neon burns radiatively out to about 1.5 $M_\odot$. Then oxygen burns in a convective core first out to about 1.35 $M_\odot$ and after in a convective shell out to 2.4 $M_\odot$. Silicon burns out to 1.3 $M_\odot$, and then a silicon convective shell burns out to 2.1 $M_\odot$ before the core collapses. In figure 5.1 the composition of this model at the onset of core collapse is shown.

Following the shock passage the pre–explosive composition is substantially altered out to about 3.0 $M_\odot$. This means that nearly half of the carbon–oxygen material, containing the results of the s–process occurred during core helium burning, is ejected without further processing.

This again stresses the major importance of the core helium burning phase as the best site for the production of the light s–only isotopes that can enrich the interstellar medium.

^{58}Fe	74
^{70}Ge	385
^{76}Se	362
^{80}Kr	905
^{82}Kr	366
^{86}Sr	289
^{87}Sr	248
^{86}Kr	0.41
^{87}Rb	0.36

Table 5.1: p–Corrected overabundances at helium core exhaustion.

5.3 STEPS TOWARDS THE BUILD UP OF THE WEAK s–COMPONENT

5.3.1 A Deeper Analysis Of s–Processing In A 25 $M_\odot$ Star

The discussion of the previous paragraph led us to the conclusion that in order to explain the solar distribution of the light s–only elements, we must concentrate on the core helium burning yields. In particular, we saw that probably half of the carbon–oxygen core of a 25 $M_\odot$ star is ejected by the supernova explosion unaltered.

However, a small correction to the final overabundances is necessary, in order to compare the results of our calculation with the s–process contribution to the solar abundances. Indeed, most of the s–only nuclides are more or less affected by a p–process contribution. We adopted the fractional p–corrections to s–only abundances quoted by Kappeler et al. (1989a): while ^{58}Fe is given no p–contribution, ^{70}Ge and ^{76}Se have a 9.7 % correction, ^{80}Kr a 15 %, ^{82}Kr a 3.0 %, ^{86}Sr a 5.6 % correction; no correction is found for ^{87}Sr. Since the p–corrections must be scaled from the initial solar abundance, the final overabundances are increased accordingly.

If we now go back to the results we obtained for a 25 $M_\odot$ at core He–exhaustion and we concentrate on the s–only nuclides with $A \leq 90$, table 5.1 shows that a very large spread exists in the final overabundances (p–corrected), going from 74 for ^{58}Fe to 385 for ^{70}Ge, up to 905 for ^{80}Kr.

The first four isotopes tabulated are essentially affected by the weak component alone.In particular, ^{58}Fe is not a s–only isotope, but attempts to produce it in other ways besides the weak component have been unsuccesful up to now, so that it can be considered as totally produced by the process we are investigating.

The large spreads of the results means that the s–processed abundances by a 25 $M_\odot$ star alone are not suitable for reproducing the weak component.

5.3.2 Criticisms To The Classical Analysis

The classical analysis of the s–process is a phenomenological approach that does not take into account the astrophysical prescriptions, as it assumes a steady neutron flux with constant neutron density and temperature. These parameters are derived by looking at the behaviour of the neutron flow at branching points.

We already stressed that the investigation of the weak component by the classical analysis is not a direct one, but it is mediated by the results obtained for the main component, through a detailed analysis of the branchings occurring at ^{79}Se and ^{85}Kr (Kappeler et al, 1989a,b). Indeed, the main component provides a not negligible contribution to the s–only isotopes involved in these branchings, i.e. ^{80}Kr, ^{82}Kr, ^{86}Sr, and ^{87}Sr. The main difficulty comes from the treatment of the ^{85}Kr branching, a very delicate question that up to now can give a satisfactory answer neither for the main component, that yields overproduction factors of 1.65 and 1.12 for the two ^{85}Kr branching dependent isotopes ^{86}Kr and ^{87}Rb, even if the contributions from the r–process or from the weak s–process are neglected. This overproduction can only be removed by treating the ^{85}Kr branching under the assumption of a pulsed s–process (Beer, 1986; Beer and Macklin, 1989). But calculations of the main s–process under realistic astrophysical conditions in low mass stars have revealed that the abundances in that branching are not sensitive to the pulsed nature of the neutron exposure (Kappeler et al., 1989b). In addition, the dynamical nature of this mechanism strongly affects the s–isotopes involved in the ^{85}Kr branching. The consequence of the above discussion is that the link between the main and the weak component in a classical scenario turns out to be doubtful.

Besides these difficulties, we saw that both the two models that have been proposed for the weak component in the classical scheme suffer from hard problems: on the one side an exponential distribution of neutron exposures leads to an overproduction of ^{58}Fe and of ^{92,94}Zr, accompanied with an underproduction of ^{70}Ge and ^{76}Se. Table 5.2 gives a picture of the work by Kappeler et al. (1989a) assuming an exponential distribution of neutron exposures for both the main and the weak component. In the upper part of the table the percentages of the main and total (main + weak) contributions (p–corrected) of their s–processes to the solar values are shown; in the lower part the physical conditions they adopted to obtain such results are reported. From table 5.2 it is easy to recognize several difficulties of the Kappeler et al. (1989a)'s classical analysis: in particular,^{70}Ge is underproduced by 31%.

Notice that there is no way of improving the fit to the solar data by simply changing the neutron density and temperature values: the s–only isotopes ^{70}Ge, ^{76}Se, and ^{58}Fe do not depend on branching points, but they are sensitive to the neutron exposure τ alone.

On the other side a single exposure fails to reproduce the ^{58}Fe abundance, which is underproduced by $\sim$ 80 %.

The fact that the contribution of the weak component to the ^{79}Se and ^{85}Kr

CONTRIBUTIONS		
	σN(main)/σN(sun)	σN(all)/σN(sun)
^{58}Fe	0.02	1.14
^{70}Ge	0.13	0.69
^{76}Se	0.26	0.92
^{80}Kr	0.44	1.09
^{82}Kr	0.43	1.12
^{86}Sr	0.62	0.95
^{87}Sr	0.59	0.89
PARAMETERS		
	main	weak
T_8	2.5–3.8	1.8–3.0
$N_n(10^8)$cm^{-3}	1.5–3.5	<0.8–1.9
$\rho(10^3)$ g cm^{-3}	2.6–13	

Table 5.2: The fractional contributions of the weak and weak+main components to the solar–system abundances of the s–only isotopes from iron to strontium (above), and the physical parameters (below) in the Kappeler et al. (1989a)'s paper.

branchings is very model–dependent leads to a very aleatory derivation of the physical parameters characterizing the weak s–process.

In other words, there is no clear statement about what the temperature and neutron density during the weak s–process have to be, and there is not a reliable model for the kind of neutron irradiation occurring there, coming from the classical approach.

More severe difficulties come out when the results of the classical analysis are examined in the light of general astrophysical grounds. The exponential exposure distribution model has to be discarded because, if massive stars are responsible for the synthesis of the s–only isotopes in the range $70 \leq A \leq 90$, there is no evidence for a repeated mechanism such as in low mass stars.

As for the single flux model, the results we found show that it is impossible to reproduce the empirical data with a unique exposure, and in particular with the one that has been proposed by the classical analysis. The best fit solution was found by Beer and Macklin (1989) to have a time integrated flux of $\tau = 0.23$ mb^{-1}, which pratically corresponds to the final exposure occurring in a 25 $M_\odot$ star. As a matter of fact, looking at the results of figure 4.1, apart from the problem of a strong underproduction of ^{58}Fe, a harder problem is encountered for the ^{80}Kr abundance. Indeed, when assuming typical neutron densities of about 10^6 ncm^{-3} and temperatures of T$\simeq 3.5\times10^8$ K as occurring in massive stars, the neutron flow at the ^{79}Se branching essentially goes to ^{80}Kr, with the result of a large overproduction

of ^{80}Kr. [1]

Moreover, the single exposure model for the weak component gives a $\sim$ 30 % contribution to the ^{86}Kr abundance, that we saw to be already produced in excess by the main component. In massive stars, ^{86}Kr is underproduced instead.

As a final comment we would like to point out that the temperature assumed in the single flux scenario is such a low one, that ^{22}Ne could not capture α nuclei and so a problem would arise concerning the neutron source for the s–process.

So we can conclude that neither an exponential distribution of neutron exposures nor a single exposure approximation can fit the empirical data, but a realistic solution can only be found taking in due consideration the astrophysical conditions, and an appropriate average of the various contributions of a generation of stars.

5.3.3 A Generation Of Massive Stars

In order to understand to what extent the s–process coming from a whole spectrum of massive stars is suitable to reproduce the weak component, we emphasize that the efficiency of s–processing during He–burning is in some way related to the stellar mass. Smaller masses are characterized by lower values of the number of neutrons captured by ^{56}Fe nucleus n_c, while higher masses have larger n_c values, until an asymptotic n_c is reached around M$\sim$ 50 M$_\odot$, when all the ^{22}Ne is burnt at helium exhaustion.

In order to calculate the s–process overabundances for increasing n_c, that is for increasing neutron exposures, in typical massive star conditions, we can simply refer to the time behaviour of the overabundances obtained in our 25 M$_\odot$ model. In figure 5.2 we plotted the p–corrected overabundances of the isotopes we are interested in, as a function of n_c.

It is evident that ^{58}Fe is mainly produced for small values of n_c, that is by lower mass stars, while the other s–only isotopes receive a major contribution for higher values. Thus we can be confident that by performing an average of the various contributions coming from a whole stellar generation according to the initial mass function, we shall reach a better understanding for the explanation of the weak component.

Figure 5.3 shows the whole distribution of overabundances obtained for increasing n_c values.

[1] With a neutron density of 1.7×10^8 cm^{-3} and a temperature of 18 KeV, that is 2.1×10^8 K, the branching ratio at ^{79}Se gives: $f = 0.20$, and so only $\sim$ 20 % of the single exposure neutron flow through the ^{79}Se branching goes to ^{79}Br and then to ^{80}Kr, while in our computation almost all the flow follows this way. Since Beer and Macklin (1989) already have a weak contribution to ^{80}Kr of 64 %, a change of the branching ratio in our direction would cause an enormous overproduction of ^{80}Kr!

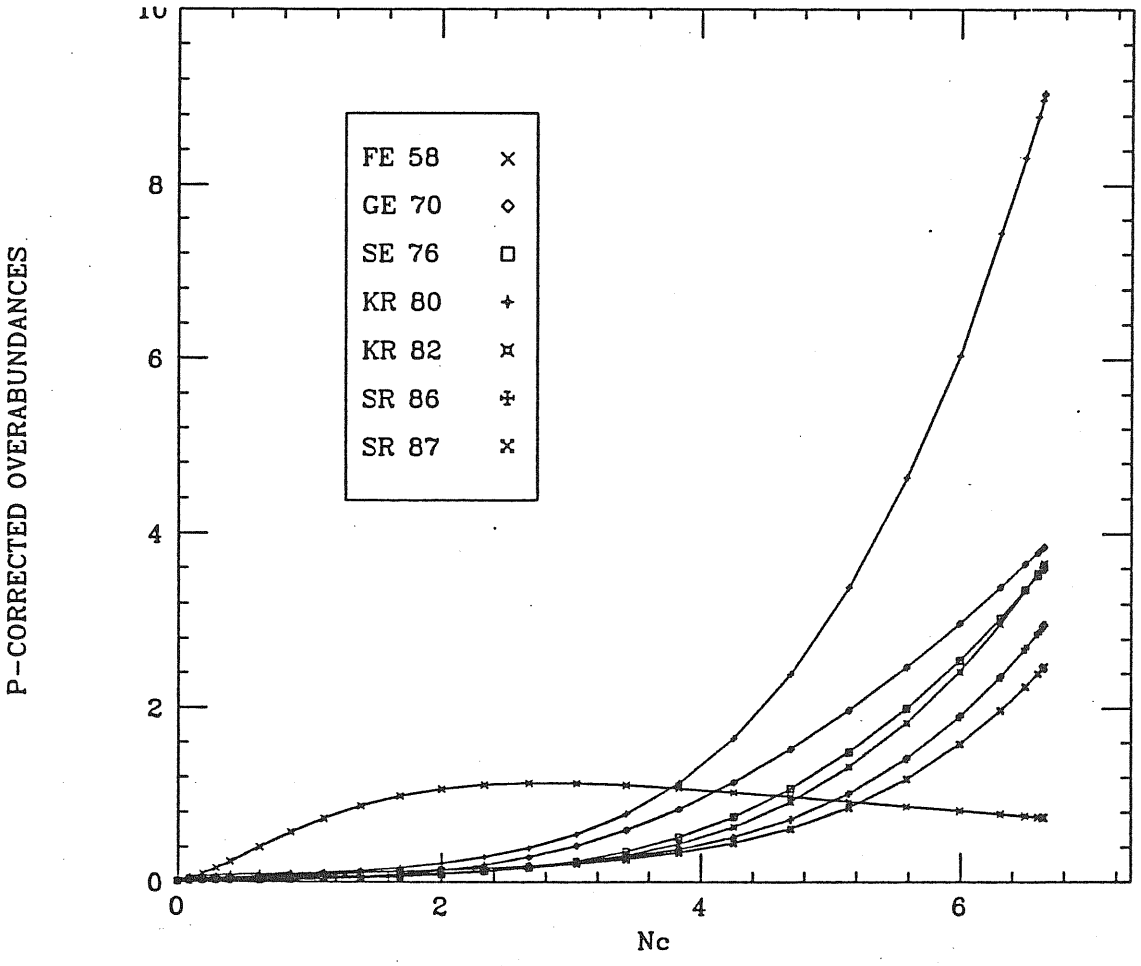

Figure 5.2: Behaviour of some p–corrected isotopic overabundances as a function of n_c. The values are normalized to 100.

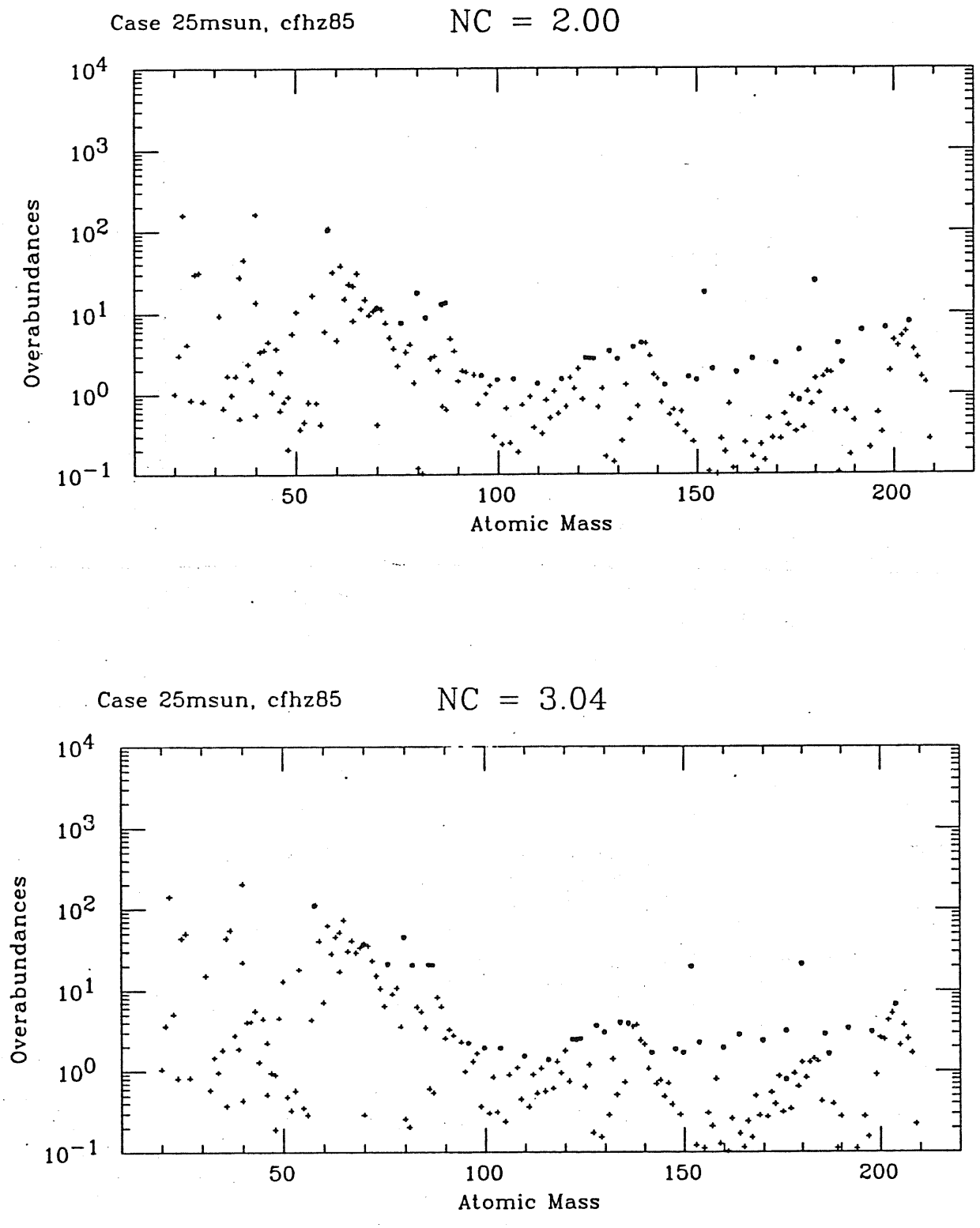

Figure 5.3: Overabundances at He–exhaustion as a function of atomic mass, for various values of n_c.

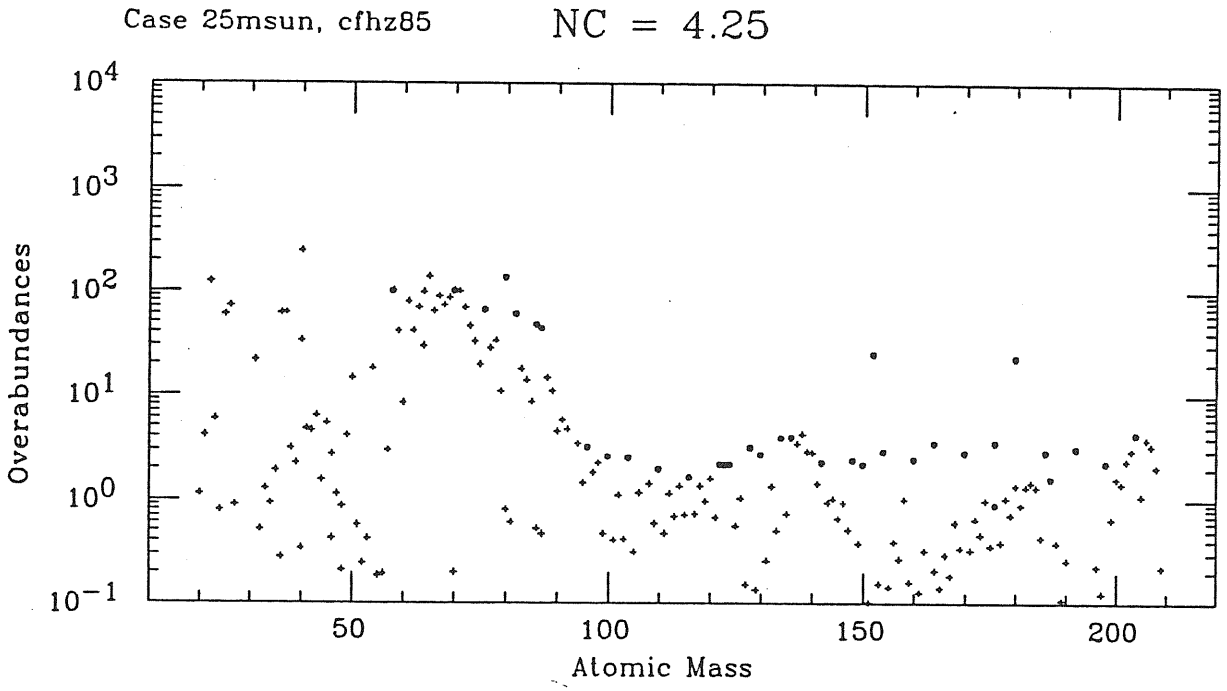
Case 25msun, cfhz85
NC = 4.25
Overabundances
10^4
10^3
10^2
10^1
10^0
10^{-1}
50
100
150
200
Atomic Mass

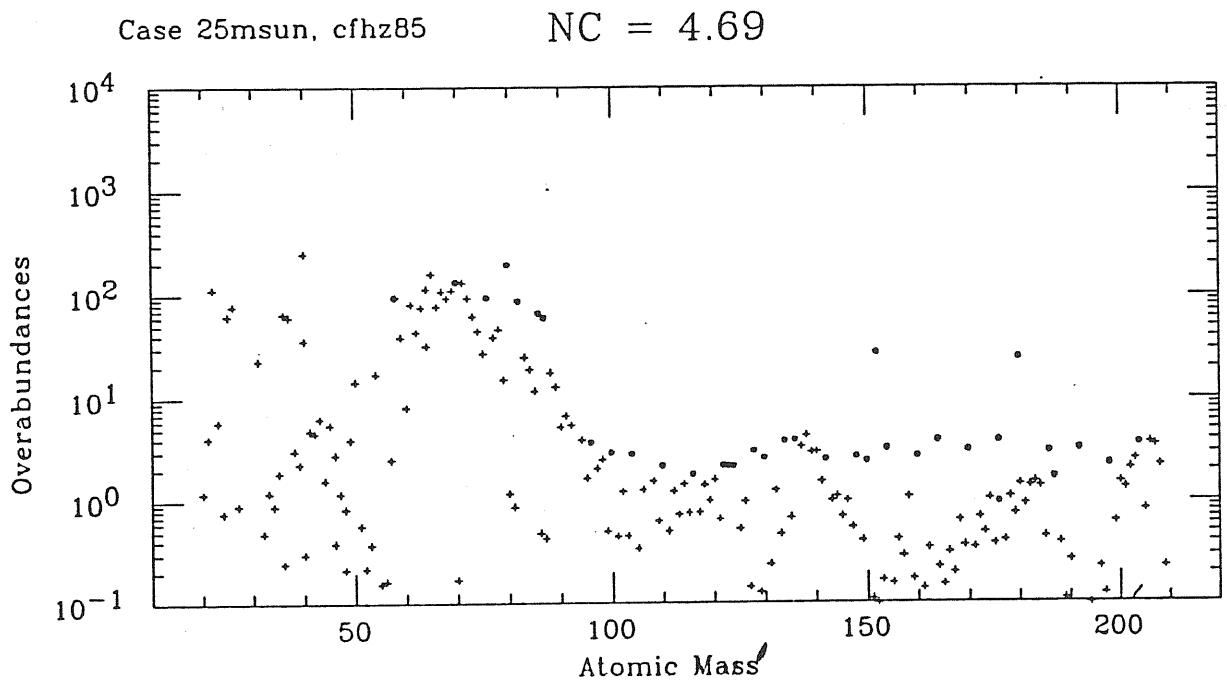
Case 25msun, cfhz85
NC = 4.69
Overabundances
10^4
10^3
10^2
10^1
10^0
10^{-1}
50
100
150
200
Atomic Mass

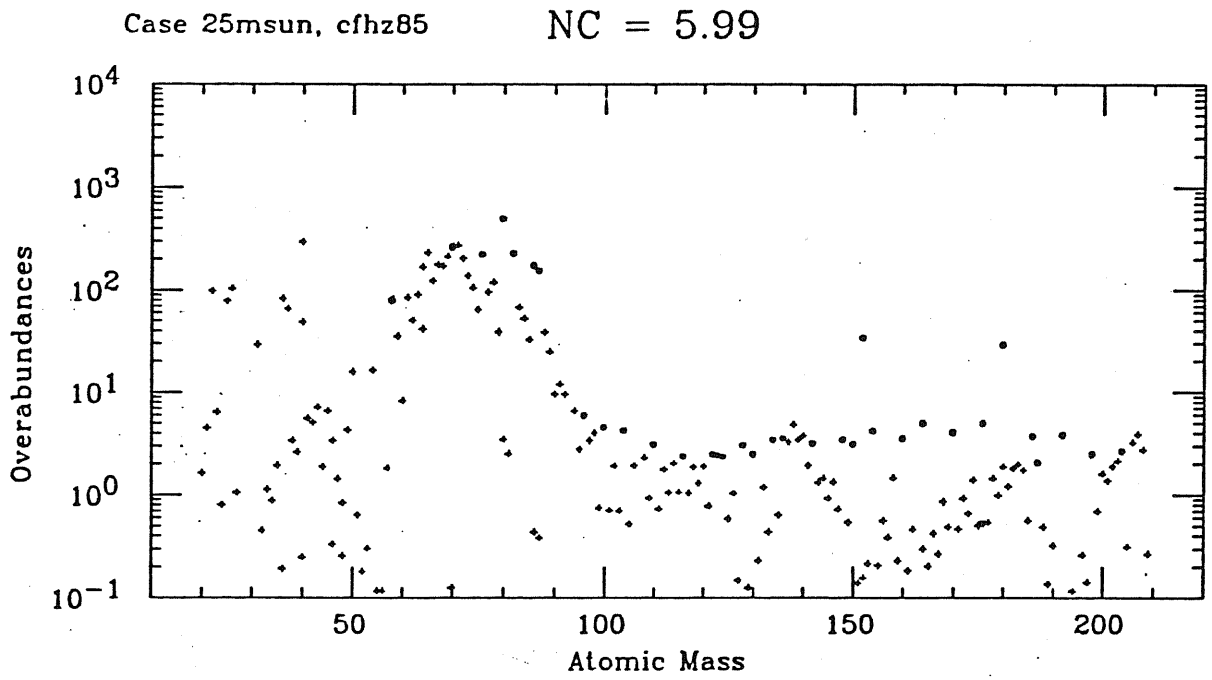
Case 25msun, cfhz85
NC = 5.99
Overabundances
10^4
10^3
10^2
10^1
10^0
10^{-1}
50
100
150
200
Atomic Mass

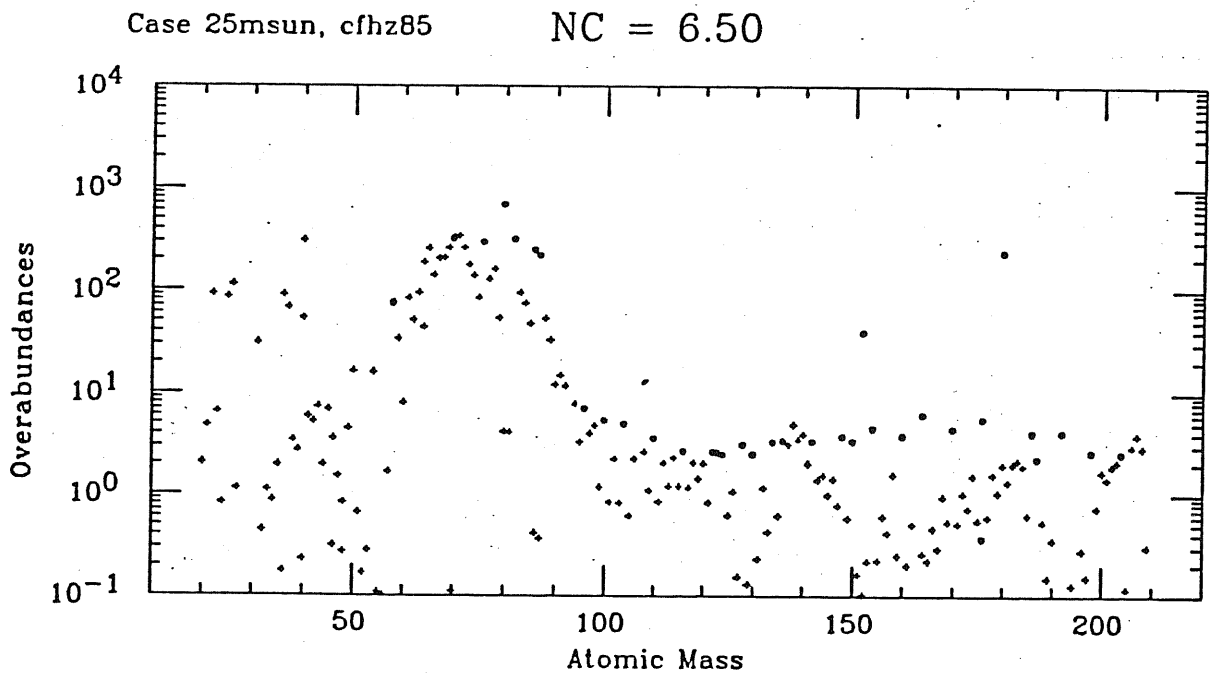
Case 25msun, cfhz85
NC = 6.50
Overabundances
10^4
10^3
10^2
10^1
10^0
10^{-1}
50
100
150
200
Atomic Mass

It is known that the initial mass function $\phi(M)$ represents the Galaxy mass fraction that is included in stars of mass M per stellar mass unity. A power law of the kind $\phi(M) \propto M^{-b}$ is commonly assumed, with b ranging from 1.35 (Salpeter, 1955) to 2 (Lequeux, 1979), the last value holding for $2.5 \leq M/M_{\odot} \leq 100$ stars (see also Miller and Scalo, 1979, and Garmany et al., 1982).

The mass fraction of the chemical species i that is expelled by a stellar generation into the interstellar medium is:

$$\int_{M_{down}} dM\phi(M)q_{co}(M)X_i(M), \tag{5.1}$$

where $q_{co}(M)$ is the ejected mass fraction of the carbon–oxygen rich region from a star of mass M.

M_{down} is the least massive star where the s–process is efficient enough to give a contribution to the chemical s–enrichment.

If we want to follow the temporal evolution of an isotope i, we must integrate over the time:

$$X_i(t) = \int_0^t dt' \frac{dS}{dt'} \int dM\phi(M)q_{co}(M)X_i(M), \tag{5.2}$$

where dS/dt is the stellar birth function, that is the fraction of galactic mass condensed in stars of all masses per time unity. In writing the last equation, the instantaneous recycling hypothesis has been adopted, that is the time delay between the star birth and its death has been neglected, which is allowed when short–lived massive stars are considered. This implies that the right member of equation 5.2 splits into two parts, one containing the integral over time, and the other one over the mass spectrum.

We would like to perform an estimate of the integral 5.1 in order to verify if a stellar generation of massive stars is able to produce ^{58}Fe on one side and the s–only isotopes ^{70}Ge, ^{76}Se, ^{80}Kr, ^{82}Kr, ^{86}Sr and ^{87}Sr on the other side in the same proportions as in the solar system. This calculation will be affected by various uncertainties, because each factor involved is difficult to determine. Before doing this, we still need to correct the calculated abundances from massive stars by the s–contribution from the low mass stars.

5.3.4 Contributions From Low Mass Stars

The calculations of the s–process in thermally pulsing low mass stars by Gallino et al. (1988), Gallino (1988), and Kappeler et al. (1989b) we already mentioned, offer us the possibility of a consistent evaluation of the various s–contributions to the solar abundances.

For the best fit model reproducing the main component, we get the contributions to the isotopes we are interested in that are shown in table 5.3.

Taking into account both the p–corrections and the s–main contributions, we plotted our overabundances versus n_c, scaled by a reference factor of 100 (figure

^{58}Fe	0.02
^{70}Ge	0.12
^{76}Se	0.27
^{80}Kr	0.09
^{82}Kr	0.50
^{86}Sr	0.64
^{87}Sr	0.72

Table 5.3: s–Main contributions from low mass stars.

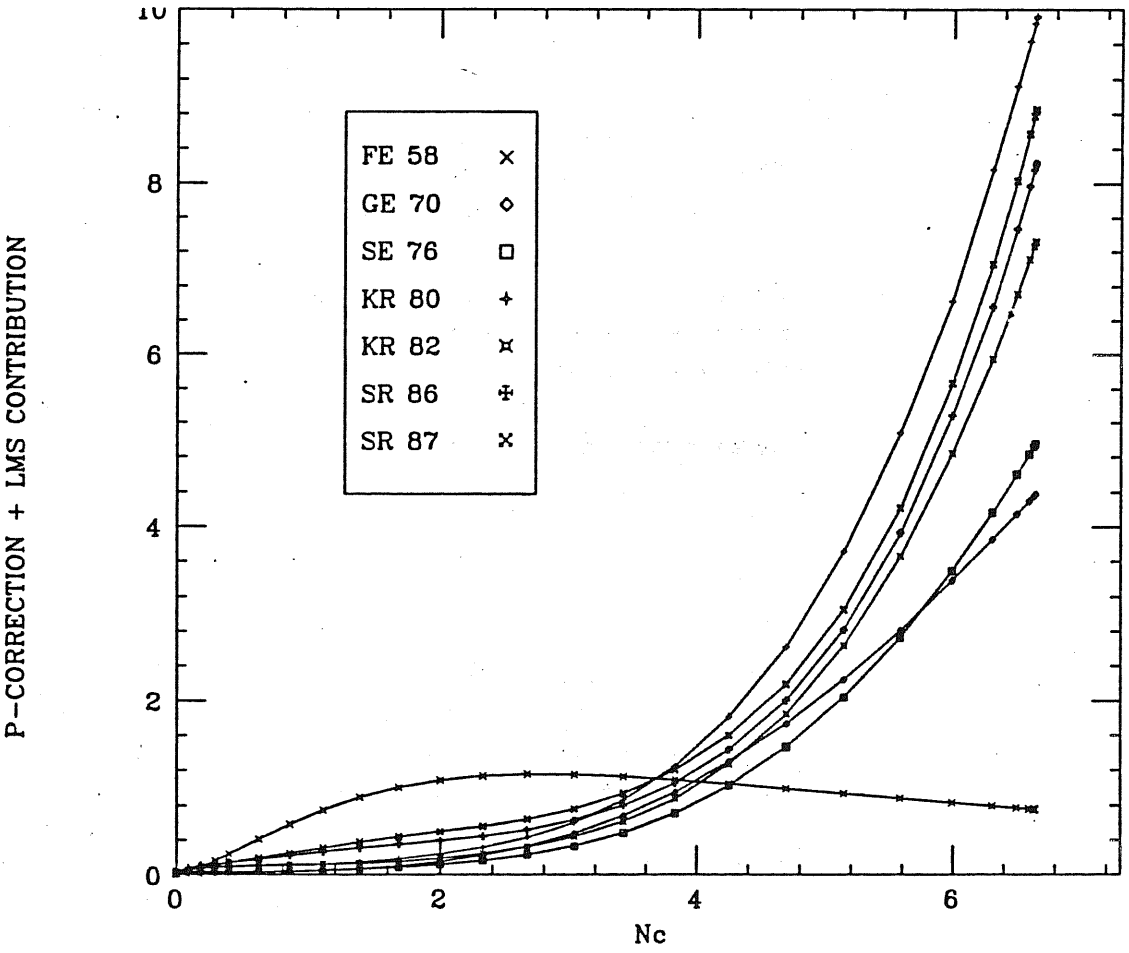

Figure 5.4: p–corrected overabundances as a function of n_c including both the weak and the main s–process contributions. The values are normalized to 100.

	σ(mb)	$\Delta\sigma$(%)	$N_\odot$(atoms/10^6 Si)	$\Delta N_\odot$(%)	$\Delta(\sigma N_\odot)$(%)
^{58}Fe	13	10.0	2.52×10^3	2.7	10.4
^{70}Ge	90	5.5	24.4	9.6	11.1
^{76}Se	163	$\geq$12.0	5.6	6.4	$\geq$13.6
^{80}Kr	251	5.6	0.999	18.0	18.9
^{82}Kr	79	7.3	5.15	18.0	19.4
^{86}Sr	73	5.5	2.32	8.1	9.8
^{87}Sr	98	7.3	1.51	8.1	10.9
^{152}Gd	1010	6.0	6.6×10^{-4}	1.4	6.2
^{180}Ta	1728	11.0	2.48×10^{-6}	1.8	11.1

Table 5.4: Neutron capture cross sections, solar–system number densities and their estimated uncertainties for the s–only isotopes in the $70 \leq A \leq 90$ range. The last column gives the total uncertainty.

5.4). If we compare this figure with figure 5.2, we see that even if there is not a single n_c value that allows us to match the solar distribution, now the spread of the various curves has been greatly reduced for high values of n_c, and in the n_c range 3.6–4.6 the plot shows a fair convergence of the overabundances. Then a single exposure with a n_c value in this range should not be too bad.

A word must be added on the uncertainties affecting our evaluations of the final overabundances. These come from two channels: the neutron capture cross sections and the solar abundances determination. Table 5.4 shows the neutron capture cross sections adopted for our s–only isotopes, together with the uncertainties on their values (Kappeler et al., 1989a), the solar–system number densities with their uncertainties (Anders and Grevesse, 1989), and the resulting $\Delta(\sigma N_\odot)$.

It is evident that the degree of confidence on the σN_s product for ^{76}Se, ^{80}Kr and ^{82}Kr is poor in this region of atomic mass number, so that the analysis of the relative contributions of the various isotopes cannot be pushed too far. We must add that for the discussion of the results the present state of the art should led us not to go underneath a confidence level of two standard deviations. In order to improve the situation a big effort should be made to better evaluate both the maxwellian averaged cross sections of the most important isotopes involved and solar abundances.

DATA					RESULTS	
M	M_{CO}^{ej}	n_c	^{58}Fe	s–only	^{58}Fe	s–only
8–18	0.862	2	120	20	0.649	0.108
18–30	2.448	4	120	120	0.290	0.290
30–50	6.080	7	80	480	0.173	1.037
				SUM:	1.112	1.435

Table 5.5: A rough estimate of equation 5.1

5.4 THE WEAK COMPONENT FROM MASSIVE STARS

Starting from the above considerations we are now able to make a rough estimate of the galactic enrichment by s–only isotopes between iron and zirconium.

As already stressed in the previous chapter, besides the uncertainties coming from nuclear physics and chemical abundance determinations, a major uncertainty comes from the choice of the effective fraction of s–processed material ejected into the interstellar medium by stars of different masses.

As a first guess we can limit ourselves to the scenario presented by Arnett (1972a), which even now constitutes a reliable picture.

In table 5.5 we have tabulated the data used for the computation. We refer to the paper by Couch et al. (1974) who gave the relations between the helium core mass M_α of models evolved by Arnett (1972a) and the range of main sequence mass they can be associated with, and the relation between this M_α and the convective core during He–burning. We have assumed that half of the carbon–oxygen core is ejected by the star during the supernova event, which consists of pure helium burning processed material. Then we have assigned to each range of stellar masses a typical value of n_c characterizing the s–processing. Then, from figure 5.4 we derive the ^{58}Fe overabundance and a mean overproduction factor for the other isotopes. We assume $b = 2$ as the exponent of the initial mass function and calculate the integral 5.1.

The results of our estimate are shown in the same table.

The difference between ^{58}Fe and the average for the s–only isotopes is $\sim$ 29 %. A more detailed analysis dealing with each single s–only isotope shows that a consistent picture can be reached for all of them. This is just a first approximation estimate; better determinations of the amount of He–processed material which is actually ejected by the supernova as a function of the stellar main sequence mass, of the n_c value characterizing this material, of the initial mass function for a stellar generation would be highly desiderable in order to improve the calculation.

Anyway, already at this very basic level it is possible to conclude with some

confidence that the chemical enrichment of the Galaxy by the light s–only isotopes is the result of the contributions of the s–process occurring during helium core burning in massive stars of a whole stellar generation.

Chapter 6

CONCLUSIONS

In this thesis we have followed the evolution of a 25 $M_\odot$ star from the Main Sequence up to the exaustion of helium in the core.

We chose to run a canonical model, that is a model without mass loss and overshooting, because we weren't interested in the evolutionary track, but in the central conditions during the last phases of helium burning.

We checked the influence of different thermonuclear reaction rates and of a change in the initial metal content on the evolution of our star, and in one case we prolongued the evolution up to the end of central carbon burning.

A comparison was made with previous canonical model computations and a general agreement was found, with some differences most probably due to the up to date physical inputs of our evolutionary code.

Then the data produced in this way were used to investigate the s–process nucleosynthesis occurring during the final stages of core helium burning.

A complete nuclear network was set up including the most updated cross sections and weak interaction rates.

We found a very efficient s–process, producing large overabundances of the s–only nuclei in the atomic mass range $70 \leq A \leq 90$, and a good amount of light nuclei too. Our results have been compared with those of the past literature, pointing out the main differences and the possible causes.

Finally, we undertook a deeper analysis of our data trying to insert them into a general view of the chemical enrichment of the interstellar medium. We stressed that only an average of single neutron exposures coming from a whole range of stellar masses according to the initial mass function can explain the solar distribution of the s–process isotopes. This tells the reason why the classical analysis of the weak s–process, which tries to reproduce the empirical data either with an exponential neutron exposure distribution or with a single neutron flux model, without taking in due consideration the astrophysical circumstances under which this process occurs, can't lead to a good fit.

An improved analysis of the s–process in massive stars and of its role in the chemical evolution of the Galaxy would require first of all more evolutionary tracks

to be run for various values of the total star mass. Then, the nucleosynthesis episodes up to the supernova stage should be followed in details, in order to see to what extent the subsequent thermonuclear phases can affect the core He–burning abundances of the s–only isotopes. A refined evolutionary model of the Galaxy, with a better determination of the Initial Mass Function for massive stars would be very appreciated too.

ACKNOWLEDGEMENTS

The evolutionary part of this work was done using the computer facilities of the Trieste Observatory, thanks to the gentle permission of Prof. Giorgio Sedmark. Luigi Pulone taught me how to run the FRANEC code, and assisted me during the hard mounths of numerical computations there. For all the hardware problems I was kindly helped by Paolo Santin.

The nucleosynthesis calculations were done mostly at the Torino University, and I' m very indebted to Prof. Roberto Gallino, who constantly led me during this phase of the work, continuously stimulating me with suggestions and discussions. Special thanks must be adressed to Guido Picchio of the Pino Torinese Observatory, who introduced the nucleosynthesys computation to me and that, together with Maurizio Busso, gave me hints for the prosecution of the work.

Finally, I would like to thank Prof. Dennis Sciama who, as the Director of the Astrophysics Sector of the SISSA, allowed me to start this research, and in a particular way Prof. John Miller, who assisted me whenever I had any type of difficulties, showing a deep interest in what I was doing.

Bibliography

[1] Allen, B. J., Gibson, J. H., and Macklin, R. L. 1971, *Adv. Nucl. Phys.*, 4, 205.

[2] Almeida, J., and Kappeler, F. 1983, *Ap. J.*, **265**, 417.

[3] Anders, E., and Ebihara, M. 1982, *Geochim. Cosmochim. Acta*, **46**, 2263.

[4] Anders, E., and Grevesse,N. 1989, *Geochim. Cosmochim. Acta*, **53**, 197.

[5] Arcoragi, J.-P. 1986, in *Advances in Nuclear Astrophysics*, ed. E. Vangioni-Flam, J. Audouze, M. Casse, J. P. Chieze and J. Tran Thanh Van (Paris: Editions Frontières), p. 385.

[6] Arnett, W.D. 1972a, *Ap. J.* **176**, 681.

[7] Arnett, W.D. 1972b, *Ap. J.* **176**, 699.

[8] Arnett, W.D., and Truran, J.W. 1969, *Ap. J.***157**, 339.

[9] Arnett, W.D., and Thielemann, F.K. 1985, *Ap. J.* **295**, 589.

[10] Bao, Z. Y., and Kappeler, F. 1987, *Atomic Data and Nucl. Data Tables*, **36**, 411.

[11] Bencivenni, D., Castellani, V., and Chieffi, A. 1987, Proc. *Max Planck Institute Conference on Nuclear Astrophysics*, p.204.

[12] Beer, H. 1986, in *Advances in Nuclear Astrophysics*, ed. E. Vangioni-Flam, J. Audouze, M. Casse, J. P. Chieze and J. Tran Thanh Van (Paris: Editions Frontières), p. 375.

[13] Beer, H., Walter, G., and Macklin, R. L. 1985, in *Capture Gamma- Rays Spectroscopy and Related Topics*, ed. S. Raman (New York: American Institute of Physics), p. 778.

[14] Beer, H., and Macklin, R. L. 1988, *Ap. J.*, **331**, 1047.

[15] Beer, H., and Macklin, R. L. 1989, *Ap. J.* **339**, 962.

[16] Bertelli, G., Bressan, A. G., and Chiosi, C. 1984, *Astron. Astrophys.* **130**, 279.

[17] Bertelli, G., Bressan, A. G., and Chiosi, C. 1985, *Astron. Astrophys.* **150**, 33.

[18] Bertelli, G., Bressan, A. G., Chiosi, C., and Angerer, K. 1986, *Astron. Astrophys. Suppl.* **66**, 191.

[19] Bressan, A. G., Bertelli, G., and Chiosi, C. 1981, *Astron. Astrophys.*, **102**, 25.

[20] Brunish, W.M., and Truran, J.W. 1982a, *Ap. J.* **256**, 247.

[21] Brunish, W.M., and Truran, J.W. 1982b, *Ap. J. Suppl.* **49**, 447.

[22] Burbidge, G. R., Burbidge, E. M., Fowler, W. A., and Hoyle, F. 1957, *Rev. Mod. Phys.*, **29**, 547.

[23] Busso, M., and Gallino, R. 1985, *Astron. Astrophys.*, **151**, 205.

[24] Busso, M., Gallino, R., Picchio, G., and Chieffi, A. 1987, *Mem. S.A.It.*, **57**, 539.

[25] Busso, M., Picchio, G., Gallino, R., and Chieffi, A. 1988, *Ap. J.*, **326**, 196.

[26] Cameron, A. G. W. 1955, *Ap. J.*, **121**, 144.

[27] Cameron, A. G. W. 1973, *Space Sci. Rev.*, **15**, 121.

[28] Cameron, A. G. W. 1982, *Ap. Space Sci.*, **82**, 123.

[29] Castellani, V., Giannone, P., and Renzini, A. 1971a, *Ap. Space Sci.*, **10**, 340.

[30] Castellani, V., Giannone, P., and Renzini, A. 1971b, *Ap. Space Sci.*, **10**, 355.

[31] Castellani, V., Chieffi, A., Pulone, L., and Tornambe', A. 1985, *Ap. J.*, **296**, 204.

[32] Caughlan, G. R., Fowler, W. A., Harris, M. J., and Zimmerman, B. A. 1985 (CFHZ85), *Atomic Data and Nucl. Data Tables*, **32**, 197.

[33] Caughlan, G. R., and Fowler, W. A. 1988 (CF88), *Atomic Data and Nucl. Data Tables*, **40**, 283.

[34] Chiosi, C., and Maeder, A. 1986, *Ann. Rev. Astron. Astrophys.* **24**, 329.

[35] Chiosi, C., Bressan, A., and Bertelli, G. 1986, in *Advances in Nuclear Astrophysics*, ed. E. Vangioni-Flam, J. Audouze, M. Casse, J. P. Chieze and J. Tran Thanh Van (Paris: Editions Frontières), p. 145.

[36] Clayton, D. D., Fowler, W. A., Hull, T. E., and Zimmerman, B. A. 1961, *Ann. Phys.*, **12**, 331.

[37] Cosner, K., Iben, I., Jr., and Truran, J. W. 1980, *Ap. J. (Letters)*, **238**, L91.

[38] Cosner, K., and Truran, J. W. 1981, *Ap. Space Sci.*, **78**, 85.

[39] Couch, R. G., Schmiedekamp, A. B., and Arnett, W. D. 1974, *Ap. J.*, **190**, 95.

[40] Fowler, W. A., Caughlan, G. R., and Zimmerman, B. A. 1971, private communication..

[41] Fowler, W. A., Caughlan, G. R., and Zimmerman, B. A. 1975 (FCZ75), *Ann. Rev. Astron. Astrophys.*, **13**, 69.

[42] Fuller, G. M., Fowler, W. A., and Newman, M. J. 1982, *Ap. J. Suppl.*, **48**, 279.

[43] Gallino, R. 1988, in *Evolution of Peculiar Red Giant Stars*, Proc. IAU Coll. no. 106, ed. H. R. Johnson (Cambridge: Cambridge Univ. Press), in press.

[44] Gallino, R., and Busso, M. 1985, in *From Nuclei to Stars*, ed. A. Molinari and R. A. Ricci (Amsterdam: North-Holland), p. 309.

[45] Gallino, R., Busso, M., Picchio, G., Raiteri, C. M., and Renzini, A. 1988, *Ap. J. (Letters)*, **334**, L45.

[46] Gallino, R., Busso, M., Picchio, G., and Raiteri, C. M. 1989, On the Origin of the Strong Component of the s–process, Proc. *Elba Workshop on Chemical and Dynamical Evolution of Galaxies.*

[47] Garmany, C. D., Conti, P. S., and Chiosi, C. 1982, *Ap. J.*, **263**, 777.

[48] Harris, M. J., Fowler, W. A., Caughlan, G. R., and Zimmerman, B. A. 1983, *Ann. Rev. Astron. Astrophys.*, **21**, 165.

[49] Hollowell, D. E., and Iben, I., Jr. 1988, *Ap. J. (Letters)*, **333**, L25.

[50] Hollowell, D. E., and Iben, I., Jr. 1989, *Ap. J.*, **340**, 966.

[51] Holmes, J. A., Woosley, S. E., Fowler, W. A., and Zimmerman, B. A. 1976, *Atomic Data and Nucl. Data Tables*, **18**, 305.

[52] Howard, W. M., Mathews, G. J., Takahashi, K., and Ward, R. A. 1986, *Ap. J.*, **309**, 633.

[53] Iben, I., Jr. 1972, *Ap. J.*, **178**, 433.

[54] Iben, I., Jr. 1975, *Ap. J.*, **196**, 549.

[55] Iben, I., Jr., and Renzini, A. 1982a, *Ap. J. (Letters)*, **259**, L79.

[56] Iben, I., Jr., and Renzini, A. 1982b, *Ap. J. (Letters)*, **263**, L23.

[57] Kappeler, F. 1986, in *Advances in Nuclear Astrophysics*, ed. E. Vangioni-Flam, J. Audouze, M. Casse, J. P. Chieze and J. Tran Thanh Van (Paris: Editions Frontières), p. 355.

[58] Kappeler, F. 1989, internal report.

[59] Kappeler, F., Beer, H., Wisshak, K., Clayton, D. D., Macklin, R. L., and Ward, R. A. 1982, *Ap. J.*, **257**, 821.

[60] Kappeler, F., Beer, H., Wisshak, K., 1989a, *Reports on Progress in Physics*, in press.

[61] Kappeler, F., Busso, M., Gallino, R., and Raiteri, C.M. 1989b, *Ap. J.*, submitted.

[62] Kippenhan, R., Weigert, A., and Hofmeister, E. 1967, in *Methods in Computational Physics* vol.7, Astrophysics Academic press, p.129.

[63] Klay, N., and Kappeler, F. 1988, *Phys. Rev. C***38**, 295.

[64] Lamb, S., Iben, I.Jr., and Howard, W.M. 1976, *Ap. J.* **207**, 209.

[65] Lamb, S., Howard,W.M., Truran, J.W., and Iben, I.Jr. 1977, *Ap. J.* **217**, 213.

[66] Lamers, H. J. G. L. M. 1981, *Ap. J.*, **245**, 593.

[67] Langer, N. 1986a, Phd. Thesis, unpublished.

[68] Langer, N. 1986b, *Astron. Astrophys.*, **164**, 45.

[69] Langer, N., El Eid, M. F., and Fricke, K.J. 1985, *Astron. Astrophys.*, **145**, 179.

[70] Langer, N., Arcoragi, J.-P., and Arnould, M. 1989, *Astron. Astrophys.* **210**, 187.

[71] Lequeux, J. 1979, *Astron. Astrophys.*, **80**, 35.

[72] Maeder, A. 1975, *Astron. Astrophys.*, **40**, 303.

[73] Maeder, A. 1981a, *Astron. Astrophys.* **101**, 385.

[74] Maeder, A. 1981b, *Astron. Astrophys.* **102**, 401.

[75] Maeder, A., and Meynet, G. 1987, *Astron. Astrophys.* **182**, 243.

[76] Maeder, A., and Meynet, G. 1989, *Astron. Astrophys.* **210**, 155.

[77] Miller, G. E., and Scalo, J. M. 1979, *Ap. J. Suppl.*, **41**, 513.

[78] Prantzos, N., Doom, C., Arnould, M., and de Loore, C. 1986, *Ap. J.* **304**, 695.

[79] Prantzos, N., Arnould, M., and Arcoragi, J.P. 1987, *Ap. J.* **315**, 209.

[80] Ratynski, W., and Kappeler, F. 1988a, *Phys. Rev. C*,**37**, 595.

[81] Ratynski, W., and Kappeler, F. 1988b, internal report.

[82] Reeves, H. 1966, *Ap. J.*, **146**, 447.

[83] Reimers, D. 1975, *Mem. Soc. Roy. Liege 6th. Ser*, **8**, 369.

[84] Ross, J. E., and Aller, L. H. 1976, *Science*, **191**, 1223.

[85] Salpeter, E. E. 1955, *Ap. J.*, **121**, 161.

[86] Schwarzschild. M. 1958, in *Structure and Evolution of Stars*, (New York: Dover Publ. Inc.), p.167.

[87] Seeger, P. A., Fowler, W. A., and Clayton, D. D. 1965, *Ap. J. Suppl.*, **11**, 121.

[88] Straniero, O. 1989, *Astron. Astrophys. Suppl.* **76**, 157.

[89] Takahashi, K., and Yokoi, K. 1983, *Nucl. Phys.*A**404**, 578.

[90] Takahashi, K., and Yokoi, K. 1987, *Atomic Data and Nucl. Data Tables*, **36**, 375.

[91] Truran, J. W., and Iben, I., Jr. 1977, *Ap. J.*, **216**, 797.

[92] Ulrich, R. K. 1973, in *Explosive Nucleosynthesis*, ed. D. N. Schramm and W. D. Arnett (Univ. of Texas: Austin), p. 139.

[93] Ward, R. A., Newman, M. J., and Clayton, D. D. 1976, *Ap. J. Suppl.*, **31**, 33.

[94] Ward, R. A., and Newman, M. J. 1978, *Ap. J.*, **219**, 195.

[95] Weaver, T.A., Zimmerman, G.B., and Woosley, S.E. 1978, *Ap. J.* **225**, 1021.

[96] Weiss, A. 1989, *Ap. J.* **339**, 365.

[97] Winters, R. R., Kappeler, F., Wisshak, K., Mengoni, A., and Reffo, G. 1986, *Ap. J.*, **300**, 41.

[98] Winters, R. R., and Macklin, R. L. 1988, *Ap. J.*, **329**, 943.

[99] Woosley, S. E. 1986, in *Nucleosynthesis and Chemical Evolution*, SAAS–FEE Summer Course, Audouze, J., Chiosi, C., and Woosley, S.E. (eds.), p.1.

[100] Woosley, S. E., Fowler, W. A., Holmes, J. A., and Zimmerman, B. A. 1978, *Atomic Data and Nucl. Data Tables*, **22**, 371.

[101] Woosley, S.E., and Weaver, T.A. 1986, in *"Nucleosynthesis and Its Implications on Nuclear and Particle Physics"*, Audouze, J. and Mathieu, N. (eds.), p.145.

List of Tables

List of Figures